PHOTODISSOCIATION PROCESSES IN MOLECULAR BEAMS
Lee Richard Carlson

by

Lee Richard Carlson

Materials and Molecular Research Division
Lawrence Berkeley Laboratory

and

Department of Chemistry
University of California
Berkeley, California 94720

Table of Contents

ACKNOWLEDGMENTS

I sincerely wish to acknowledge the help and cooperation that I have received during these graduate studies. I am particularly grateful for the guidance and support from Professor Y. T. Lee which has been most valuable in bringing this research to a successful conclusion.

Special thanks is given to Professor Y. R. Shen, R. K. Sparks, Dr. K. Shobatake, M. L. Kowalczyk, C. Hayden, S. Bustamente, and Dr. D. Gerlich who participated in many aspects of these studies.

The help and cooperation that I received from all the members of the Lawrence Berkeley Laboratory molecular beam group is also appreciated: Dr. C. Ng, Dr. M. Coggiola, A. Wang, J. Valentini, Dr. P. Tiedemann, Dr. P. Casavecchia, R. Buss, M. Vernon, S. Ceyer, C. Kahler, S. Sibener, P. Schulz, A. Sudbo, Dr. E. Grant, Dr. M. Faubel, D. Trevor, S. Anderson, D. Krajnovich, D. Neumark, Dr. H. Kwok, Dr. T. Hirooka, and R. Baseman.

The administrative and technical support of A. Weightman, A. Susoff, and C. Taylor was invaluable.

Finally, I wish to thank my wife, Clare, and sons, Stephen and Michael, who have been extremely understanding and cooperative.

This work has been financially supported by the Division of Chemical Sciences, Office of Basic Energy Sciences, U. S. Department of Energy Under Contract No. W-7405 - Eng. - 48.

PHOTODISSOCIATION PROCESSES IN MOLECULAR BEAMS

Lee Richard Carlson

Materials and Molecular Research Division
Lawrence Berkeley Laboratory

and

Department of Chemistry
University of California
Berkeley, California 94720

May 1979

ABSTRACT

A description is presented of a study of the photodissociation dynamics of molecules in a molecular beam. Photofragmentation translational spectroscopy has been utilized to observe the photodissociation dynamics of ozone. Using a supersonic molecular beam and a 10 nanosecond pulsed laser at λ = 266 nm, the velocities of the fragment products are measured by the method of time of flight.

The resolution of the time of flight spectrum of ozone is sufficiently high that the electronic and vibrational states are clearly resolved and identified. Above the threshold (λ < 310 nm), the quantum yield for the production of $O(^1D)$ has been estimated in the past to be unity for the process

$$O_3\ (^1A_1) + h\nu)\lambda < 300\ nm) \rightarrow O_3(^1B_2) \rightarrow O_2(^1\Delta_g) + O(^1D)$$

However a small production of $O_2\ (^3\Sigma_g^-) + O(^3P)$ has been observed in this study.

The $O_2(^1\Delta_g)$ product yields four vibrational states (v = 0, 1, 2, 3) which yields a vibrational temperature of 2700°K along with narrow energy distributions of rotational levels. These energy distributions are compared with photodissociation models along with the polarization dependence of the dissociative process which was also measured.

I. INTRODUCTION

The study of the dynamics of photodissociative processes has been an active field of research for many years. Yet, there is still little detailed information about the dissociation states of polyatomic molecules, and the dynamics of the dissociation process.[1] Simple systems such as linear triatomic molecules are still ambiguous as to their actual dissociative mechanism. In order to further understand the nature of photodissociation dynamics, it is desirable to study small systems, i.e. quasidiatomic and triatomic, where it is possible to compare the results of experiments with advancing theory. For this reason we have chosen to study the photodissociation dynamics of the nonlinear triatomic ozone molecule.

Photofragment translational spectroscopy, which is conceptually very simple, has in principle all the attributes necessary to study the dynamics of photodissociative events. The probability for a molecule to absorb light is dependent on the orientation of the molecule with respect to the E vector of the excitation source. If the photofragments that are formed recoil in a nonrandom fashion, the spatial anisotropy of the products gives information about the dissociative transition. Information about the energy partitioning of the excess energy among the electronic, vibrational, rotational, and translational degrees of freedom of

fragments yields details of electronic curve crossings, vibrational couplings, rotational interactions, and all other factors associated with the time dependence in the fragmentation event. Thus by measuring the anisotropy in angular distribution and energy partition of the fragments from photolyzed molecules, photodissociative mechanisms can be determined.

Design Criteria for Photofragment Spectrometer

Figure 1 shows the basic features of a photofragment spectrometer. A molecular beam is crossed with short pulses of linearly polarized light and generally a quadrupole mass spectrometer is used to selectively detect relative fluxes of the fragments.[2] By varying the polarization angle of the light pulse, one can measure the angular distribution of fragment products. Also by measuring the flight time from the photolyzing pulse, the velocity of the products can be obtained. Invoking energy conservation,

$$E_{Trans} = E_{Photon} - E_{Bond} - E_{Internal} \quad (1)$$

one obtains an energy distribution for the products.

Several instruments of this type have been used in the study of photofragmentation in the past; however, each has encountered some difficulties in obtaining high resolution spectra for a large variety of molecules due to various reasons.[2,3,4] If one uses an effusive molecular beam, the

translational energy of the beam is thermally distributed. If the fragment translational energy is not in excess with respect to this Boltzmann energy distribution of the beam, the product state distributions will be severely broadened in the time of flight spectrum.[5,6] Utilization of equation 1 assumes that all absorptions originate in a single rovibronic state of the parent molecule. This, however, is not the case for a thermal beam. By using a "seeded" supersonic nozzle, the velocity distribution can be reduced to less than 10 percent of the most probable velocity, and rotational temperatures of less than 10°K can be easily obtained.

Figure 2 shows the velocity distribution of a thermal source, and a supersonic expansion of an ideal gas. The reduced velocity spread and the enhancement of the velocity of the supersonic beam due to the conversion of thermal energies to translational energy are immediately apparent. Another advantage in using a supersonic expansion source is the increase in number density at a greater distance from the source which is theoretically given by:[7]

$$I(r,x) = n,\pi r_s^2 \left(\frac{m}{2\pi kT}\right)^{3/2} x \int_0^{\infty} \exp -\left[\frac{m}{2kT} \left\{(C-u_1 \cos\theta_2)^2 + u^2 \sin^2\theta_2\right\}\right] \times C^3 dC \cos^4\theta_1 \frac{1}{x^2} \qquad (2)$$

where an effusive source yields a cos(θ) angulard distribution. Comparing the intensity of a supersonic beam to that of an effusive beam, one finds that[8]

$$\frac{I_{nozzle}}{I_{effusive}} = \left(\frac{\gamma}{3}\right)^{3/2} M^2 \exp(1.5) \qquad (3)$$

where γ is the ratio of the specific heats and M is the mach number, defined by

$$M^2 = (V_{most\ probable})^2/C^2 \qquad (4)$$

where C is the speed of sound in the expansion. Thus employing supersonic nozzle sources in a photofragment spectrometer can greatly enhance the signal and the resolution of the time of flight spectrum.

If the translational energy of the product states is high and the length of the ionizer is short compared with the flight path, the resolution of the spectrum can be limited to the minimum channel width of the multichannel analyser. Typical multichannel scalers permit sampling times per channel as small as 1 microsecond. If, however, the fragment product reaches the detector in 10 microseconds, then one can only expect 10 percent resolution. This problem can be minimized by employing a "seeded" supersonic nozzle. By observing the fragments which are scattered backward from the direction of the beam, the laboratory velocity of the fragment is reduced. By expanding

a light gas such as H_2 or He which contains a few percent of the molecule of interest, one finds that the molecule to be studied is forced to attain the velocity of the light gas in the isentropic limit. Thus beam energies of several eV can, in certain cases, be achieved in this fashion. Figure 3 shows the difference in laboratory fragment velocity for one arbitrary center of mass fragment energy seeded in H_2 and in Xe. By choosing an appropriate seed gas, it is possible to obtain suitable flight times for a given experiment.

If the translational energy of a fragment is small compared to the beam velocity, it is possible that the fragment will never reach the detector in an off axis geometry. As seen in Figure 4, utilization of a detector at 30° from the beam accepts translational energies of products not seen at 90°. It is therefore desirable to use a rotating detector which can be placed at small laboratory angles for low energy fragmentation and moved to backward scattered angles for high energy fragmentation.

As mentioned, the angular distribution of the fragments gives information about the excitation process and the lifetime of the dissociative state.[9] The probability for photon absorption from an initial state i to final state f is proportional to $|E \cdot \mu_{fi}|^2$ where $\mu_{fi} = \langle f | \mu | i \rangle$ and μ is the electric dipole operator. Using a classical picture, the

transition amplitude is proportional to the projection of the electric field on the direction of the transition moment of the molecule and the transition probability is proportional to the square of the absolute value of the amplitude. One finds then that the photon absorption probability is proportional to $\cos^2(\alpha)$ where α is the angle between E and μ_{fi}.

It can be shown from spherical trigonometry[10,11,12,13], that the center of mass angular distribution for fragment recoil with respect to E can be generalized for the C.M. angular distribution for an arbitrary recoil distribution $P(\beta)$ by

$$W(\theta) = \int_0^{\pi} (4\pi)^{-1} \left[1 + 2P_2(\beta)P_2(\theta)\right] P(\beta)\, d\beta \qquad (5)$$

$$= (4\pi)^{-1} \left[1 + 2bP_2(\theta)\right] \qquad (6)$$

where $b = \int_0^{\pi} P_2(\beta)P(\beta)d\beta$

Here θ is the angle between E and the center of mass angle, and β is the angle between μ_{fi} and the axis of fragmenting recoil as shown in Figure 5. $P_2(\beta)$ and $P_2(\theta)$ are the second degree Legendre polynomials in cosine. Thus

$$P_2(\theta) = \frac{(3\cos^2(\theta) - 1)}{2}$$

We see that the angular dependence of the photofragment process regardless of the dynamics is given by equation 6.

The information of the dynamics is contained in b.

Figure 6 shows three dissociating models.[9] If $b = P_2(\beta)$, then the process is impulsive, and the axis of recoil fragmentation will lie in a cone with half angle β. If rotation of the molecule during the dissociation is significant then $b = P_2(\alpha)P_2(\beta)$ as shown in 6b. If the excited state of the parent molecule has a finite lifetime before fragmentation, then b can be expressed by

$$b = \left[\frac{P_2(\alpha) + \psi^{-2} - 3\psi \sin\alpha \cos\alpha}{1 + 4\psi^{-2}}\right] P_2(\beta) \qquad (7)$$

where ψ is the angle through which the molecule will rotate ($\psi = \omega\tau$). Employing these models, values of b can be obtained which best fit the angular distribution data. Such angular distributions can best be obtained where E is rotated using a half wave retardation plate. To obtain all angles (θ) the geometry of the apparatus should be such that the E vector can generate all angles, from 0 to 90° with respect to the detector.

The energy and angular distributions thus far described assume a collision free environment. To estimate the vacuum necessary to achieve this criteria, it is simple to calculate the number of collisions from the interaction region to the detector.

Much more serious vacuum criteria are encountered, however, when considering the method of signal detection, and the nature of the evolution of background. The most frequently utilized mass selective fragment detector is the quadrupole mass spectrometer. For general purpose fragment detection, electron impact ionization followed by ion detection is presently the most desirable choice. One finds, however, using this technique that only one fragment in a thousand that enter the ionizer is detected. Further complications arise from background gas having the same mass as the fragment. In a 5 per cent seeded nozzle, one might expect 10^{10} molecules/cc of the dissociating species. If the irradiation source interacts with a 0.1 cm^3 volume of the molecular beam, it would then be possible to dissociate 10^9 molecules assuming saturation for the photoabsorption. In order to achieve the desired resolution in the time of flight spectrum, the in plane collection angle should be small, typically less than 2 degrees. If the fragments are scattered in 4π steradians, a collection efficiency of 6×10^{-5} is obtained, and the final fragment number density at the ionizer (1 Cm^3 volume) is 6×10^4 fragments per cm^3, which corresponds to a partial pressure of 2×10^{-12} torr. Thus the background gas which generates particles with the same mass as the photofragments must have a partial pressure comparable to that of the photofragments during the detection interval.

Using the criteria stated above, a general purpose crossed molecular beam facility used as a photofragment spectrometer was constructed and is shown in Figure 7.[14,15] Details of the apparatus can be found elsewhere, and features relevant to the experiments are described in the experimental section.

FOOTNOTES

1. William M. Gelbart, Ann. Rev. Phys. Chem. 28, 223 (1977).

2. George E. Busch, John F. Cornelius, Richard T. Mahoney, Robert I. Morse, Donald W. Schlosser, and Kent R. Wilson, Rev. Sci, Inst. 41, 1066 (1970).

3. J. Solomon, C. Jonah, P. Chandra, and R. Bersohn, J. Chem. Phys., 55, 1908 (1971).

4. C. E. Fairchild, E. J. Stone, and G. M. Lawrence, J. Chem. Phys., 69, 3632 (1978).

5. C. Jonah, J. Chem. Phys., 55, 1915 (1971).

6. George E. Busch and Kent R. Wilson, J. Chem. Phys., 56, 3626 (1972).

7. J. B. Anderson and J. B. Fenn, Phys. Fluids, 8, 780 (1965).

8. J. J. Valentini, Ph.D. Thesis (University of California, Berkeley, Berkeley, California, 1976).

9. George E. Busch and Kent R. Wilson, J. Chem. Phys. 56, 3638 (1972).

10. R. N. Zare, Ph.D. Thesis (Harvard University, Cambridge, Mass., 1964).

11. J. Solomon, J. Chem. Phys. 47, 889 (1967).

12. Sze-cheng Yang and Richard Bersohn, J. Chem. Phys. 61, 4400 (1974).

13. R. Bersohn and S. H. Lin, Adv. Chem. Phys. 16, 67 (1969).

14. R. K. Sparks, to be published.

15. Y. T. Lee, J. D. McDonald, P. R. Lebreton, and D. R. Herschbach, Rev. Sci. Instr., 40, 1402 (1969).

FIGURE CAPTIONS

Fig. 1 Schematic diagram of a molecular beam photofragment spectrometer. The E field is varied to obtain the fragment spatial distribution for horizontal in plane scattering.

Fig. 2 Velocity distribution of a thermal effusive beam, and the velocity distribution of a supersonic nozzle beam using a source temperature of 298°K, mass of 40 a.m.u. and a mach = 20 nozzle. The distributions have been scaled to total intensity (area). The effect of equation 3 is omitted.

Fig. 3 Newton diagram for a single energy fragment using a light molecular weight gas (helium) and a heavy gas (xenon).

Fig. 4 Schematic of fragmentation dynamics for various laboratory detector angles. The advantage of using a rotating detector is thus illustrated in that all fragments can be detected.

Fig. 5 Diagram of angles defined in equations 5 through 7.

Fig. 6 Pseudo diatomic molecules, and the dissociation processes used to derive equations 5 through 7. These diagrams are obtained from Ref. 9.

Fig. 7 Crossed molecular beam facility adapted for use as a photofragment spectrometer.

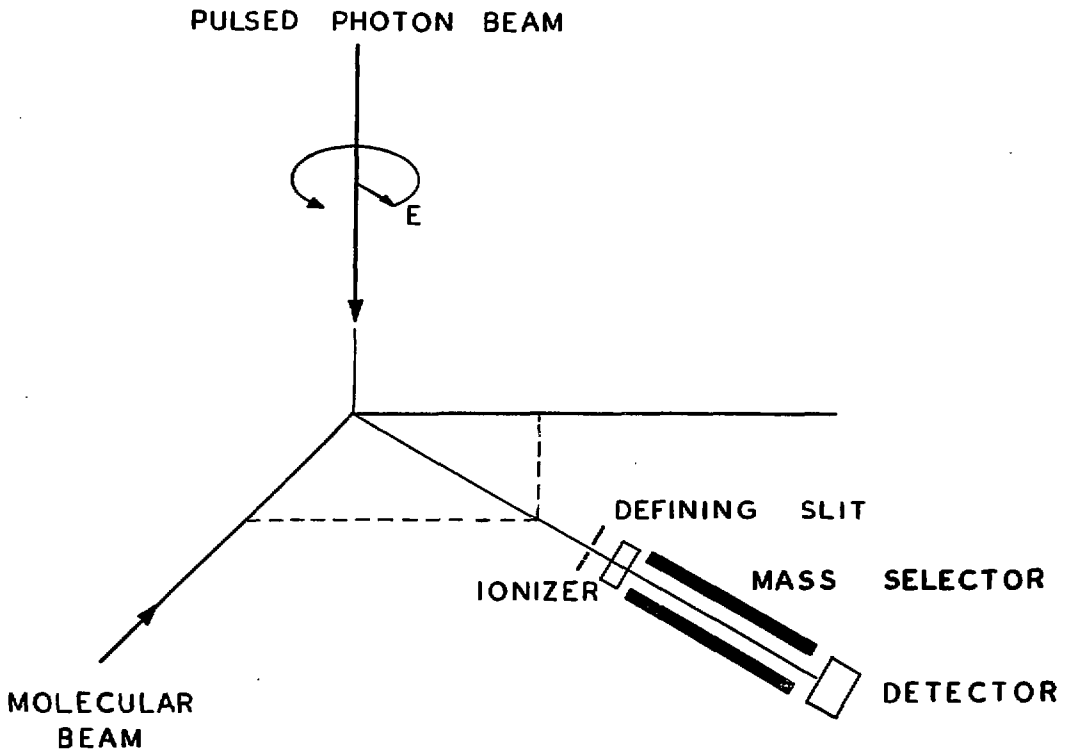

FIGURE 1

XBL 795-9743

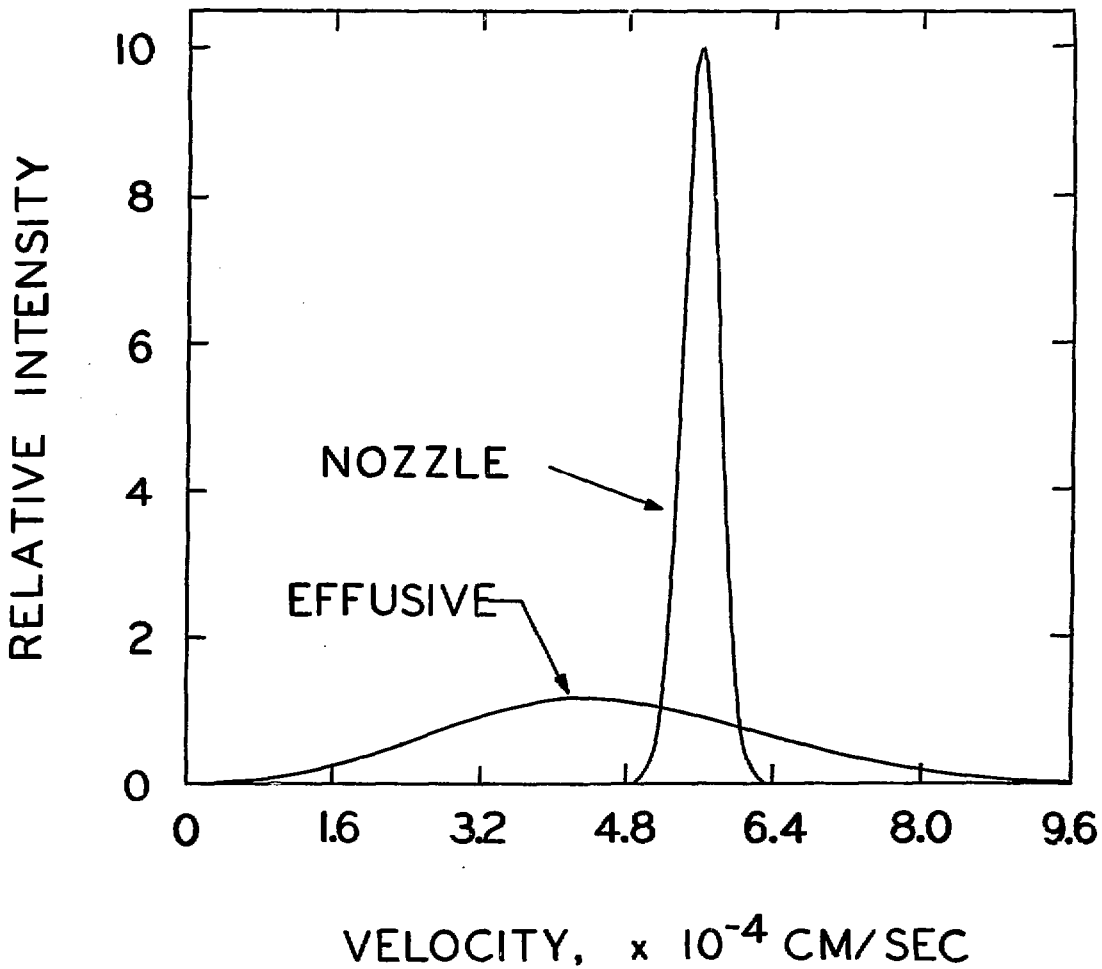

Figure 2

XBL 795-9757

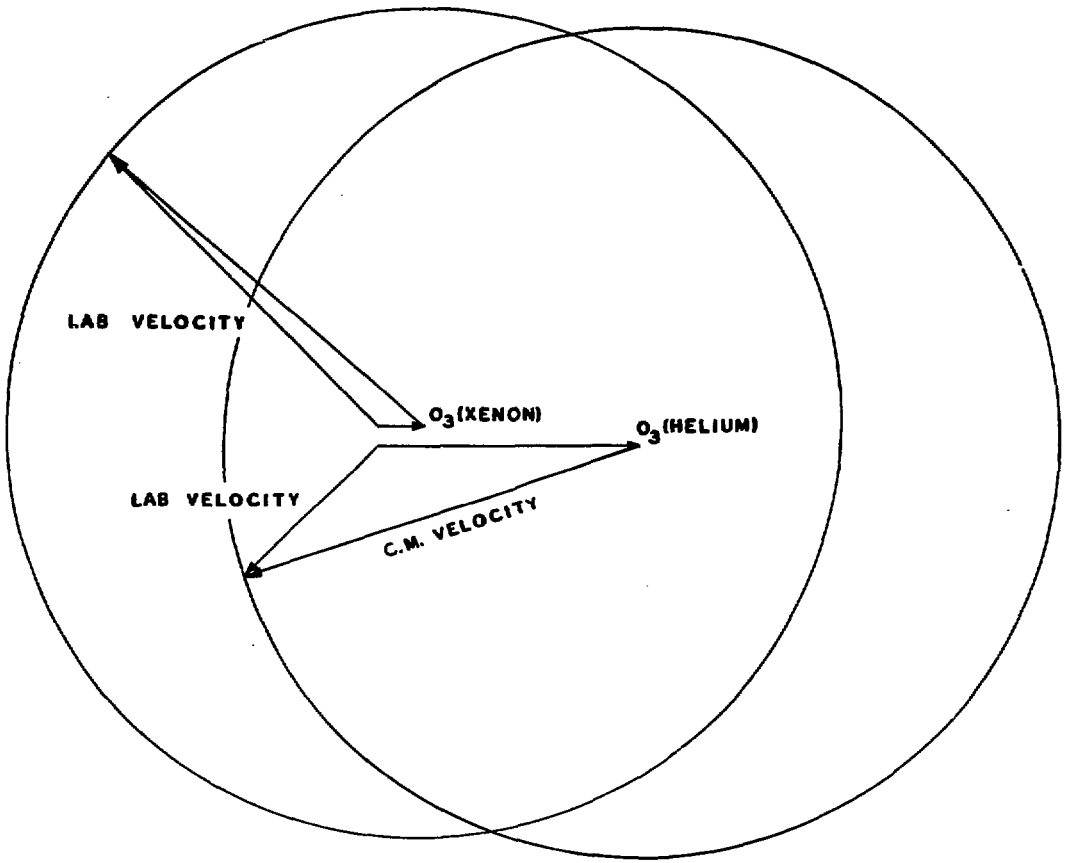

FIGURE 3

XBL 795-9740

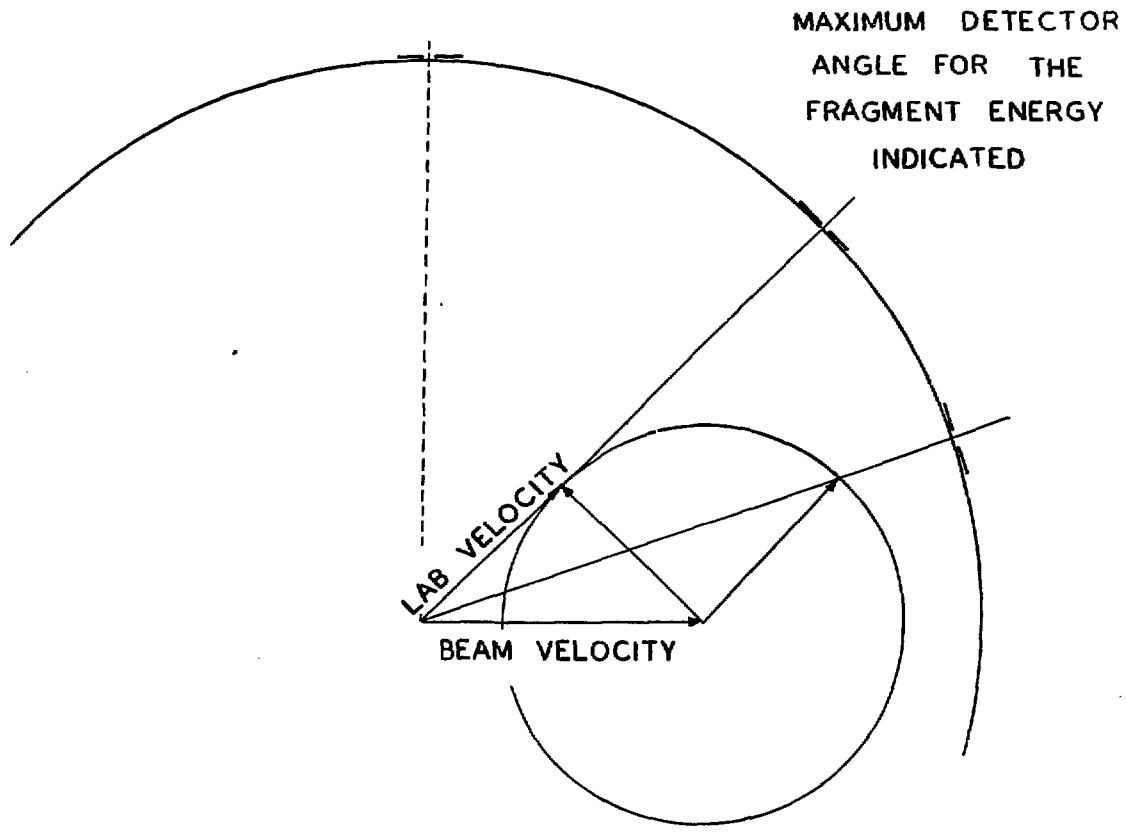

FIGURE 4

XBL 795-9744

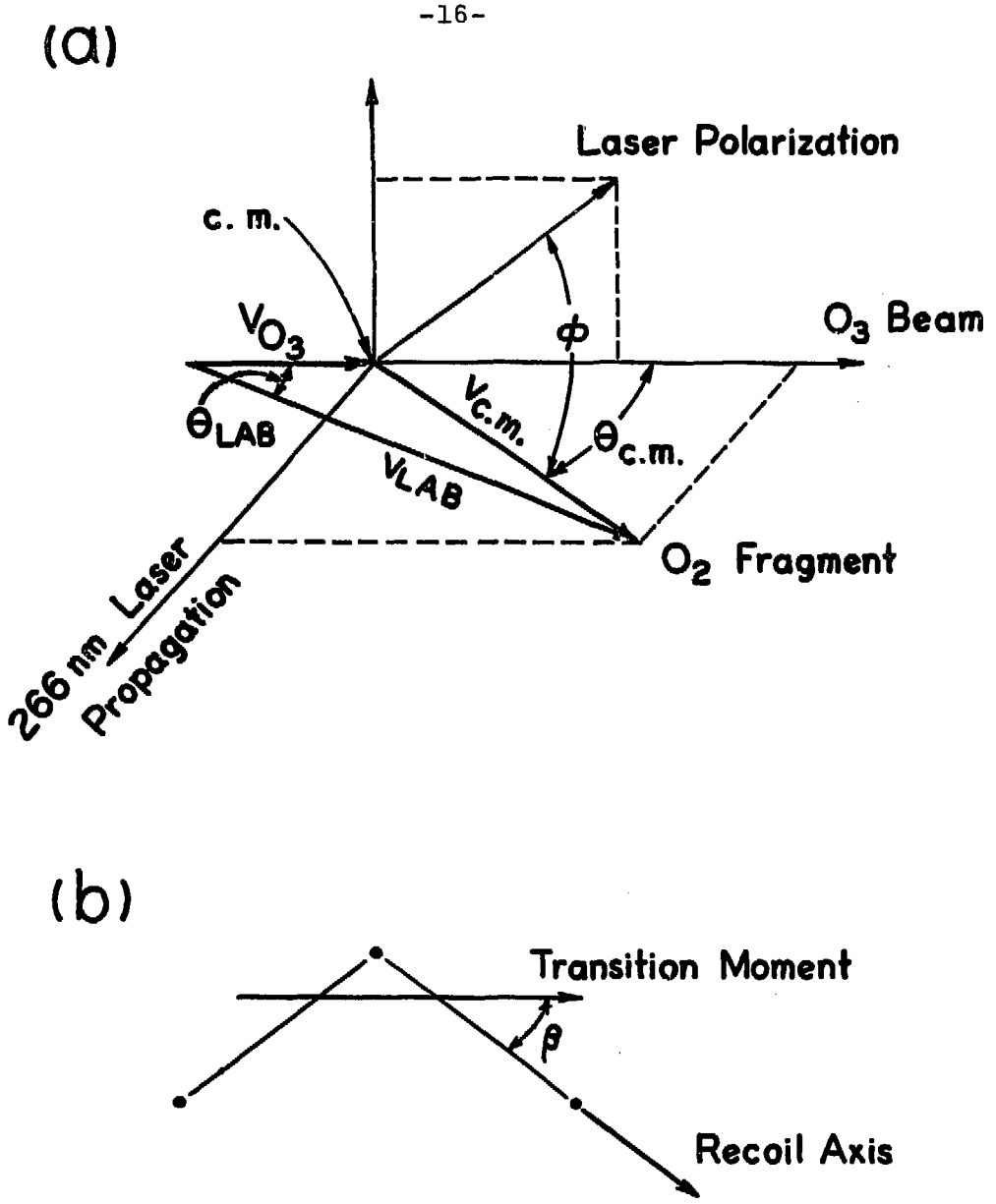

Figure 5

XBL 791-7815 A

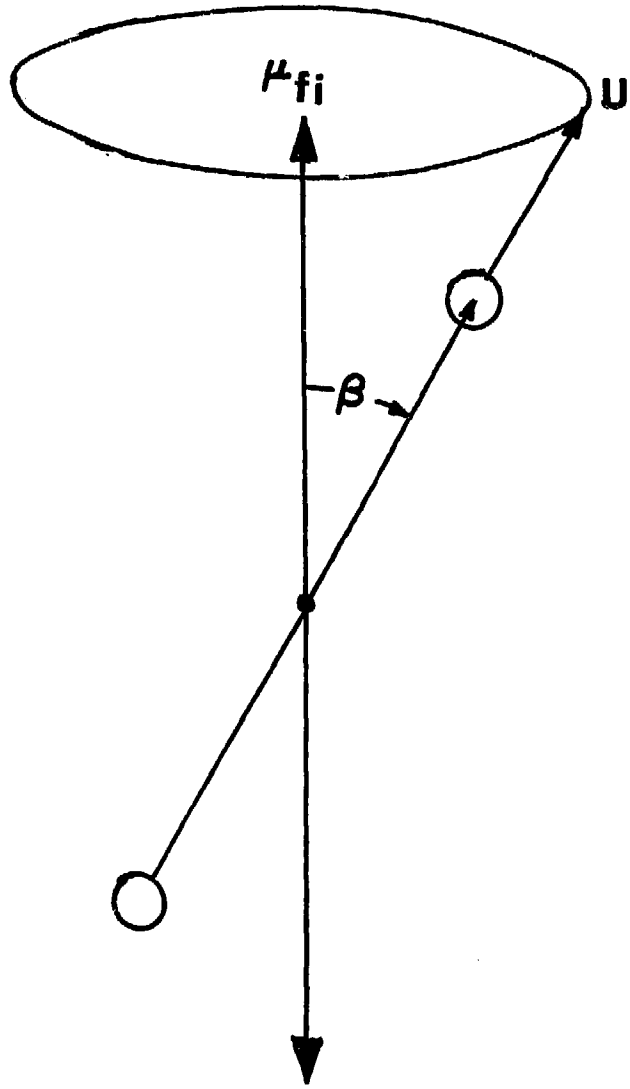

$$b = P_2(\beta_o)$$

XBL 795-9735

Figure 6(a)

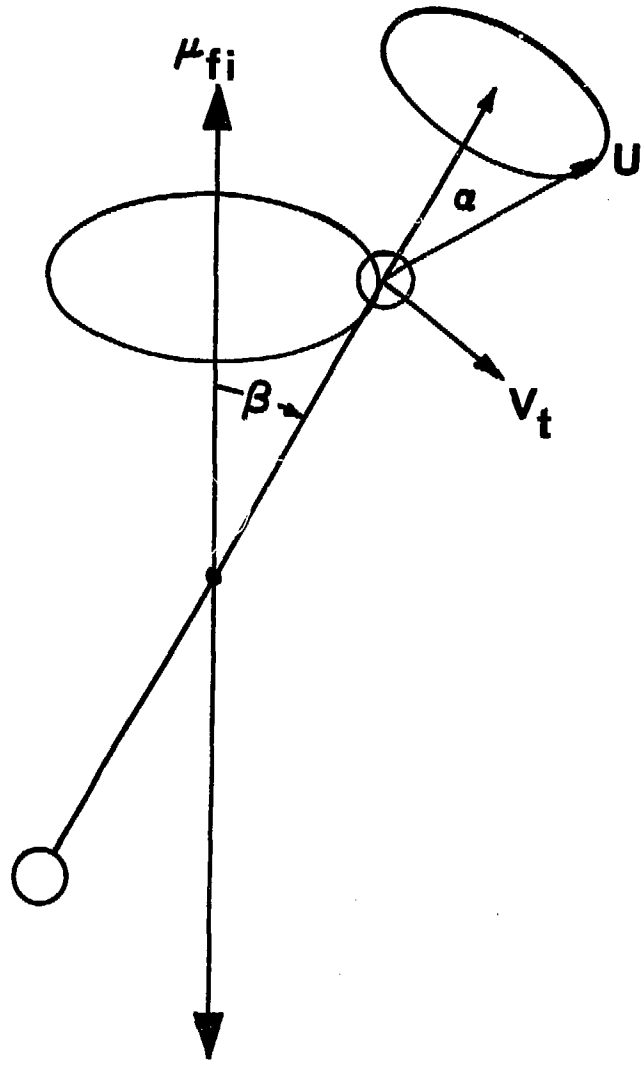

$$b = P_2(\alpha) P_2(\beta)$$

XBL 795-9733

Figure 6(b)

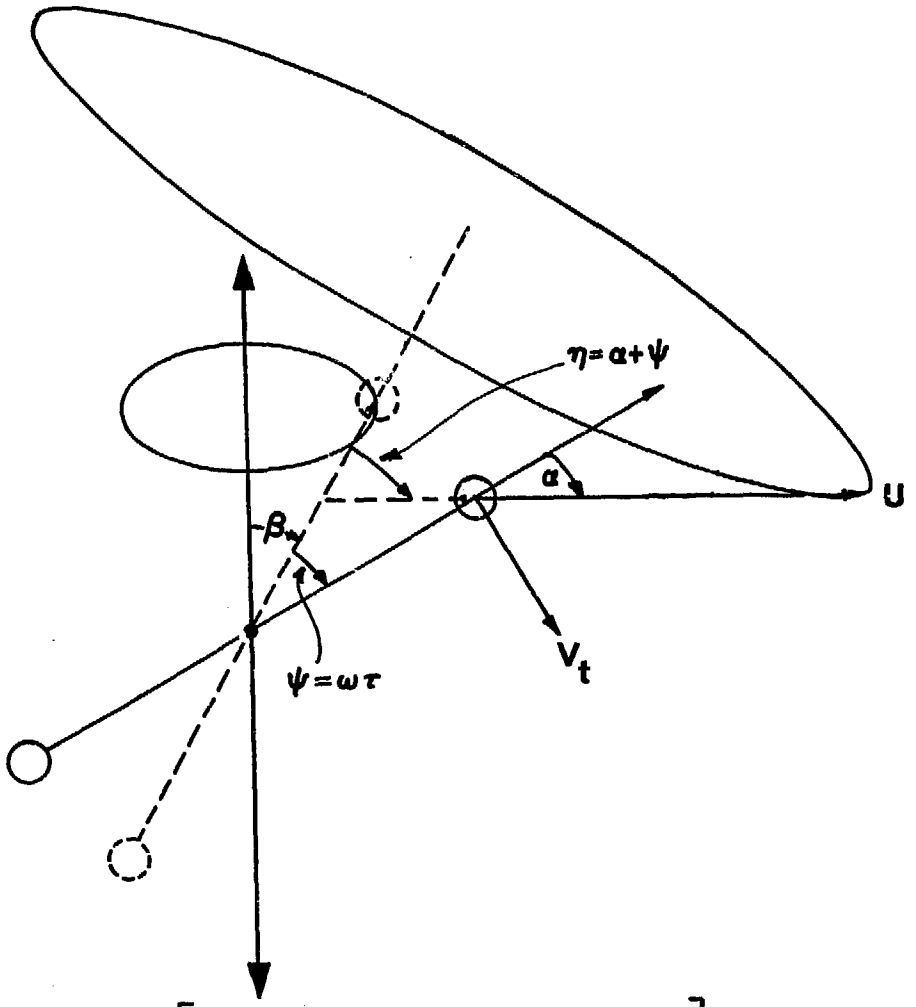

$$b = \left[\frac{P_2(\alpha) + \bar{\psi}^2 - 3\bar{\psi}\,\mathrm{SIN}\,\alpha\,\mathrm{COS}\,\alpha}{1 + 4\bar{\psi}^2} \right] P_2(\beta)$$

XBL 795-9734

Figure 6(c)

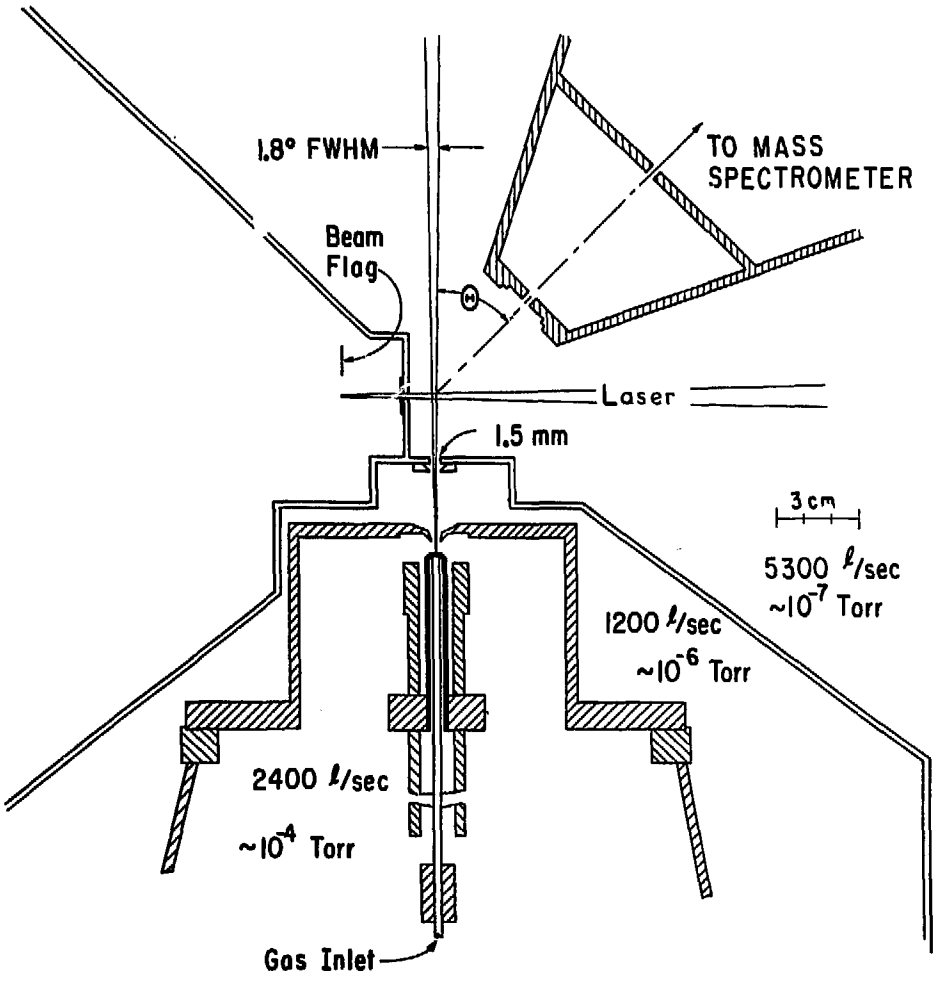

XBL 7512-10181A

Figure 7

II. PHOTODISSOCIATION OF OZONE

A. Introduction

Since the dynamics of photodissociation are poorly understood for systems other than diatomics, we have chosen ozone as a suitable molecule to study. Extensive theoretical efforts have been made on ozone from ab initio approaches,[1-15] and semiempirical studies.[16] Also detailed spectroscopic information[17-24] is available as well as photolytic data[25-40] which renders an extensive base of complimentary information to the studies described here. With such a collection of data, more detailed models for photodissociation can be formulated which address the complexities of nonlinear systems.

The photolysis of ozone is not only important from a theoretical view, but is also an important source of metastable $O(^1D)$ atoms in the atmosphere. $O(^1D)$ reacts rapidly with water to produce OH. The OH radicals oxidize CO to CO_2 as well as affect the concentration of important atmospheric trace quantities. Consequently a measure of the $O(^1D)$ product formation with respect to other possible product states is important.

The quantum efficiency for production of $O(^1D)$ has been estimated to be unity for the process

$$O_3(^1A_1) + h\nu(\lambda < 300 \text{ nm}) \rightarrow O_3(^1B_2) \rightarrow O_2(^1\Delta_g) + O(^1D)$$

Despite the extensive investigations of this process, whether the excited O_3 really dissociate exclusively

to $O_2(^1\Delta_g$ and $O(^1D)$ is still subject to question. Demore and Raper[42] photolyzed ozone in liquid nitrogen at wavelengths between 248 and 334 nm. The production of N_2O decreased by a factor of 2 between 300 and 302 nm. At 334 nm, a further decrease in N_2O production occurred. Thus three different mechanisms seem present at the various wavelengths. No absolute yield for the $O(^1D) + O_2(^1\Delta_g)$ dissociation channel was measured in this work. Demore and Raper[43] later photolysed O_3 in liquid argon where they measured the consumption of O_3 upon radiation of 253.7 and 313.3 nm. Extrapolation to zero concentration of O_3 yielded an intercept from which one may infer the products to be exclusively $O(^1D) + O_2\ (^1\Delta_g)$. The precision in the data however could not give an accurate determination for this quantity. Gas phase photolysis studies have been made by observing the depletion of O_3 in various buffer gasses.[25,44-48] The lack of consistency in these measurements is difficult to assess since the mechanisms for chain reactions in these experiments are still in question. Lin and Demore[49] have studied the relative efficiency of $O(^1D)$ production by monitoring the insertion of $O(^1D)$ in isobutane. Arnold, Comes, and Moortgat[34] have used the chemiluminescence of NO_2 from the reactions

$$O_3 \xrightarrow{h\nu} O_2\ (^1\Delta_g) + O(^1D_2)$$

$$O(^1D_2) + N_2O \rightarrow 2NO$$

$$NO + O_3 \rightarrow NO_2^* + O_2$$

to measure the wavelength dependence of the $O(^1D)$ yield. This technique has been used by others[36,37,50] using laser flash photolysis at various temperatures and wavelengths. All results show a constant relative yield of $O(^1D)$ in the wavelength range 250-300 nm. Amimoto, Force, and Wiesenfeld[51] have photolyzed ozone at 248 nm. using a KrF excimer laser, and monitored the temporal production of $O(^3P)$ using an oxygen resonance lamp. They found no direct photolytic production of $O(^3P)$ and concluded that the absolute quantum yield of $O(^1D)$ is unity at 248 nm. Thus from the relative quantum yields, and this measurement of an absolute quantum yield at 248 nm., it has been concluded that the absolute quantum yield of $O(^1D)$ is unity from 248-300 nm. This is in contradiction, however, with the recent work of Fairchild, Stone and Lawrence[40] who find the quantum yield for $O(^3P)$ to be 0.10 at 274 nm. using a molecular beam technique. The accuracy of their method is hard to estimate but the presence of $O(^3P) + O_2\ (^3\Sigma_g^-)$ is clearly seen.

Table 1 gives the relative $O(^1D)$ production as a function of wavelength from various research groups. Complications in the bulk type measurements can result

from collisional effects which may seriously alter the desired results. The motivation to employ a molecular beam technique is, therefore, obvious.

From spectroscopic measurements it is found that ozone has an ultraviolet spectrum commonly referred to as the Hartley band which is a continuum between 34,000 cm^{-1} and 48,000 cm^{-1} centered at 39,000 cm^{-1} as shown in Figure 1. The structure on the long wavelength tail known as the Huggins band has been attributed to the same electronic state as the Hartley band from the analysis of ab initio calculations. This absorption band is the $^1B_2 \leftarrow X^1A_1$ transition[1,6] which has an unusually high photoabsorption coefficient of k = 108 cm^{-1} base 10 with a 27°C gas temperature at 266.2 nm. Both SCF-CI and generalized valence bond calculations show the $^1B_2$ state has an unsymmetrical equilibrium geometry with as much as 0.7 eV energy lowering when distorting to C_s symmetry. These calculations also show that the equilibrium bond angle is much smaller than the ground state ($^1B_2$ = 108° and X^1A_1 = 117°). Details of the $^1B_2$ surface are still sparse since only a limited number of points have been generated and the surface has not been optimized for all parameters. Thus it is not certain whether this state has a minimum in the potential, or whether it is totally repulsive. Nothing is known about the nature of curve crossings with this state which most

likely exist. Thus it is possible for ozone to be initially prepared in the $^1B_2$ state and then cross to another surface which correlates to different final fragment states. Also avoided crossings could give rise to a predissociative $^1B_2$ system. Low temperature absorption studies of the Huggins band show definite mode structure. This band has been analysed by several workers.[29,53-55] The band structure ends abruptly at 28,450 cm^{-1} in the absorption at 195°K and is assigned the $v'_{000} \leftarrow v''_{000}$ transition. This band is diffuse and degraded toward the red which indicates a system where the bond lengths of the upper state are greater than those of the lower state. This is consistant with the theoretical analysis of the $^1B_2$ state. Also found in the analysis is that only symmetric modes are present. The asymmetric stretch mode is the mode which is expected to mix most strongly with perturbing states giving rise to curve crossings or predissociation.[29] The structure of the Huggins band becomes less pronounced, and disappears entirely in the vicinity of 32,000 cm^{-1}. This corresponds exactly to the onset of $O(^1D) + O_2(^1\Delta_g)$ production from flash photolysis experiments. Thus it appears that the ozone $^1B_2$ state has a dissociation limit or barrier of 10.1 Kcal.

In order to study dissociation dynamics, information on both the lower state and the excited electronic state

is necessary. Detailed ground state information can be obtained by microwave and infrared spectroscopic studies. From the microwave absorption of ground state ozone, it is found that the X^1A_1 state has C_{2v} symmetry with a bond angle of 116.78 $\pm$ .03 degrees, and an equilibrium bond length of 1.2717 $\pm$ .002 angstroms.[24] From the spectroscopic data of the X^1A_1 and 1^1B_2 state, it is likely that ozone undergoes absorption via a non vertical transition (transition takes place outside the Franck-Condon region) in the region of the $^1B_2$ minimum. In the Franck-Condon region, the transition proceeds to a state which is quite high on the repulsive wall of the $^1B_2$ surface, and is well above the dissociation limit. The wavelength with maximum absorption cross section corresponds to 20.2 Kcal. above the asymtotic limit of the $O(^1D) + O_2\ (^1\Delta_g)$ products. Figure 2 shows the energy levels available for the O_2 molecule and O atom. The O_2-O bond energy used is 23.9 Kcals./molecule.[56] The threshold energy (minimum photon energy) for various fragment pairs is shown in Table 2. Although twelve states are accessible with the photon energy used in these experiments (107.5 Kcal.), only four of these states give spin allowed processes. The accessible vibrational energy levels for the $O(^1D_2) + O_2(a^1\Delta_g)$ and the $O(^1D_2) + O_2(b^1\Sigma g^+)$ products are tabulated in Table 3.

From the data available, complemented by the results

of photofragmentation beam spectroscopy, it should be possible to extend our understanding of the dynamics of ozone photodissociation. With this detailed knowledge more refined models for photodissociation in general can be developed.

B. Experimental

Ozone was produced by passing 99.99% pure oxygen through a high voltage discharge. The ozone produced was collected in a 3 liter glass reservoir with teflon stopcocks which contained silica gel. The reservoir was maintained at constant temperature (-80°C) using a dry ice-ethanol slush bath.

A supersonic ozone beam was constructed as shown in Figure 3. An inert gas was passed over the ozone reservoir with a range of backing pressures between 600 and 1000 torr. The reservoir was kept at constant pressure using a dry ice-ethanol slush bath. The exact pressure of the gas mixture obtained was monitored using an MKS Inst. Inc. Baratron Model 221A, 1000 torr head capacitance manometer. The gas mixture then passed through an all glass line with teflon stopcocks to a 10 cm. absorption cell contained in a Beckman model DU spectrophotometer which was used to monitor the partial pressure of ozone. The partial pressure of ozone varied from 8 to 15 torr over extended time

intervals. Corrections for partial pressure variations of the ozone could be made utilizing the monitor output from the spectrophotometer. Due to this variation in ozone partial pressure, argon was chosen as the inert carrier gas since the beam velocity is dependent upon the average mass of the beam as previously described. By using argon whose atomic weight is similar to the molecular weight of ozone, small variations in the partial pressure of ozone would not appreciably affect the average mass. All experiments of ozone were therefore performed with an argon carrier gas. The argon-ozone gas mixture then entered a quartz nozzle which contained a 0.003 inch diameter hole and the nozzle tip to skimmer distance was set at .24 inches. The reservoir and nozzle design permitted all measurements to be obtained with a single ozone charge.

The velocity distribution of the beam was obtained by constructing a chopping wheel which contains a photodiode to monitor the slot position. The wheel was assembled 92 centimeters from the electron impact ionizer of the mass spectrometer and the ions produced were mass analyzed at 80 eV using a quadrupole mass spectrometer. The total flight time from the chopping wheel to the detector was measured using a 255 channel multichannel scaler which has a variable sampling time per channel from 1 to 99 micro-

seconds. The scaler was interfaced to a Digital Equipment Corporation LSI-11 microcomputer to allow ensemble averaging of the data.

Figure 4 shows the time of flight spectrum of ozone with a partial pressure of 12 torr seeded in 980 torr of argon. The velocity distribution obtained is fit to the equation

$$\frac{dn}{dv} = C\, v^2 \exp\left(-\frac{\bar{m}}{2KT_s}\right)(V-V_s)^2 \qquad (1)$$

Time of flight measurements were obtained for several argon backing pressures. A suitable beam was obtained using 580 torr argon and 10 torr ozone. This produced a translational temperature Ts of 2°K, and a most probable velocity, V_s of 55,800 cm/sec. This corresponds to a beam mach number of 19.8.

By utilizing defining slits in the beam, a well-defined spatial distribution of the beam can be obtained. Using the geometry shown in Figure 5, a beam width of 0.50 cm was obtained with an angular distribution of 2 degrees.

The photoexcitation source was based on a Quanta-Ray Corporation Nd^{+3}YAG laser which produced 1×10^{-8} second pulses in a Q switched mode. 200 mjoules were obtained for the laser oscillator which was increased to 700 mjoules by employing an amplifier. Laser output power was measured using a Scientec Corporation Model 362 thermopile detector.

The output beam consisted of an annular ring profile (due to the unstable resonator design)with an intensity profile as shown in Figure 6, having a beam divergence of <1.0 m radians, and diameter of 6mm.

In order to obtain the desired ultraviolet radiation, the λ = 1064 nm. laser beam was directed onto a 3 centimeter potassium dihydrogen phosphate (KDP) frequency doubling crystal. Phase matching conditions for frequency doubling were obtained by angle tuning. 0.200 joules per pulse of 532 nm radiation was obtained in this fashion. The 532 nm radiation produced was frequency doubled with a 2 centimeter KDP crystal in a similar manner to produce $1x10^{-8}$ second pulses of 266 nm radiation with 0.05 joules per pulse. The primary, doubled, and quadrupled output frequencies were separated using a fused silica prism so that only the ultraviolet source crossed the ozone beam. To obtain optimal overlap of the laser beam with the ozone beam, a 2 meter focal length quartz lens was employed. Unfortunately, the focal point coincided with the back wall of the crossed beam facility and generated copious quantities of background products. (See Figure 7) Various focusing schemes were tried but the most reliable results were obtained using an unfocused laser beam.

In this final arrangement, background runs were obtained with the molecular beam blocked to insure that no signal was obtained which was time correlated to the laser pulse. A similar and redundant experiment was performed by blocking the laser beam to verify that no electrical noise gave rise to false signals. In both cases, no time correlated signal was obtained.

Due to self absorption in the KDP quadrupling crystal, the laser power tended to vary during the course of an experiment. The self absorbed radiation caused crystal heating which in turn changed the refractive indices of the birefringent crystal. The optical phase conditions were therefore altered. An uncoated piece of quartz was therefore used to split a small fraction of the light for constant power monitoring using the thermopile detector. The power was manually adjusted to maintain the power level to within 5% of the maximum.

The vacuum window was made of optical quartz. Since diffusion pumps were used in the vacuum chamber, it was necessary to construct a shield for the window so that oil residue did not accumulate. The shield consisted of a long tube with a shutter at the end, enclosing the window when experiments were not in progress. Even with this precaution, photodeteriorization of the window due to traces of oil was

present, although minimal.

The photofragment time of flight spectrum was obtained using the same multichannel analyser used in the beam velocity distribution measurements. The synchronization of the laser pulse was achieved using a fast photodiode and amplifier. The pulse obtained, however, did not generate an amplitude compatible with the multichannel scaler which required +5 volts. The amplified pulse was sent to a Data Pulse Corporation Model 101 pulse generation unit which supplied the required pulse amplitude and pulse width. The delay time of the pulse was measured with a Tektronics 585 oscilloscope with a 1A1 plug in amplifier and was determined to be 100 nanoseconds. Since this is only 10% of the smallest time interval possible per channel, we have disregarded this delay. The shortest dwell time per channel in the ozone measurements was 3 microseconds and the shortest flight time observed was 140 microseconds; hence,only a 3% error in flight time is introduced in the first channel, and less than 0.1% error is introduced for observed fragment from this propogation time.

Since the fragments were measured with an ion detector, it was necessary to study the effect of the ionizer on the velocity distribution. At lower ion extraction energies, due to ion trapping, one finds that the fragments are delayed, thus introducing a broadening effect. By

applying a higher extractor voltage to the ionization region, the ions are removed more efficiently. With a higher extractor voltage, the electrons are confined to a smaller region near the front of the ionizer. The result gives a smaller flight time with a narrower time distribution; however, this advantage is offset by a loss in signal.

When utilizing a supersonic nozzle, it is extremely important to determine whether van der Waals molecules are contributing to the measurement. When the photofragment spectrum of ozone was obtained (mass 32 detected) using 1000 torr argon backing pressure, a large signal was observed which peaked at the minimum observable velocity at the laboratory angle used (see Figure 8). By adjusting the mass spectrometer to mass 48, we tried to determine if any ozone van der Waals complex was the source of this peak. Figure 9 shows that ozone is indeed scattered in the photodissociation process, implying that van der Waals complexes are present in the beam. By decreasing the argon pressure to less than 600 torr, the slow velocity component of the time of flight spectrum is eliminated. Figure 10 shows the time of flight spectrum of ozone using 13 torr partial pressure of ozone and 580 torr of argon. Normal operating parameters are summarized in Table 5. In order to achieve

the desired signal to noise ratio, 100,000 laser pulses were used and the data was ensemble averaged in the LSI-11 microprocessor. The averaged data was then stored on magnetic disks for future data processing.

To obtain the dependence of the angular distributions in the E vector of the radiation field, a half wave retardation wave plate obtained from Karl Lembrecht Corporation was used to rotate the polarization of the input radiation. The polarization angle rotates twice as rapidly as the half wave plate.

To determine the absolute orientation of the optical axis, a UV polarized filter was placed after the polarization rotator. The polarization angle was varied until a minimum intensity was observed through the UV polaroid filter. The absolute orientation of the polarization angle was determined to within $\pm$ 5°. This was found to be adequate for these studies. The anisotropy data were then taken at 6° intervals of polarization in the LAB frame as shown in Figure 11.

To insure that saturation effects did not obscure the anisotropy data, it was also necessary to determine that the quantity of dissociation products was still linearly dependent upon the laser input power. The power dependence was obtained by integrating the values of 10 channels around v = 0 of the O_2 ($^1\Delta_g$) (as described later).

The laser power was varied between 13 and 45 mjoules per pulse. The results are shown in Figure 12 which verifies that the photon saturation level has not been reached.

C. Results

To determine the distribution of the rotational energy in each vibrational state, it is first necessary to evaluate the resolution of the time of flight spectrometer. Using the parameters of Table 4, a Fortran IV computer program was developed to simulate the photofragmentation process. A listing of the program is included in Appendix A. Included in Figure 13 are single energy fragments of equal probability at 2, 5, 10 and 15 Kcal which have been convoluted with the various distribution functions of the apparatus with the proper transformation Jacobian applied.[57,58] The results show the non uniform response of equally partitioned energy as it is measured in time space.

In order to conserve flux in the transformation from center of mass velocity, u, to laboratory velocity, v,

$$I_{LAB}(\theta,v)du = \frac{v^2}{u^2} I_{c.m.}(\theta,u)du$$

is used.[57,58] The analysis is most convenient in the center of mass energy coordinate frame. Thus we desire

$$I_{c.m.}(\theta,v)du = I_{c.m.}(\theta,E)dE$$

Since $E = 1/2\ mu^2$, and $du = dE/mu$, substitution for du yields the desired Jacobian v^2/u. The efficiency of the electron impact ionizer is proportional to 1/v. After compensating for this factor, the final flux conserving transformation becomes

$$I_{LAB}\ (\theta,v)du = \frac{v^3}{u}\ I_{c.m.}\ (\theta,E)dE$$

An additional factor arises if "delta functions" are used as energy input. When the transformation is made to time space, an unequal density is obtained for the histogrammed result at different energies. After compensating for this factor, the synthesis of time of flight spectra can be generated using the program described in appendix A. From Figure 13 one also observes the inherent resolution of the apparatus.

If the time of flight data are transformed to center of mass coordinates using a direct inversion process from a single Newton diagram, the results of this transformation gives an improper weighting of the energies. For an accurate estimate of the center of mass energy distribution, it is necessary to deconvolute parameter distributions of the apparatus which degrades the experimental resolution. The process of deconvolution is inherently an ill conditioned mathematical process[59-64]

and is not a viable approach. Convolution, however is a numerically stable process. In order to obtain the center of mass energy distribution, a trial energy distribution can be generated which is convolved using the convolution integral generated as described in Appendix A. After transformation to a time distribution, the results are compared to the original time of flight data. The trial distribution is modified until a reasonable fit is obtained. The fit obtained is not unique, but other distributions obtained which fit the data well can be ruled out as physically unrealistic such as distributions containing negative energy probabilities. Alternatively, one can generate the energy distribution by means of a multiple linear regression technique. One finds that complications arise from the non uniform spacing of data after the transformation from time to energy space. Hence if an equal spacing in energy is assumed in order to generate the convolution distributions in time, one finds that there are more coefficients sought than time of flight variables at high energies whereas many data points exist with relatively few energy coefficients at low energies. The consequence of this situation is that the regression gives reasonable coefficients at low energies with large residual root mean squared error, and unreasonable coefficients at high energies with little or no residual root mean squared error. The trial and error fitting procedure was therefore used for these studies. A

comparison of the direct inversion to center of mass process, and the center of mass energy distribution obtained by a trial and error fitting procedure is shown in Figure 14. The fit obtained with respect to the original data is shown in Figure 15.

The center of mass distribution obtained shows an appreciable continuous signal at low recoil energies, the existence of which is difficult to rationalize from the standpoint of photodissociation dynamics. Since ozone is a bent triatomic molecule, when significant energy is released as translation it is necessary that a considerable portion of the excess fragment energy be partitioned into rotation based on the conservation of angular momentum. Since the initial angular momentum of ozone is small, in the fragmentation process large orbital angular momentum L' should be compensated by the molecular angular momentum of O_2 ($^1\Delta_g$), namely, $J = j = L' + J' = 0$. Consequently, $L' = \mu g b' = J'\hbar$ where μ is the reduced mass, g is the relative velocity of the fragments, and b is the exiting impact parameter. Since the range of exit impact parameters is limited by the nuclear orientation of the parent molecule, only a narrow distribution of J values for the diatomic fragment are permitted. The energy in each vibrational state is calculated by[65]

$$E_{Vib} = \omega_e (V + 1/2) - \omega_e X_e (V + 1/2)^2 + \omega_e y_e (V + 1/2)^3$$

The rotational energy for each J state was obtained from

$$E_{Rot} = J (J + 1) B_v \text{ where } B_v = B_e - \alpha_e (V + 1/2)$$

All higher order terms are negligible. By simultaneous conservation of both energy and momentum, the exiting impact parameter for each rovibrational state of the O_2 fragment can be obtained from

$$b = \frac{J\not{h}}{\mu} \left[\frac{2(E_{Photon} - E_{Bond} - E_{Vib} - E_{Rot})}{\mu}\right]^{-1/2}$$

Figure 16 gives the impact parameter vs. J for the four accessable vibrational states of $O_2(^1\Delta_g)$ in these experiments. From conservation rules again, the most probable J for each vibrational level is obtained for the $O_2(^1\Delta_g)$ manifold. v = 0, 1, 2, and 3 yield most probable J's of 23, 16, 14 and 14 respectively. The corresponding exit impact parameter for each is also shown in Figure 16. The rotational energy distribution for each vibrational state should show a correspondence to the distribution of nuclear configurations found in the excitation process. For v = 0 and v = 1, this correspondence is observed to be reasonable. The large continuous signal from 3 to 5 Kcal of kinetic energy gives exit impact parameters of approximately 2.0, 1.4 and 1.2 angstroms for v = 0, 1, and 2 respectively at 3 Kcal. A distortion to C_s symmetry is required as well

as fragmentation deviating considerably from the internuclear bond axis. This would not be likely in an impulsive dissociation which is verified from the polarization dependent data. It is therefore likely that the large continuous feature from 3 to 5 Kcal is due to an artifact. The existance of an artifact is further supported if one analyses the slow decay of the low energy tail. The phase space configuration of the fragmenting molecule for these energies should have low probability which is not consistant with the center of mass distributions obtained. This type of tail has been observed by other authors[66] and also in our CH_3I photodissociation studies. The possible cause is photofragment trapping in the ionizer. By fitting the data for the 20°, 30°, and 50° runs and scaling with respect to the polarization results, one finds that the most probable energies for each vibrational level exhibit large anisotropic scattering whereas the continuum from 3 to 5 Kcal., and the low energy tail contain little or no anisotropy which supports the premise of particle trapping. (see Figure 17.)

The slowly decaying tail was fit to an exponential form, and the lifetime found to be 375 microseconds. This exponential function was then convolved with a set of four gaussian functions which closely approximate the distribution of the four vibrational states observed. The resulting

function was scaled to the original data in the region of the slow tail, as shown in Figure 18. This result was then subtracted from the original data to yield a close estimate of the actual time of flight form. Figure 19 shows the time of flight distribution obtained after correction of the underlying artifact.

The corrected time of flight data for θ LAB = 20, 30, and 50 degrees was transformed to center of mass energy space as described earlier with no polarization dependence incorporated in the simulation program. The intensity of each of these distributions has been normalized using the polarization data from Figure 11 since the center of mass angle is different for all of the runs. The intensity normalized results are shown in Figure 20. It is now necessary to correct this distribution due to the different rate of change in polarization angle as a function of energy. Since the center of mass angle (in this case equivalent to the polarization angle) does not vary rapidly over a single vibrational distribution, and since the polarization dependence ($\cos^2\theta$) is a slowly varying function, it is possible to apply a single polarization correction factor over an entire vibrational peak without appreciable error. This process was performed for all vibrational states, for each laboratory angle. Using the polarization dependent

scattering form

$$W(\theta) = A\left[1 + 2b(E)\ P_2\ (\theta)\right]$$

the value of b, and the product ratio for each vibrational state is obtained. It is found that b(E) varies from level to level with no apparent trend. Due to the uncertainty in obtaining b(E), it is not possible to obtain a functional dependence for b(E). b(E) was found to be 0.46, 0.38, 0.55, and 0.53 for V = 0, 1, 2, and 3 respectively. An average value is obtained of 0.48 To check the consistancy of the fit, the simulation process was repeated incorporating polarization factors using the average value of b obtained. One energy distribution should thus give a good fit to any lab angle time of flight spectra. The polarization corrected energy distribution is shown in Figure 21, and the quality of the fit for the 30° lab angle is shown in Figure 22. It can be seen that b is not a constant value.

It is now possible to obtain the relative energy partitioning for the four vibrational levels by integrating the area under each product peak obtained using the four separate values of b. The results of this integration give 57%, 24%, 12%, and 7% for v = 0, 1, 2 and 3 respectively, which corresponds to an average thermal vibrational temperature of 2700°K.

As seen in Figure 10, a small signal is observed with a 150 microsecond flight time which yields 45 Kcal of

fragment energy. The only means of obtaining fragment energies of this magnitude is by the formation of ground state electronic fragments $O(^3P) + (^3\Sigma_g^-)$. This reaction channel has been unobservable in every experiment except the recent results by Fairchild et al[40] who employed a beam technique similar to that described here, whereby they observed 10% product yield to the ground state. In their studies, a chemiionization detector was used from the reaction

$$O + Sm \rightarrow SmO^+$$

The relative efficiency of $O(^3P)$ to that of $O(^1D)$ for chemiionization is not totally characterized, and thus the absolute quantum yield is still uncertain. The result obtained in the present study, by integrating the polarization adjusted energy distribution from the direct inversion process, (Figure 23) yields 12% product formation to $O(^3P) + O_2(^3\Sigma_g^-)$. The accuracy of this result is predicated on the assumption that the efficiency for electron impact ionization is constant for all internal states. To verify this hypothesis, one can repeat these experiments and detect the oxygen atom product (although the background signal is higher). The only internal state factor then present would be the relative efficiency of $O(^3P) + e^- \rightarrow O^+ + 2e^-$ and $O(^1D) + e^- \rightarrow O^+ + 2e^-$. Until these measurements are made, precise absolute values for the

energy partitioning both for the electronic and vibrational states cannot be made. Thus no error limits are reported here although a highly non uniform ionization efficiency factor and/or fragmentation ratio (O_2^+/O^+) is not likely at the ionization energies used (200 eV) since the vibrational excitation energy is small compared to the dissociation energy.

Discussion

Theoretical models of photodissociation processes have ranged in complexity from purely classical descriptions to complete three dimensional quantum dynamic descriptions. Early photodissociation models, both semiclassical,[67,68] and quantum mechanical[69-75] utilized a quasidiatomic picture. In this model, the dissociative state coordinate is assumed to be a normal mode of vibration of the initial electronic state (In this work the ground state of the ozone molecule). Thus interactions due to the recoil fragments are the only mechanism to promote distribution changes other than Franck-Condon factors in the internal energy in the quasidiatomic model. More recent models have utilized a polyatomic Franck-Condon approach [76-78] and have treated effects of multiple coupled continua.[79-81] The formalism is completely described. A detailed theoretical description of HCN and ICN has been made by

evaluating multidimensional bound-continuum Franck-Condon amplitudes between the initial bound state wavefunction and wavefunctions for the repulsive surface.[76-78] Further refinements have been made on ICN by treating continuum-continuum interactions[81] which were found to be significant only for high vibrational states, and the results agree well with experimental results. A full treatment of this type has not as yet been carried out on a nonlinear triatomic molecule where a complete three dimensional analysis is necessary.

Due to the computational complexity of the full quantum dynamics approach, alternative methods have been proposed to elucidate qualitatively the dynamical processes in a photodissociation event. Semiclassical approximations have been used,[82-84,92] and a comparison of these approaches has been carried out to test the validity of the approximations used.[78] These semiclassical techniques can be useful in calculations of large molecules where the potential surface for the repulsive electronic state is seldom well known. Such approaches would be quite suitable for the analysis of ozone, when further data on the wavelength dependence for photofragment energy partitioning is available. An exact time dependent formulation of the photoabsorption process has been developed[85,86] which is analogous to the Franck-Condon approach. The results of this study showed that the

influence of short time effects permits a purely classical expression to be used for the photodissociation cross section. Classical photodissociation models have been used for a long time in the analysis of continuous spectra by means of a classical Franck-Condon, or reflection method.[87-91] A more sophisticated classical approach using a Wigner distribution of classical particles has been used for dissociative attachment studies.[93] The reflection method and these variations are based on a diatomic or quasidiatomic model which cannot be applied to bent triatomics. Recent analysis of quantum corrections to classical photodissociation has shown, however, that the classical reflection method can be generalized to polyatomic molecules.[85]

The information on the $^1B_2$ surface of ozone is sparse,[1] although it seems feasible to obtain a suitable accurate potential surface if further theoretical work is done so that dynamics calculations can be obtained. In lieu of such studies, some qualitative features of the photodissociation dynamics can be developed. If continuum-continuum coupling is small, then the formulation of a reasonable photodissociation description should be possible for ozone using Franck-Condon arguments. Recent analysis of AB_2 systems has been done in this way to describe the structure in

photoabsorption spectra[94] of AB_2 molecules. If no vibrational coupling exists, then such an analysis should also explain the vibrational product state distribution.

To describe the photodissociative absorption process for a symmetric AB_2 molecule, a typical ground electronic state surface as shown in Figure 24 is expected. The upper electronic surface is described as shown in Figure 25. Shown in both these figures is the direction of the normal vibration coordinates of the ground state (symmetric and asymmetric stretch). The line Z represents the reaction coordinate, and X describes vibrational motion perpendicular to Z. X yields the vibration coordinate for AB (O_2 for ozone) in the asymtotic limit. At the top of the barrier, X and Z are found to lie parallel to the symmetric and asymmetric coordinates of the ground state even though the saddle point may be displaced outward from the ground state minimum. Assuming that the absorption process is vibrationally adiabatic and one obtains the absorption cross section from the product of Franck-Condon factors, then

$$\sigma(\omega) = C\omega \sum_{v_f} |\langle \chi(z,E_{zf})\ \chi(x,v_f)\psi_f |\ u\ |\ \psi_i \chi(x,v_i)\chi(z,n_i) \rangle|^2$$

where v_i and v_f are the initial and final quantum numbers in the x direction, n_i is the initial asymmetric stretch vibrational quantum number, and E_{zf} is the energy available

for the unbound motion along the Z direction. The sum is over all v_f accessible with photon frequency ω. This may be simplified to

$$\sigma(\omega) = C\omega\,(u_{fi})^2 \times \Sigma |< \chi\,(z,E_{zf})|\chi(z,n_i)><\chi(x,v_f)|\chi(x,v_i)>|^2$$

if the completely symmetric coordinate has a negligible effect on the dipole matrix element. Since the wavefunction for the ground state surface is localized near the potential minimum, strong Franck-Condon overlap will occur only in this spatial region. Figure 26 shows a cut through the X (symmetric) axis at the barrier of the upper surface. If the saddle point is displaced as shown, a maximum overlap will occur for some vibrational state (v = 4 in this example) and diminish as one moves away from the ground state maximum. Thus v = 0 in the upper state for this example has a small overlap integral and would not be expected to possess a high absorption probability. Figure 27 represents cuts along the reaction coordinate Z with S = 0 and X = 0. The amplitudes of three vibrational continuum wavefunctions are shown. If ω is small, one finds that negligible overlap occurs, and if ω is large, the upper state wavefunction contains rapid oscillations and cancellation occurs. In the region of the barrier, however, large overlap is found to occur. The transition probability is shown in Figure 28 as a function of energy using the example shown. One finds that the

transition probability is therefore sharply peaked at the potential barrier. If the distribution of Figure 28 were infinitely narrow, then the photoabsorption spectrum could be interpreted as a one-dimensional, bound-bound Franck-Condon absorption in the symmetric stretch coordinate. The reaction coordinate would serve as a line broadening mechanism. Since the distribution of Figure 28 is so sharply peaked, this one-dimensional Franck-Condon description should give a reasonable picture of the $^1B_2$ surface of ozone for the symmetric coordinate in the case of a vertical transition if the photon energy exceeds the barrier height. The photofragment experiments were carried out on the low frequency side of the absorption maximum and show a monotonic decrease in product yield with increasing vibrational level. This would indicate that the saddle point is not displaced from the position of the ground state minimum, if no V-T mixing occurs in the fragmentation dynamics. If wavelength dependent photofragment results are obtained, the exact position of the saddle point can be obtained. This qualitative analysis explains both the structure in the photoabsorption spectrum and the trend in the vibrational energy distribution of the O_2 photofragment. Since the barrier height is not known it is possible that the photon energy is below that which is required to reach the top of the barrier. In this case, the transition

must occur away from the barrier and thus creates circumstances favorable for a non vertical transition. The Franck-Condon factors will thus be dominated by the wavefunction of the asymmetric (reaction) coordinate of the upper surface, and the classical reflection method would produce a profile more representative of the repulsive reaction coordinate. This view is also consistant with the product vibrational distribution as shown in Figure 21. Presently the distinction between a vertical and non vertical transition cannot be made without more detailed information. It should be mentioned that this model may also be extremely over simplified. If the reaction coordinate has sharp curvatures then little resemblance will exist to the initial asymmetric mode. A double minimum type potential would be expected which exhibits grossly different vibrational wavefunctions from those of Figure 27. Finally the assumption that the half reaction is vibrationally adiabatic may be invalid. Quantitative theoretical analysis to address these questions will be possible only after the $^1B_2$ surface has been reasonably characterized.

The rotational distributions of the fragment diatomic can be treated using a classical model. Since the photodissociation experiments were performed with a cold (less than 10°K) source, neglecting the residual rotational

motion of the ozone is insignificant compared to the contributions from excess recoil energy. The fragment rotational energy can be calculated as described on page 39 if vibrational coupling is negligible. Neglect of vibrational mixing has been used in the analysis of NOCl, and NO_2 using a modified impulsive model and has given good agreement with experimental results.[66] This model assumes that all of the available energy

$$E_{AVL} = E_{Photon} - E_{Bond} - E_{electronic} - E_{vib}$$

appears at the beginning of the dissociation as repulsive potential energy between atoms of the fragmenting bond. It is assumed that the force is impulsive on the time scale of rotation but will not allow energy transfer to vibrational modes. Thus partitioning between rotation and translation is dependent on E_{avl}, reduced masses, and angle by

$$E_r = \sin^2 x \left[(1-u_a/u_f)^{-1} - \cos^2 x \right]^{-1} E_{avl}$$

$$E_t = E_{avl} - E_r$$

where E_r is the rotational energy of the O_2 fragment, E_t is the relative translational energy of the two fragments, x is the O-O-O bond angle, u_a is the reduced mass of the O and O atoms, and u_f is the reduced mass of the O and O_2 fragments. If the bond lengths of the O_3 molecule are fixed at their equilibrium distance, the classical turning point

for the bending motion can be obtained from

$$V = \frac{1}{2} f_r (\Delta r_1^2 + \Delta r_2^2) + f_{rr}, \Delta r, \Delta r_2 + f_{r\theta}(\Delta r_1 + \Delta r_2)\Delta\theta + 1/2\, f_\theta \Delta\theta^2$$

where $f_r = 2.99$; $f_{rr} = -1.68$; $f_{r\theta} = 0.417$; and $f_\theta = 7.66$ mdyn/A. for ozone.[24] This gives turning points of 114.8°, and 118.7° since the equilibrium angle is 116.78°. The rotational energy has been calculated for various nuclear configurations for each vibrational state as well as the equilibrium geometry and the results are tabulated in Table 5. If the translational energies calculated from this impulse model are compared with the experimental results (Figure 21), one finds that the most probable energy for each vibrational level is in good agreement. The width of the energy distribution obtained from the impulsive model is much narrower than the experimental results, however. Such spreading can be attributed to effects such as variations in bond lengths, transverse velocity (perpendicular to the fragmenting bond) due to vibrational motions, finite lifetime of the $^1B_2$ state, and coupling of vibrational energy. Regardless, the impulsive model is capable of predicting the major features of the O_3 fragmentation process.

Since the impulse model agrees well with experiment for the energy partitioning of the photofragments of ozone, an

impulsive description of the polarization dependence should also hold true. The anisotropic scattering in this case would be given by

$$W(\theta) = A\left[1 + 2bP_2(\theta)\right]$$

where $b = P_2(\beta)$.

Substituting $P_2(\beta)$ for b gives

$$W(\theta) = A\left[\cos^2\theta + \frac{\sin^2\beta}{2-3\sin^2\beta}\right]$$

where β is the angle of the axis of the fragment recoil with respect to the transition moment. From the polarization data (see Fig. 11) a value of .46 is obtained for b which corresponds to 36.9° for β. Thus in an impulsive treatment, the upper state bond angle is found to be 106.2° which compares well with the results of ab initio calculations. A 106.2° bond angle gives reasonable agreement with experimental results for the energy distribution when the impulsive model is maintained. From an impulsive approach then, evidence for a non vertical transition to the upper state surface might exist.

From the above analysis, one finds that a good qualitative description of the ozone photodissociation dynamics can be obtained from simple classical models which require little detail about the upper state potential surface. More refined details will require a complete

three dimensional analysis at which time treatment of the product branching to ground state products can also be addressed. Measurements of the wavelength dependence for product energy distribution will certainly aid in the analysis of this photofragmentation system. A detailed potential surface can then be constructed, curve crossings established, and questions can be resolved on the relative importance of continuum-continuum coupling vs. Franck-Condon factors.

FOOTNOTES

1. P. Jeffrey Hay and Thom. H. Dunning, Jr., J. Chem. Phys., 67,2290 (1977).

2. Albert K. Q. Sui and Edward F. Hayes, Chem. Phys. Lett. 21,573 (1973).

3. James S. Wright, Can. J. Chem. 51,139 (1973).

4. Shingkuo Shih, Robert J. Buenker, and Sigrid D. Peyerimhoff, Chem. Phys. Lett. 28,463 (1974).

5. P. J. Hay and W. A. Goddard, Chem. Phys. Lett. 14,46 (1972).

6. A. Devaquet and J. Ryan, Chem. Phys. Lett. 22,269 (1973).

7. Robert R. Lucchese and Henry F. Schaefer III, J. Chem. Phys. 67,848 (1977).

8. P. Jeffrey Hay, Thom. H. Dunning, Jr. and William A. Goddard III, J. Chem. Phys. 62,3912 (1975).

9. P. Jeffrey Hay, Thom. H. Dunning and William A. Goddard III, Chem. Phys. Lett. 23,457 (1973).

10. Stephen Rothenberg and Henry F. Schaeffer III, Mol. PHys. 21,317 (1971).

11. Richard J. Blint and Marshall D. Newton, J. Chem. Phys. 59,6220 (1973).

12. David M. Hirst, Mol. Phys. 31,1511 (1976).

13. R. P. Messmer and D. R. Salahub, J. Chem. Phys. 65,779 (1976).

14. D. Grimbert and A. Devaquet, Mol. Phys. 27,831 (1974).

15. Sigrid D. Peyerimhoff and Robert J. Buenker, J. Chem. Phys., 47, 1953 (1967).

16. Michael J. S. Dewer, Santiago Olivella and Henry S. Rzepa, Chem. Phys. Lett. 47,80(1977).

17. Edward C. Y. Inn and Yoshio Tanaka, J. Opt. Soc. Amer. 43,870 (1953).

18. Edward C. Y. Inn and Yoshio Tanaka, Advances in Chemistry Series.

19. Jean-Claude Depannemaecker and Jean Bellet, J. Mol. Spectros. 66, 106 (1977).

20. Christopher C. Jones and John H. Shaw, J. Mol. Spectros. 68, 48 (1977).

21. M. Lichtenstein, J. J. Gallagher, and S. A. Clough, J. Mol. Spectros. 40,10 (1971)

22. A. G. Hearn, Proc. Phys. Soc., 78,932 (1961).

23. M. Griggs, J. Chem. Phys. 49,857 (1968).

24. Takehiko Tanaka and Yonezo Morino, J. Mol. Spectors. 33,538 (1977).

25. R.G.W. Norrish, and R. P. Wayne, Proc. Roy.Soc. Lond. A 288,200 (1965).

26. I.T.N. Jones and R. P. Wayne, Proc. Roy. Soc. Lond. A319, 273 (1970).

27. I.T.N. Jones, U. B. Kaczmar and R. P. Wayne, Proc. Roy. Soc. Lond. A 316,431 (1970).

28. M. Gauthier and D. R. Snelling, J. Chem. Phys. 54,4317 (1971).

29. John W. Simons, Richard J. Paur, Henry A. Webster III, and Edward J. Bair, J. Chem. Phys. 59,1203 (1973).

30. K. H. Welge, Can. J. Chem. 52,1424 (1974).

31. R. J. Cvetanovic, Can. J. Chem. 52,1452 (1974).

32. E. Castellano and H. J. Schumacher, Zeit, Phys. Chem. 65,62 (1969).

33. R. Simonaitis, S. Braslavsky, Julian Heicklen, and M. Nicolet, Chem. Phys. Lett., 19,601 (1973).

34. I. Arnold, F. J. Comes, and G. K. Moortgat, Chem. Phys. 24, 211 (1977).

35. Susan Kuis, R. Simonaitis, and Julian Heicklen, J. Geophys. Res. 80, 1328 (1975).

36. G. K. Moortgat and P. Warneck, Z. Naturforsch., 30A, 835 (1975).

37. D. L. Philen, R. T. Watson, and D. D. Davis, J. Chem. Phys. 67,3316 (1977).

38. O. Kajimoto and R. J. Cvetanovic, Chem. Phys. Lett. 37,533 (1976).

39. Geert Karel Moortgat and Eberhard Kudszus, Geophys. Res. Lett. 5, 191 (1970).

40. C. E. Fairchild, E. J. Stone, and G. M. Lawrence, J. Chem. Phys. 69,3632 (1978).

41. H. I. Schiff Ann. Geophys. 28,67(1972).

42. W. B. DeMore and O. F. Raper, J. Chem. Phys. 37,2048 (1962).

43. W. B. DeMore and O. F. Raper, J. Chem. Phys. 44, 1780 (1966).

44. W. D. McGrath and R. G.W. Norrish, Nature, 182, 235 (1958).

45. E. Lissi and J. Weicklen, J. Photochem. 1,39 (1972)

46. H. Webster III and E. J. Bair J. Chem. Phys. 53, 4532 (1970).

47. D. J. Giarchardi and R. P. Wayne, Chem. Soc. Faraday Disc. 53, 172 (1972).

48. J. Davenport, B. Ridley, H. I. Schiff, and K.H.Welge, Chem. Soc. Faraday Disc. 53,230 (1972).

49. C. L. Lin and W. B. Demore, I.A.G.A. Symposium, Kyoto, 1973.

50. Paul W. Fairchild and Edward K.C. Lee, Chem. Phys. Lett. 60,36 (1978).

51. S.T. Amimoto, A.P. Force, J. R. Wiesenfeld, Chem. Phys. Lett. 60, 40 (1978).

52. D. Martin J. Girman, and H. S. Johnston, 167th American Chemical Society National Meeting, Los Angeles, Spring 1974.

53. A. R. Wulf and E. H. Melvin, Phys. Rev. 38, 330 (1931).

54. A. Jakowlewa and K. Kondratjew, Phys. Z. Sawjetunion 9,106 (1936).

55. W. H. Eberhardt and W. Shand, Jr., J. Chem. Phys. 14,525 (1946).

56. Gilbert Newton Lewis, and Merle Randtell rev. Kenneth S. Pitzer and Leo Brewe, Thermodynamics second ed. (McGraw-Hill, New York, 1961), P.680.

57. T. T. Warnock and R. B. Bernstein, J. Chem. Phys. 49,1878 (1968).

58. Gary L. Catchen, Javed Husain, and Richarn N. Zare, J. Chem. Phys. 69, 1737 (1978).

59. M. P. Ekstrom, IEEE. Trans on Aud. and Electroacst, AV-21, 344 (1973).

60. A.E.W. Knight and B. K. Sclinger, Spectrochimica Acta 27A,1223 (1971).

61. D. L. Phillips, J. Ass. Comput. Mach., Vol. 9, 97 (1962).

62. B. R. Hunt, IEEE Trans Audio Electroacoust. AV-20, 94 (1972).

63. B. R. Hunt, Math. Biosci. 8,161 (1970).

64. A. L. Khidir and J. C. Decius, Spectrochim. Acta 18, 1629 (1962).

65. Hertzberg,Gerhard. Molecular Spectra and Molecular Structure - Spectra of Diotomic Molecules Vol. I (New York, Van Nostrand 1950).

66. George E. Busch and Kent R. Wilson, J. Chem. Phys. 56,3626 (1972).

67. K. E. Holdy, L. C. Klotz, and K. R. Wilson, J. Chem. Phys. 52,4588 (1970).

68. J. P. Simons and P. W. Tasker, Mol. Phys. 26, 1267 (1973).

69. C. E. Caplan and M. S. Child, Mol. Phys. 23,249 (1972).

70. Shaul Mukamel and Joshua Jortner, J. Chem. Phys. 60,4760 (1974).

71. R. G. Gilbert and I. G. Ross. Anst. J. Chem. 24,145 (1971).

72. M. Shapiro and R. D. Levine, Chem. Phys. Lett. 5,499 (1970).

73. M. J. Berry, Chem. Phys. Lett. 29,329 (1974).

74. G. A. West and M. J. Berry, J. Chem. Phys. 61,4700 (1974).

75. M. J. Berry, J. Chem. Phys. 61,3114 (1974).

76. Yelunda B. Band and Karl F. Freed, J. Chem. Phys. 63,3382 (1975).

77. Yehuda B. Band and Karl F. Freed, J. Chem. Phys. 67,1462 (1977).

78. Yehuda B. Band, Michael D. Morse, and Karl F. Freed, J. Chem. Phys. 68,2702 (1978).

79. O. Atabek and R. Lefebure, Chem. Phys. Lett. 52, 29 (1977).

80. J. A. Beswick and Joshua Jortner, Chem. Phys. 24, 1 (1977).

81. O. Atabek, J. A. Beswick, R. Lefebure, S. Mukamel, and J. Jortner, J. Chem. Phys. 65, 4035 (1976).

82. M. S. Child, Mol. Phys. 29,1421 (1975).

83. M. S. Child, Can. J. Phys. 53, 1838 (1975).

84. W. H. Miller, J. Chem. Phys. 48,464 (1968).

85. Eric J. Heller, J. Chem. Phys. 68, 2066 (1978).

86. Eric J. Heller, J. Chem. Phys. 68, 3891 (1978).

87. J. G. Winan and E. C. G. Stueckelberg, Proc. Nat'l. Acad. Sci U.S.A. 14, 867 (1928).

88. G. E. Gibson, O. K. Rice, and N. S. Bayliss, Phys. Rev. 44, 193 (1933).

89. H. M. James, A. S. Coolidge, and R. D. Present, J. Chem. Phys. 4, 187 (1936).

90. D. Porret and C. F. Goodeve, Trans. Faraday Soc. 33, 690 (1937).

91. A. A. Gordus and R. B. Bernstein, J. Chem. Phys. 22, 790 (1954).

92. W. H. Miller, J. Chem. Phys. 61, 1823 (1974).

93. S. Goursaud, M. Sizun, and F. Fiquet-Fayard, J. Chem. Phys. 65,5453 (1976).

94. Russell T. Pack, J. Chem. Phys. 65, 4765 (1976).

Table 1 - Quantum Yields of O('D) from the Photolysis of Ozone

Wavelength	Quantum Yield	Reference	Comments
313.0 nm	0.75	(32)	T = 248°K
	1.00	(32)	T = 298°K
	0.53	(38)	T = 313°K
	0.21	(38)	T = 198°K
	0.35	(33)	T = 298°K
	0.32	(52)	T = 298°K
	0.29	(36)	T = 298°K
	0.29	(35)	T = 293°K
	0.22	(35)	T = 258°K
	0.11	(35)	T = 221°K
	0.10	(26)	T = 298°K
	0.08	(49)	T = 235°K
	0.120 ± 0.029	(37)	T = 298°K
	0.193 ± 0.008	(34)	T = 298°K
312.0	0.242 ± 0.051	(34)	Normalized to 1 at 305 nm.
	0.154 ± 0.024	(37)	Normalized to 1 at 300 nm.
311.0	0.406 ± 0.055	(34)	
	0.224 ± 0.032	(37)	
310.0	0.344 ± 0.068	(37)	
	0.567 ± 0.035	(34)	
305.0	1.016 ± 0.005	(34)	
	0.871 ± 0.086	(37)	
300.0	0.966 ± 0.078	(34)	
	1.004 ± 0.065	(37)	
	0.580 ± 0.160	(50)	Normalized to average quantum yield
295.0	1.054 ± 0.095	(34)	
295.0	1.050 ± 0.090	(37)	
295.0	0.870 ± 0.070	(50)	
290.0	0.880 ± 0.030	(50)	
285.0	1.020 ± 0.090		
280.0	1.000 ± 0.070		
275.0	0.970 ± 0.020		
270.0	1.080 ± 0.120		
266.0	1.060 ± 0.050		Exceeds unity within error limits
260.0	1.050 ± 0.100		
255.0	0.950 ± 0.060		
250.0	1.060 ± 0.150		

Table 2 - Threshold Energies for O_3 Dissociation

Bond Energy = 23.9 Kcal./Mole (8359 cm^{-1})

	Oxygen Atom		Oxygen Molecule		Energy Threshold	
	State	Energy	State	Energy	cm^{-1}	Kcal.
	$O(^3P_2)$	0.0	$O_2(X^3\sum_g-)$	0.0	8359	23.9
	$O(^3P_1)$	158.5	$O_2(X^3\sum_g-)$	0.0	8517	24.4
	$O(^3P_o$	226.5	$O_2(X^3\sum_g-)$	0.0	8585	24.5
*	$O(^3P_2)$	0.0	$O_2(a^1\Delta_g)$	7882.4	16241	46.4
*	$O(^3P_1)$	158.5	$O_2(a^1\Delta_g)$	7882.4	16400	46.9
*	$O(^3P_o)$	226.5	$O_2(a^1\Delta_g)$	7882.4	16468	47.1
*	$O(^3P_2)$	0.0	$O_2(b^1\sum_g+)$	13120.9	21480	61.4
*	$O(^3P_1)$	158.5	$O_2(b^1\sum_g+)$	13120.9	21638	61.9
*	$O(^3P_o)$	226.5	$O_2(b^1\sum_g+)$	13120.9	21706	62.1
*	$O(^1D_2)$	15867.7	$O_2(X^3\sum_g-)$	0.0	24226	69.3
	$O(^1D_2$	15867.7	$O_2(a^1\Delta_g)$	7882.4	32109	91.8
	$O(^1D_2)$	15867.7	$O_2(b^1\sum_g+)$	13120.9	37348	106.8
*	$O(^1S_o)$	33792.4	$O_2(X^3\sum_g-)$	0.0	42151	120.5
	$O(^1S_o)$	33792.4	$O_2(a^1\Delta_g)$	7882.4	50034	143.1
	$O(^1S_o)$	33792.4	$O_2(b^1\sum_g+)$	13120.9	55272	158.0

*Spin forbidden processes.

Table 3 - Excess Kinetic Energy of Vigrational States

$O\ (^1D_2) + O_2\ (a^1\Delta_g)$

Vibr. Q.N.	$(E_{V_i} - E_{V_o})$	Threshold	Excess Energy (107.5-Threshold)
0	0.00	91.81	15.69
1	4.24	96.05	11.45
2	8.42	100.23	7.27
3	12.52	104.33	3.17
4	16.56	108.37	Not accessible

$O\ (^1D_2) + O_2(b^1\Sigma_{g^+})$

0	0.00	106.78	0.71
1	4.01	110.79	Not accessible

Table 4 - Operating Parameters for Ozone Photofragment Experiment

Ozone partial pressure	~10 torr
Argon partial pressure	~580 torr
Nozzle diameter	.003 inches
Nozzle to skimmer distance	.24 inches
Expansion region pressure	2×10^{-4} torr
Differential pumping region pressure	5×10^{-5} torr
Main chamber pressure	2×10^{-7} torr
First region - detector pressure	1×10^{-8} torr
Second region detector pressure	$<10^{-9}$ torr
Ionizing region pressure	$<10^{-9}$ torr
Ionizing emission current	10 ma.
Ion energy	+80 volts
Extractor voltage	-580 volts
Quadrupole exit lens #1	-3660 volts
Quadrupole exit lens #2	-750 volts
Ion target	+27 K.V.
Phototube cathode	-1800 V

Table 5 - Modified Impulsive Model

Translational Energy of O_2 Fragment Calculated for Certain Bond Angles. Recoil is assumed to be along the fragmenting axis.

$$E_R = \sin^2 \chi \left[\left(1 - \frac{\mu_a}{\mu_f}\right)^{-1} - \cos^2 \chi \right]^{-1} E_{AVL}$$

$$E_T = E_{AVL} - E_R$$

Translational Energy (Kcalories/mole)

χ (Deg)	V = 0 E_{AVL} = 15.74	V = 1 E_{AVL} = 11.50	V = 2 E_{AVL} = 7.32	V = 3 E_{AVL} = 3.22
128	13.04	9.53	6.06	2.67
126	12.92	9.44	6.01	2.64
124	12.81	9.36	5.96	2.62
122	12.70	9.28	5.90	2.60
120	12.59	9.20	5.86	2.58
118	12.49	9.13	5.81	2.56
116	12.40	9.06	5.77	2.54
114	12.31	9.00	5.73	2.52
112	12.23	8.94	5.69	2.50
110	12.16	8.88	5.66	2.49
108	12.09	8.84	5.62	2.47
106	12.03	8.79	5.60	2.46

FIGURE CAPTIONS

Fig. 1 Ultra violet absorption spectrum of ozone from Ref. 17. Absorption is given in (liter-moles)/cm using log base 10. The cross section for irradiation at 2660 is indicated.

Fig. 2 Energy levels for the possible asymptotic fragments of ozone. O_2 levels are taken from Ref. 65, and O levels from C. E. Moore NBS monograph 35 (U. S. Government Printing Office, Washington D. C. 1962).

Fig. 3 Schematic diagram of ozone source.

Fig. 4 Time of flight data for ozone source using a 92 cm. flight path and a scale dwell time of 5 x 10^{-6} sec per channel.

Fig. 5 Source dimensions used in ozone photodissociation experiments.

Fig. 6 Spatial profile of laser source in near and far field conditions. Experiment was performed at 1.5 meters from laser amplifier. From Laser Focus Magazine, July, 1978.

Fig. 7 Background signal produced when laser is focused so that focal point is coincident with vacuum chamber wall.

Fig. 8 Time of flight spectrum of the photodissociation of ozone using 10 torr ozone in 1000 torr argon for source expansion conditions. Van der Waals

complexes are evident. Scaler dwell time of 9 x 10^{-6} seconds. Mass 32 detected.

Fig. 9 Time of flight spectrum of the photodissociation of ozone with same conditions as Figure 8. Mass 48 detected.

Fig. 10 Time of flight spectrum of ozone using 10 torr ozone in 580 torr argon. Mass 32 detected, Scaler dwell time 3 x 10^{-6} seconds.

Fig. 11 Angular distribution of photofragment product with respect to E. The direction of recoil and the electric field vector in the center of mass reference frame define the polarization angle.

Fig. 12 Dependence of photofragment signal with laser power. Mass 32 detected for this study.

Fig. 13 Simulated time of flight spectrum for five monoenergetic photofragments. The output shows both the variation in intensity and peak width as a function of energy.

Fig. 14 Transformation of time of flight data (see Fig. 10) to center of mass energy coordinates. O represents a direct inversion process. ● gives the transformation obtained by the pr[illegible]e described in Appendix A.

Fig. 15 Quality of data fit using energy distribution shown in Figure 14.

Fig. 16 Plot of J vs. O atom exiting impact parameter. This graph illustrates the kinematic constraints placed on the photodissociative event.

Fig. 17 Transformation of raw time of flight data to center of mass energy coordinates using transformation described in Appendix A. ● 20°; O 30°; Δ 50° laboratory angles. Relative scaling between the 20°, 30°, and 50° data is performed using data from Figure 11.

Fig. 18 Background model generated and subtracted from time of flight data.

Fig. 19 Corrected time of flight data after artifact is subtracted.

Fig. 20 Transformation as described for Figure 17 after background artifact subtraction.

Fig. 21 Energy distribution of the vibrational levels of O_2 ($^1\Delta_g$) from the photodissociation of ozone at λ = 266 nm.

Fig. 22 Data fit using an average anistropy coefficient. Illustration shows the significant variation in b (E) among vibrational levels.

Fig. 23 Direct inversion of raw time of flight data (see Fig. 10). Ratio of ground state to excited state is obtained after correction for polarization dependence.

Fig. 24 Ground state potential surface for symmetric AB_2 molecule. Taken from Ref. 94.

Fig. 25 Excited state repulsive potential surface for AB_2 molecule as given in Ref. 94.

Fig. 26 Cut along symmetric coordinate of dissociation surface at the saddle point $Z = 0$.

Fig. 27 Cut along reaction coordinate centered at $Z = 0$ and $X = 0$.

Fig. 28 Transition probability as a function of energy for the potential shown in Fig. 27.

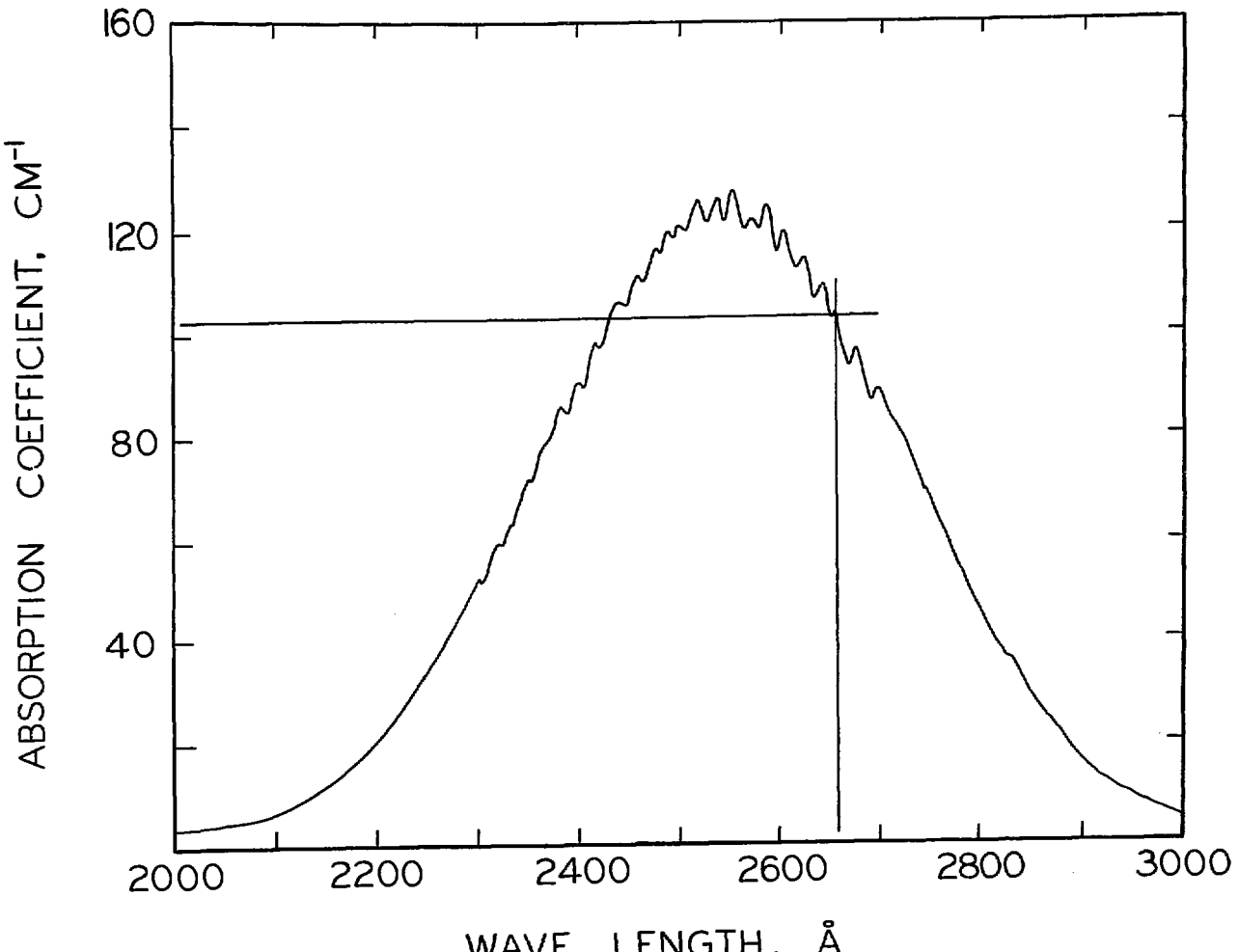

Figure 1

XBL 795-9742

Energy level diagram of $O + O_2$

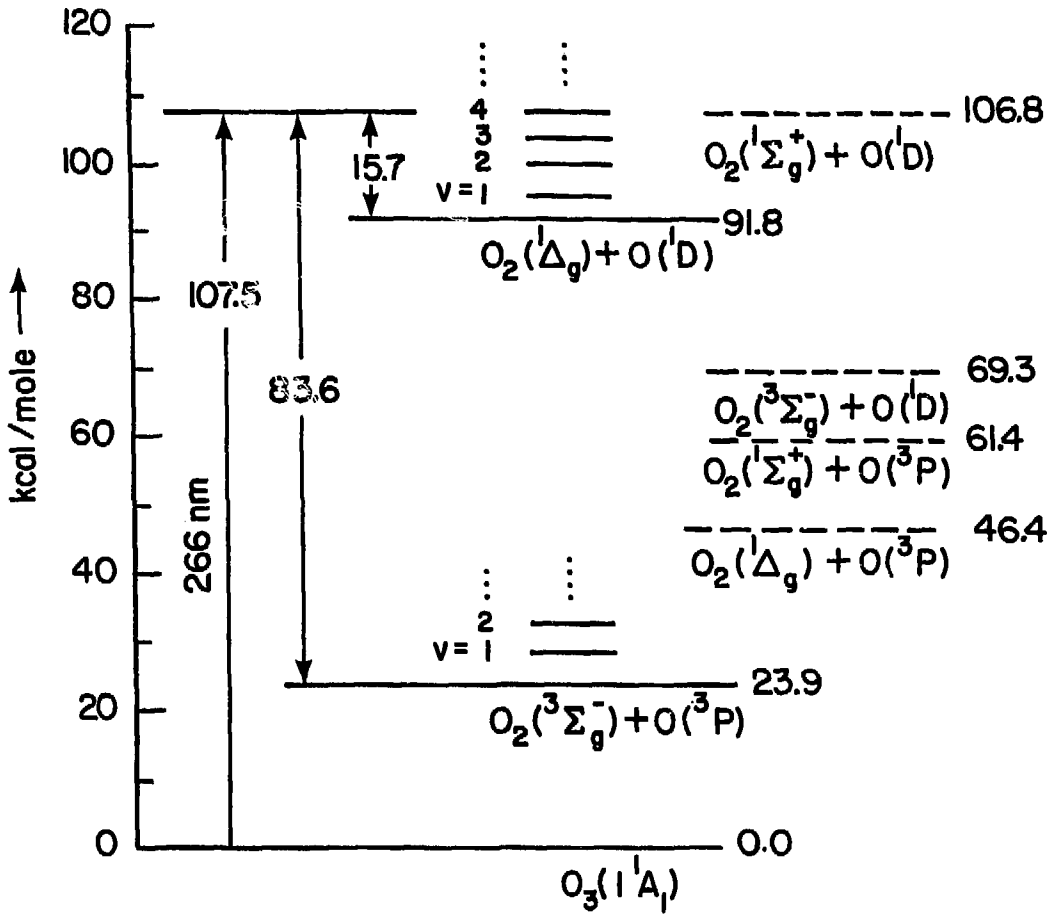

XBL 791-49

Figure 2

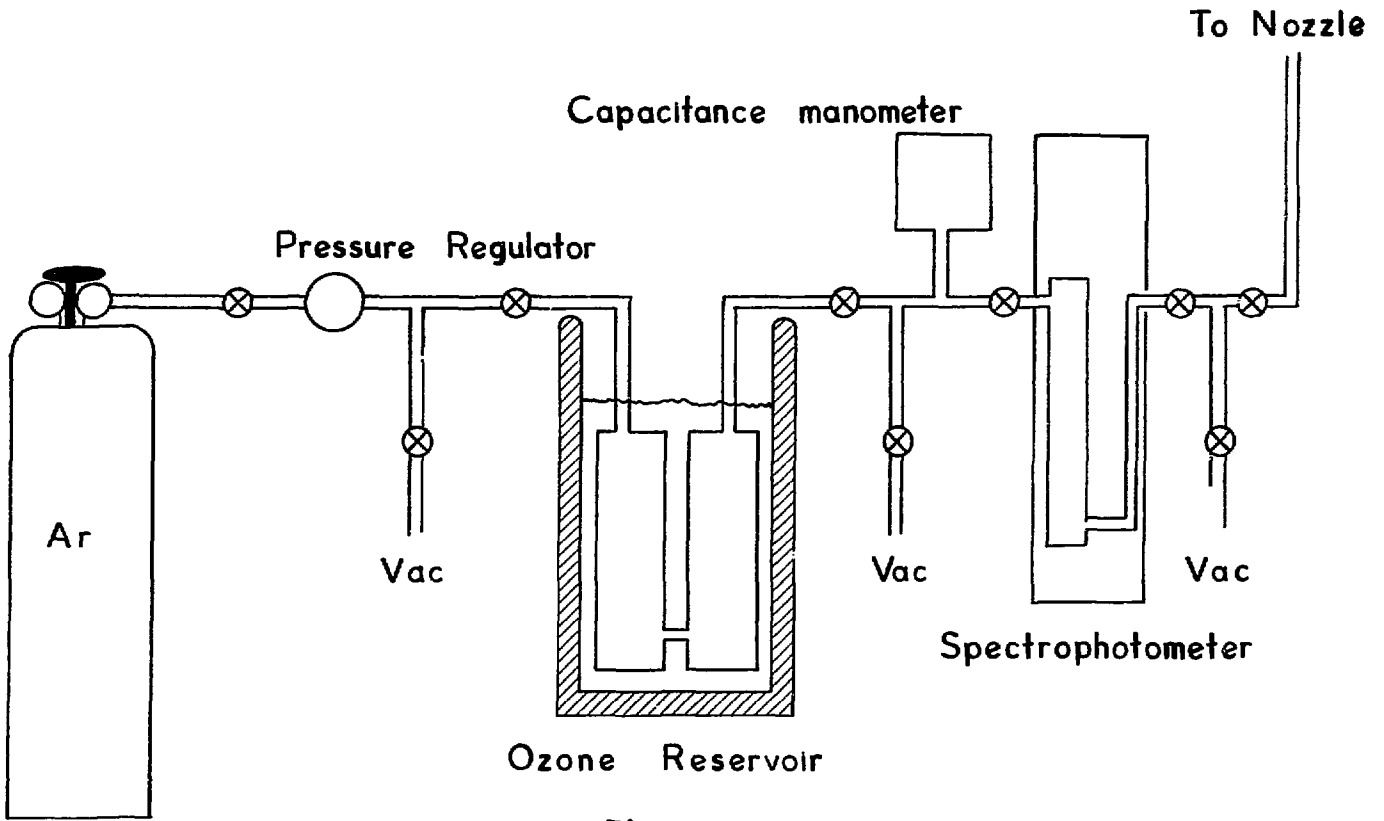

Figure 3

XBL 795-9739

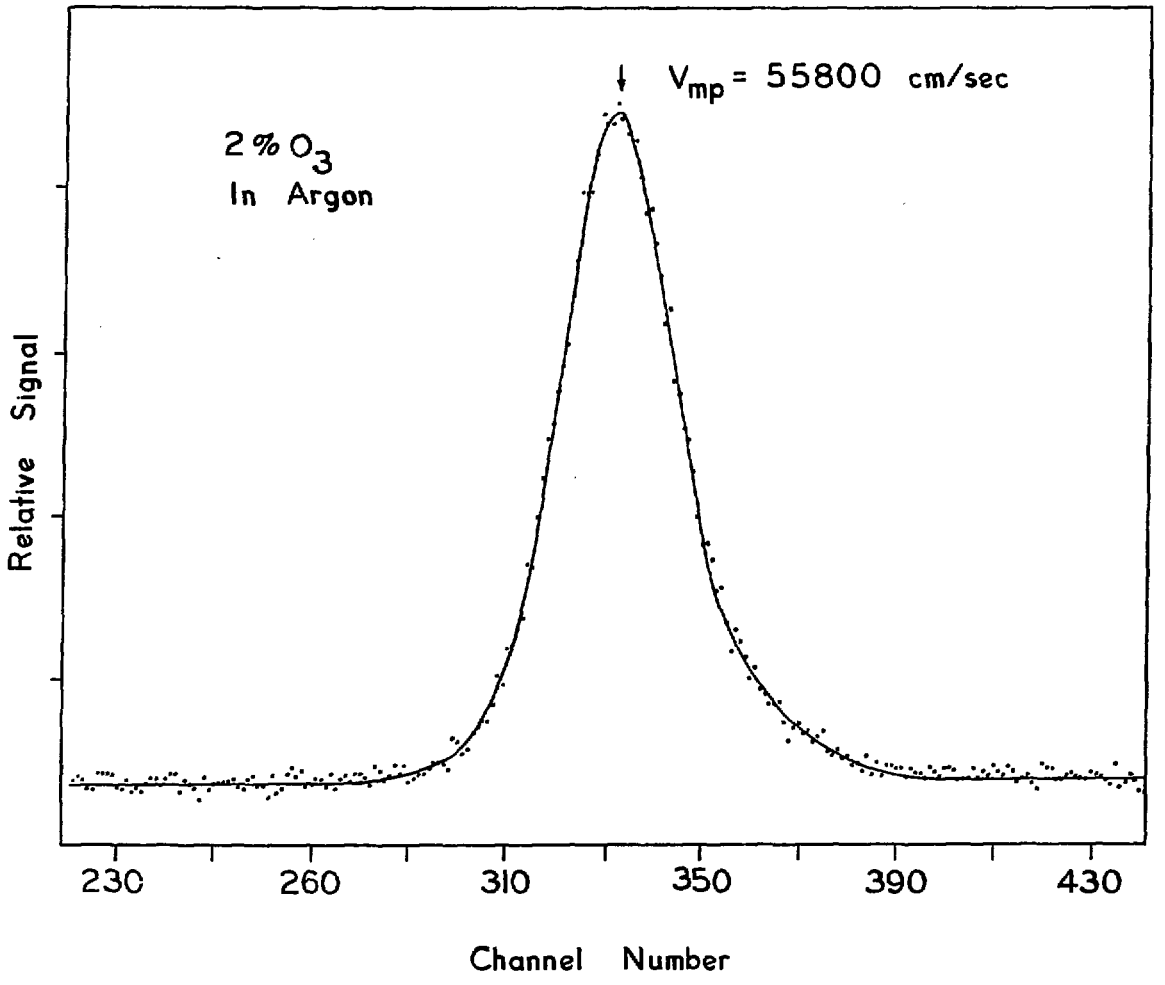

Figure 4

XBL 795-9746

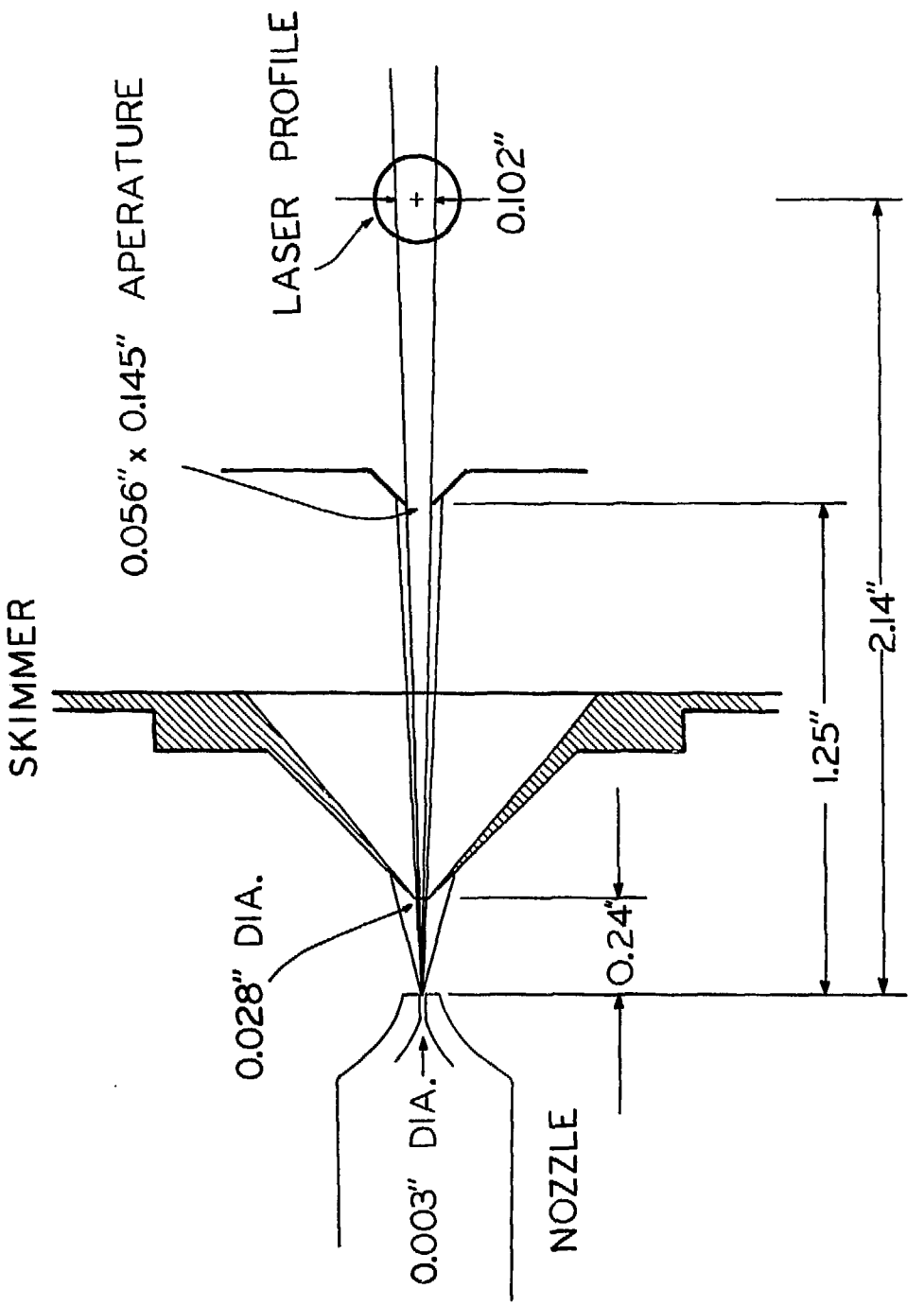
SKIMMER
0.056" x 0.145" APERATURE
LASER PROFILE
0.102"
0.028" DIA.
0.003" DIA.
NOZZLE
0.24"
1.25"
2.14"
XBL 795-9763

Figure 5

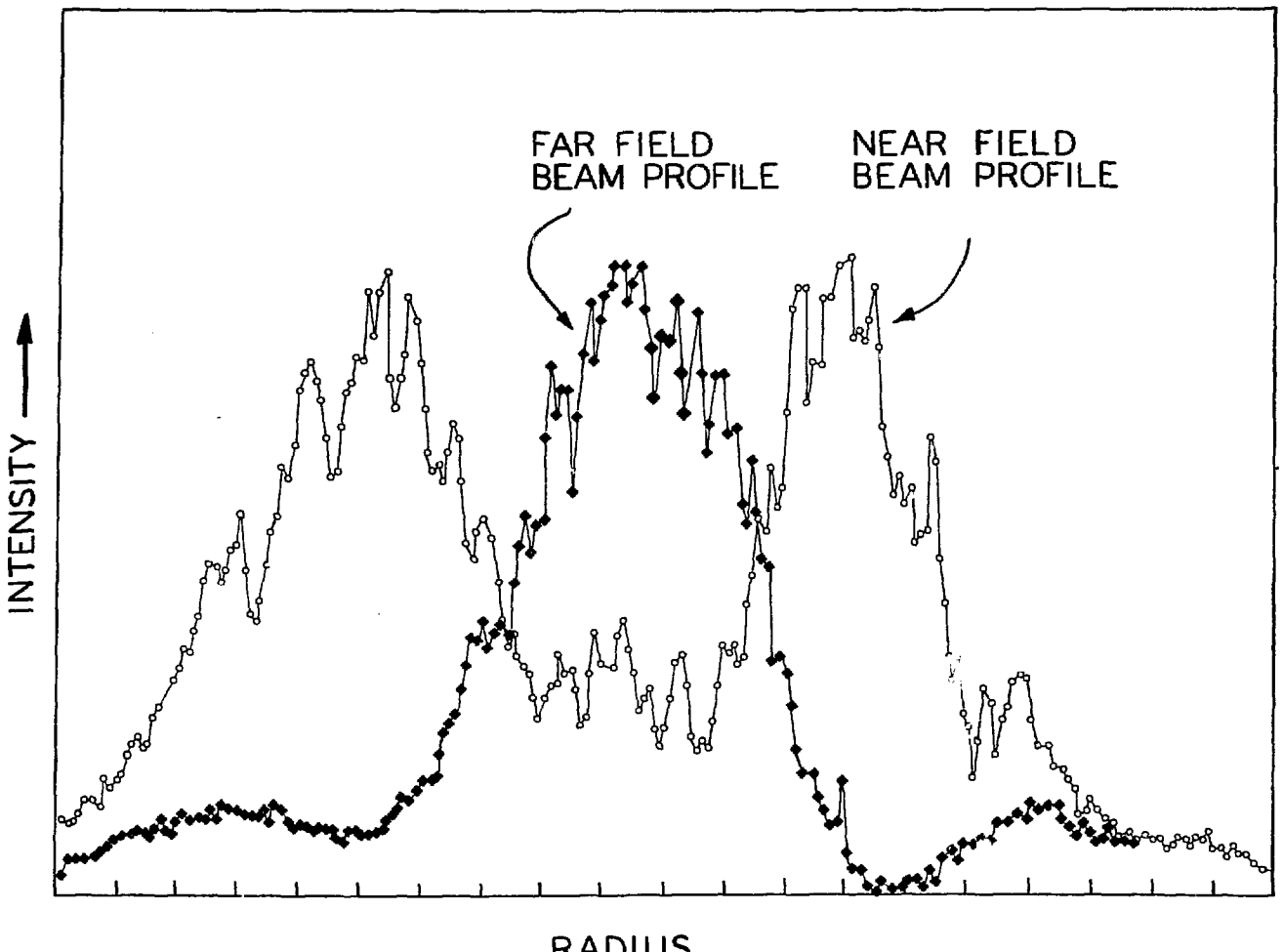

XBL 795-9762

Figure 6

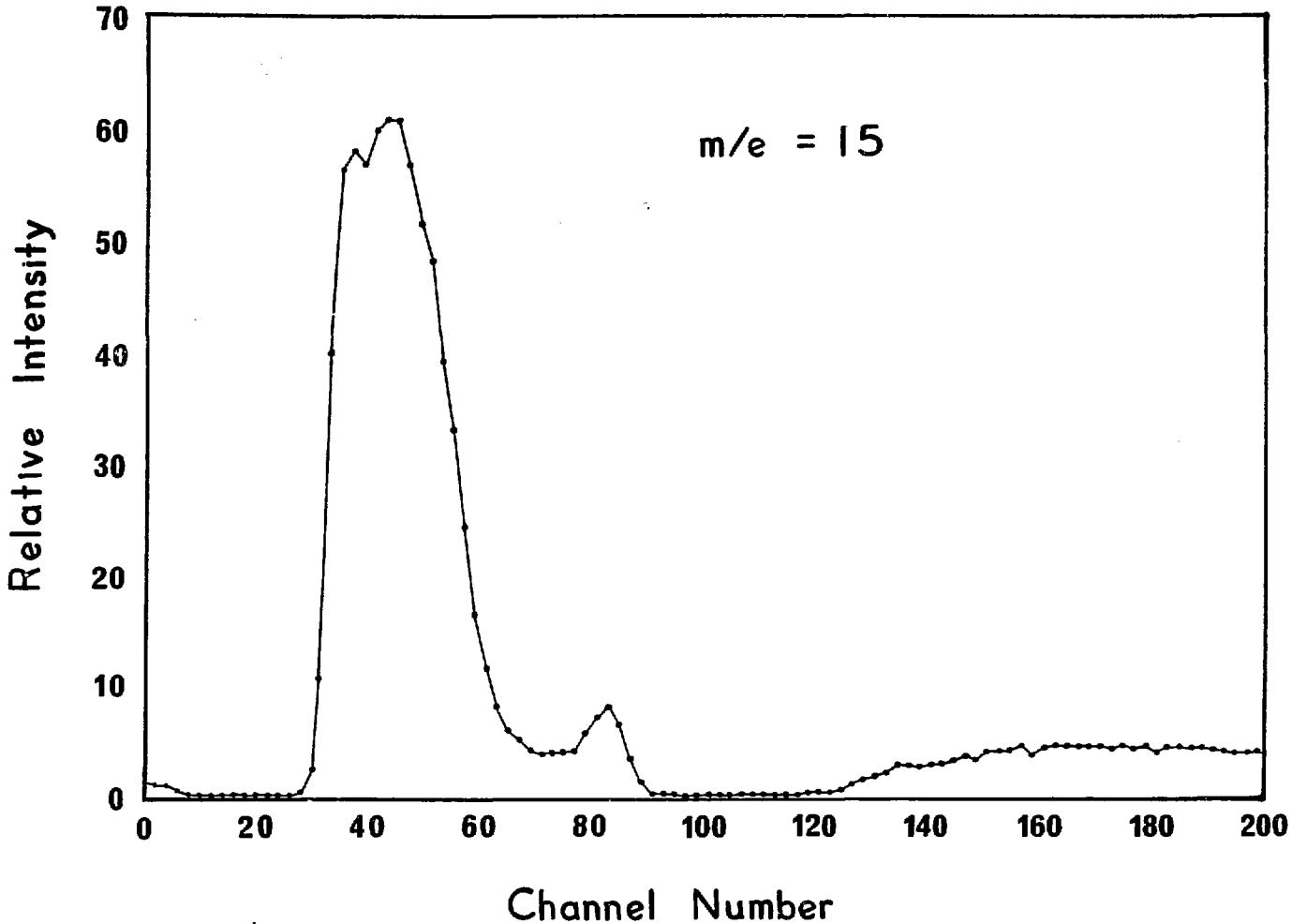

Figure 7

XBL 795-9738

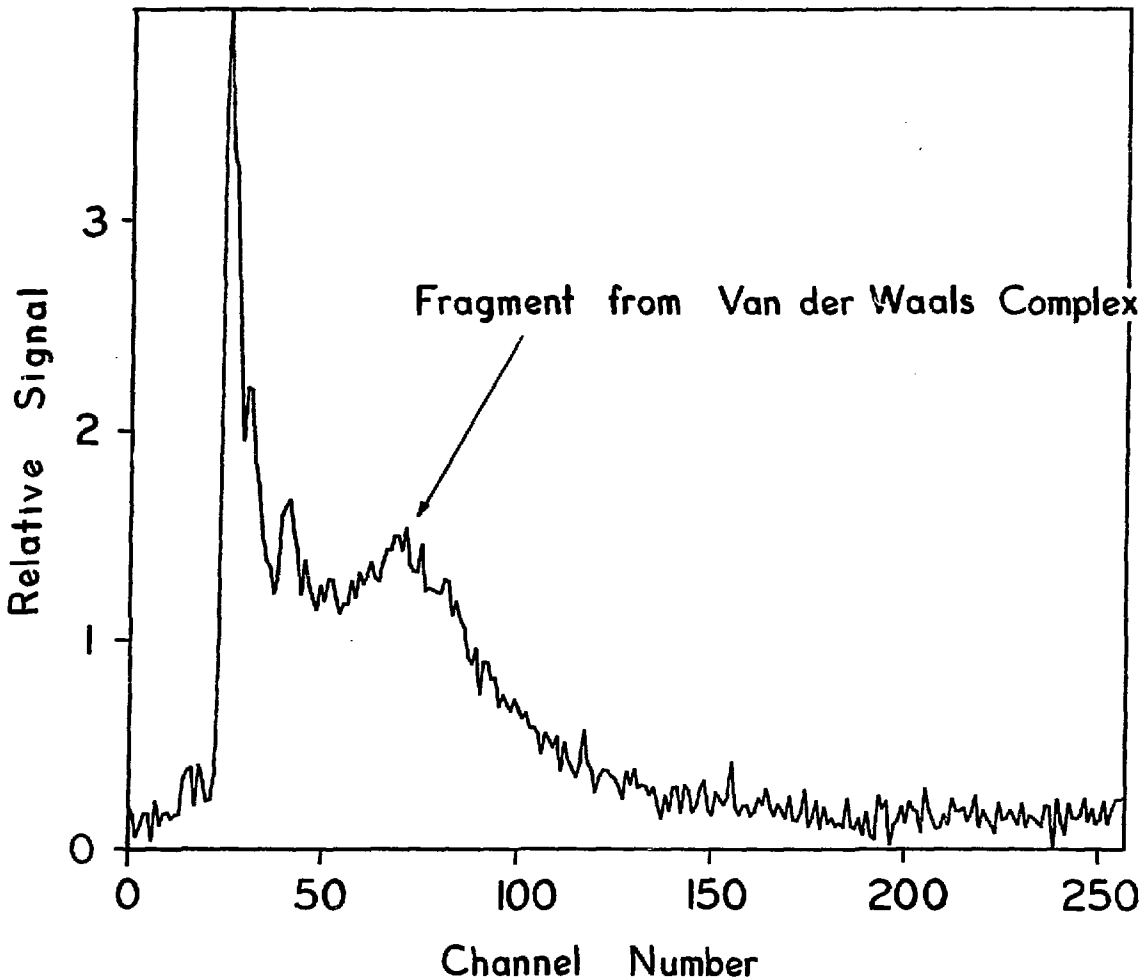

Figure 8

XBL 795-9747

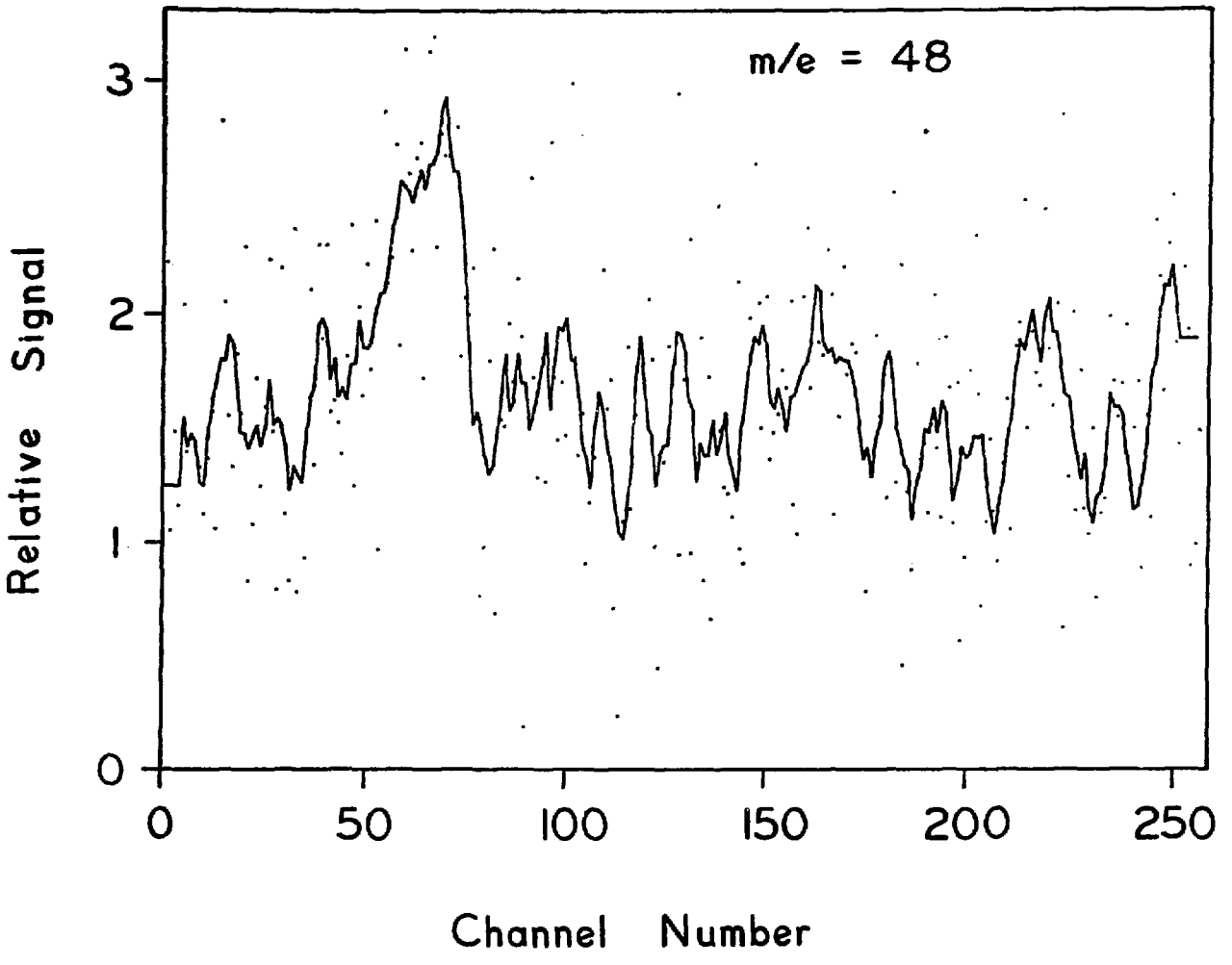

XBL 795-9750

Figure 9

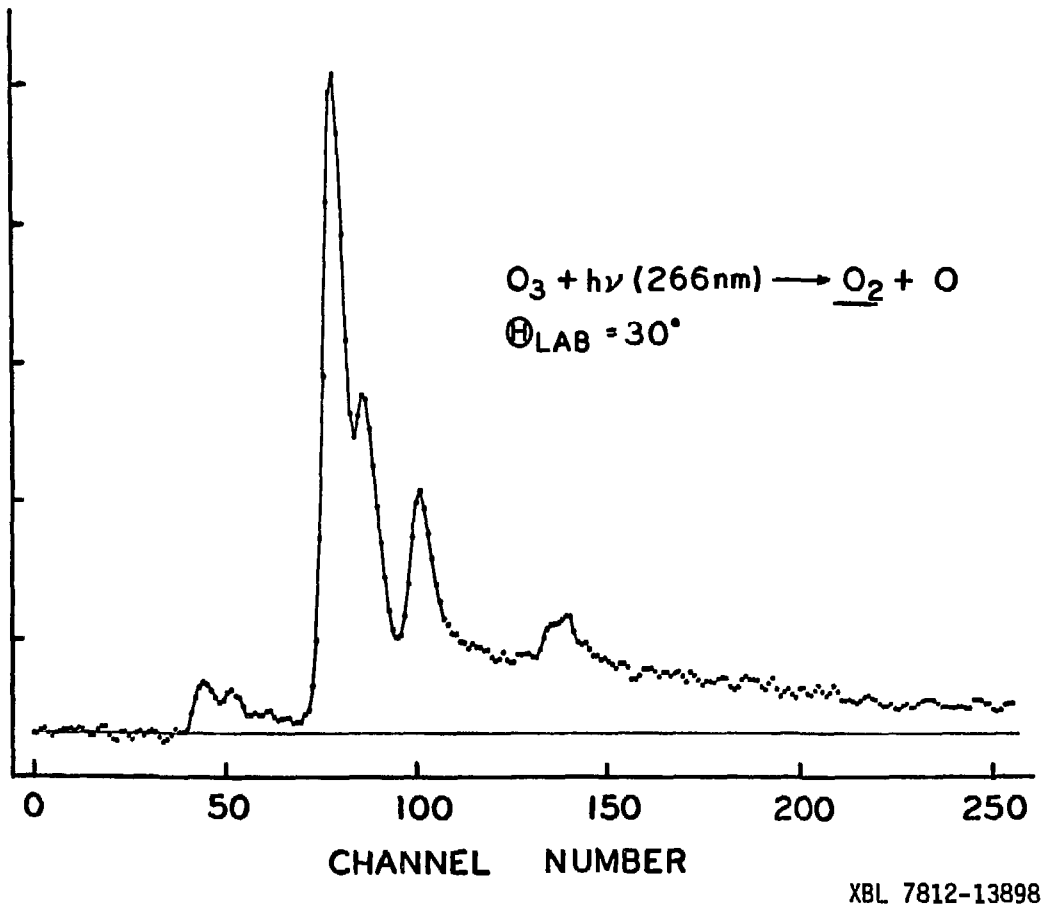
$O_3 + h\nu\,(266nm) \longrightarrow \underline{O_2} + O$
$\Theta_{LAB} = 30°$
0
50
100
150
200
250
CHANNEL NUMBER
XBL 7812-13898

Figure 10

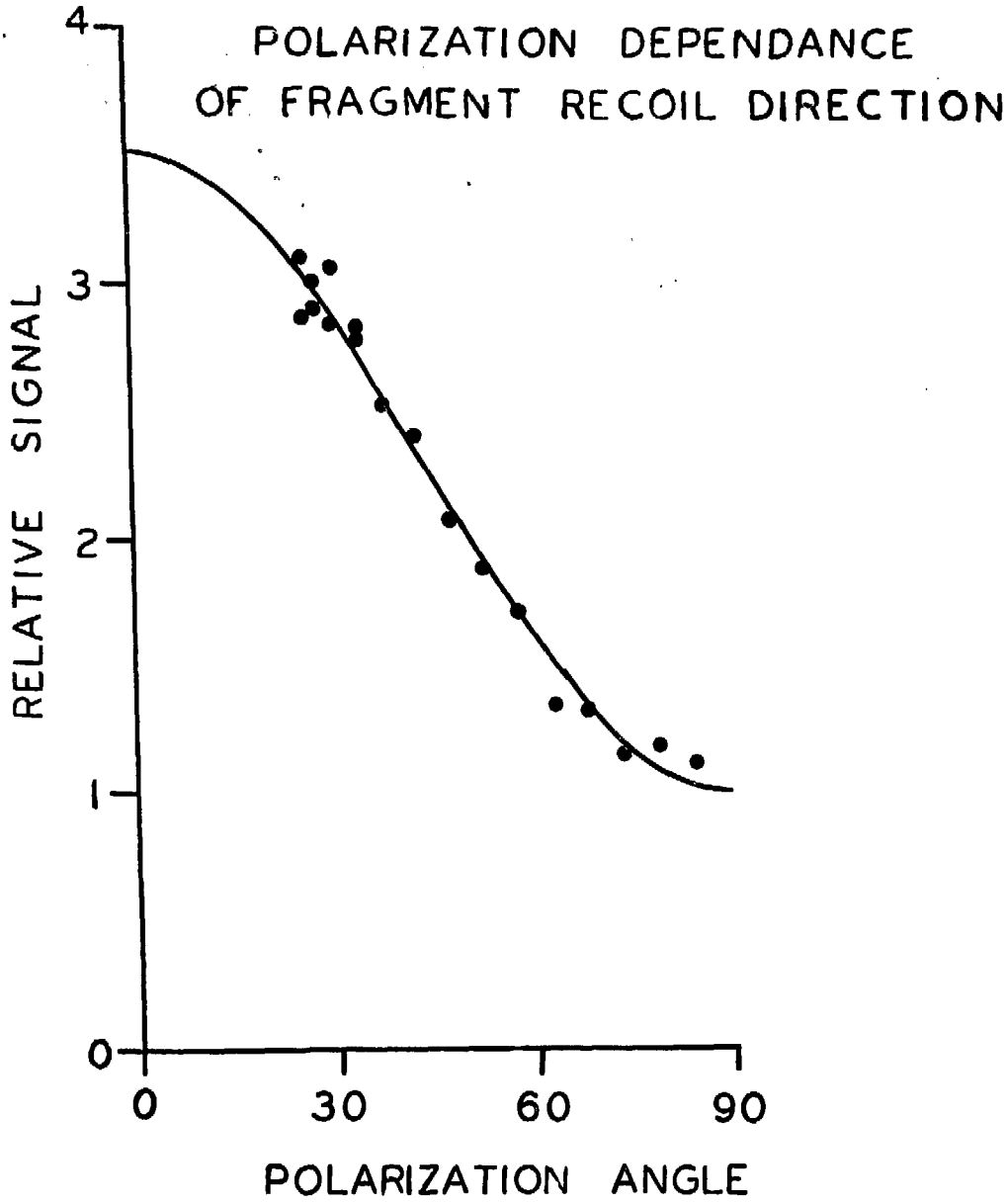

XBL 7812-13900

Figure 11

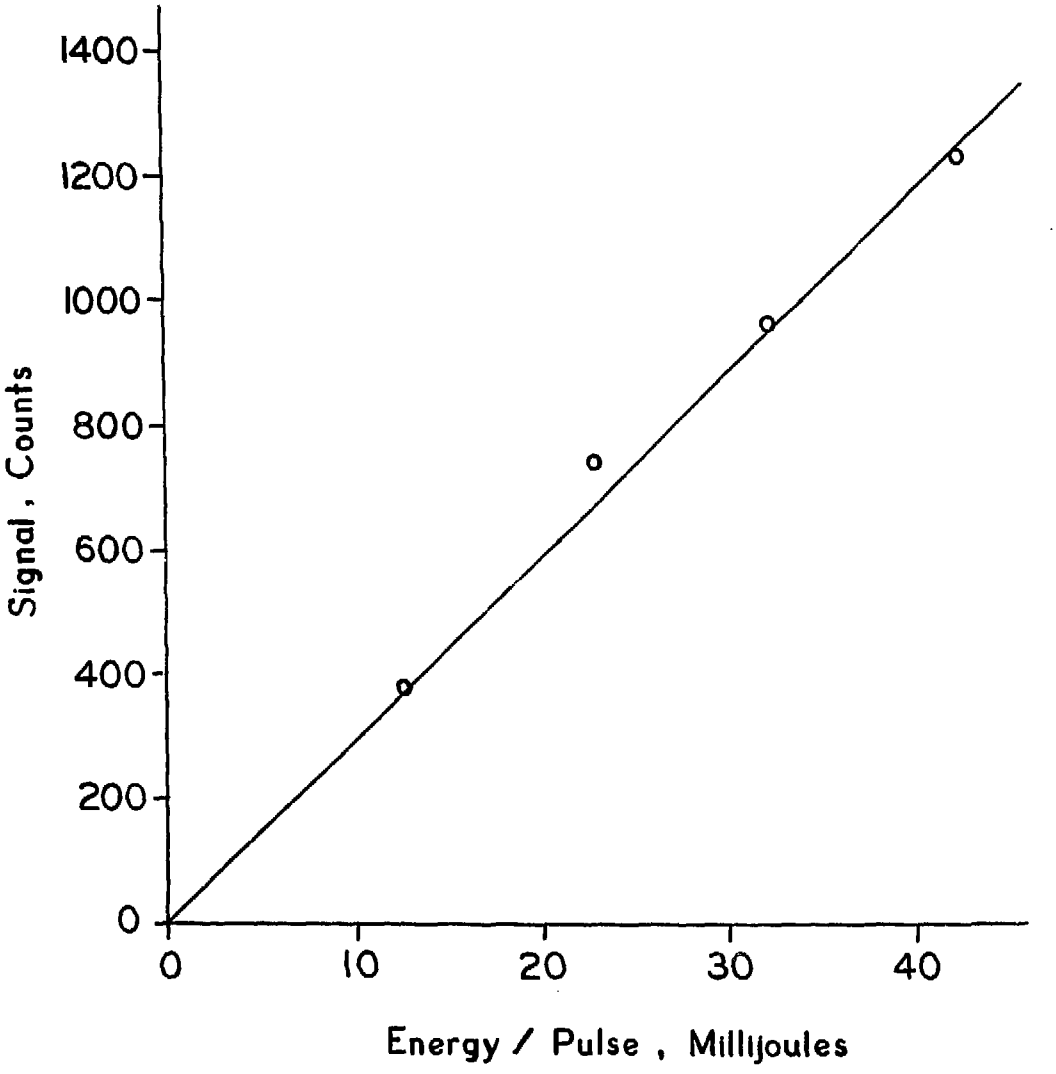

XBL 795-9748

Figure 12

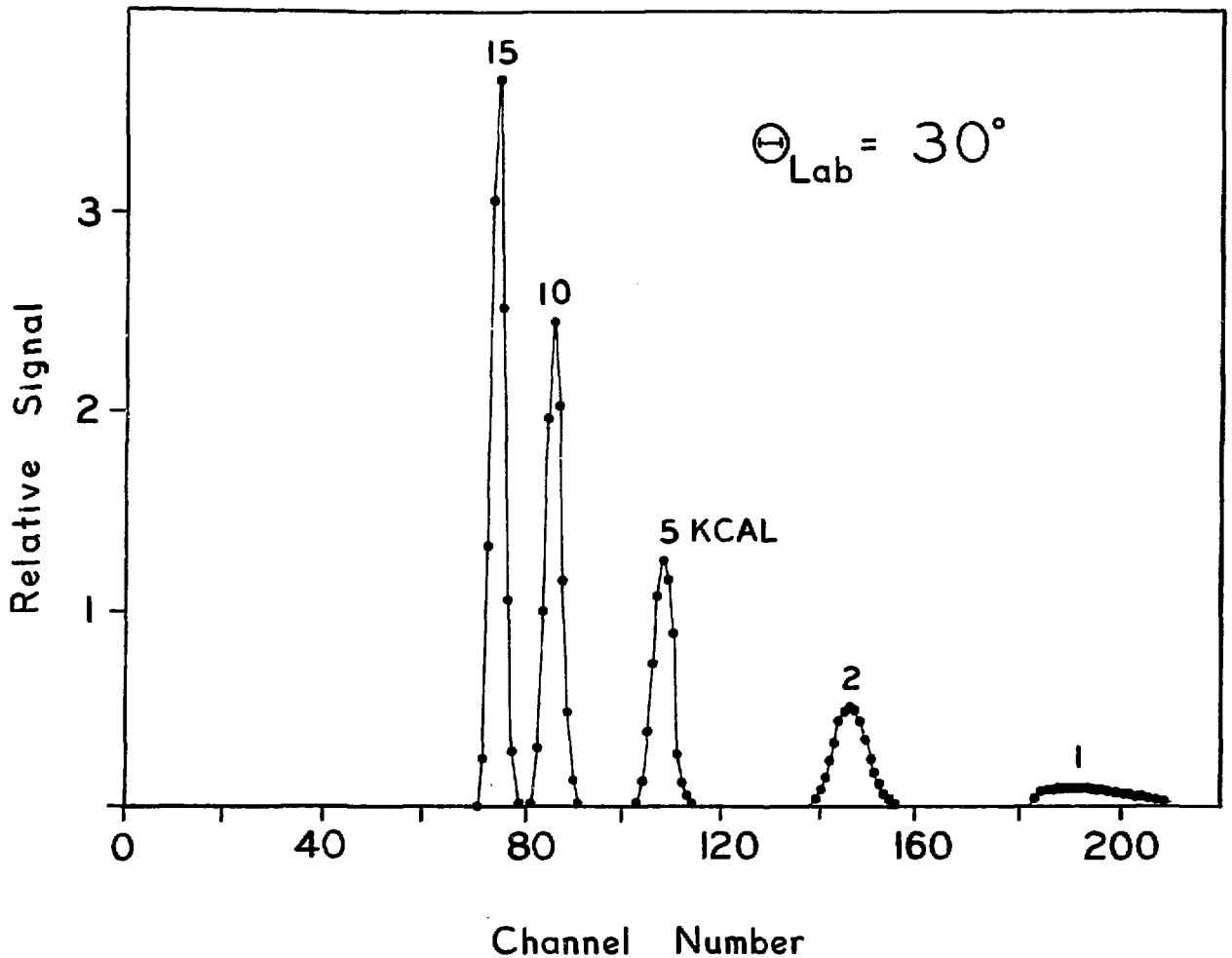

Figure 13

XBL 795-9749

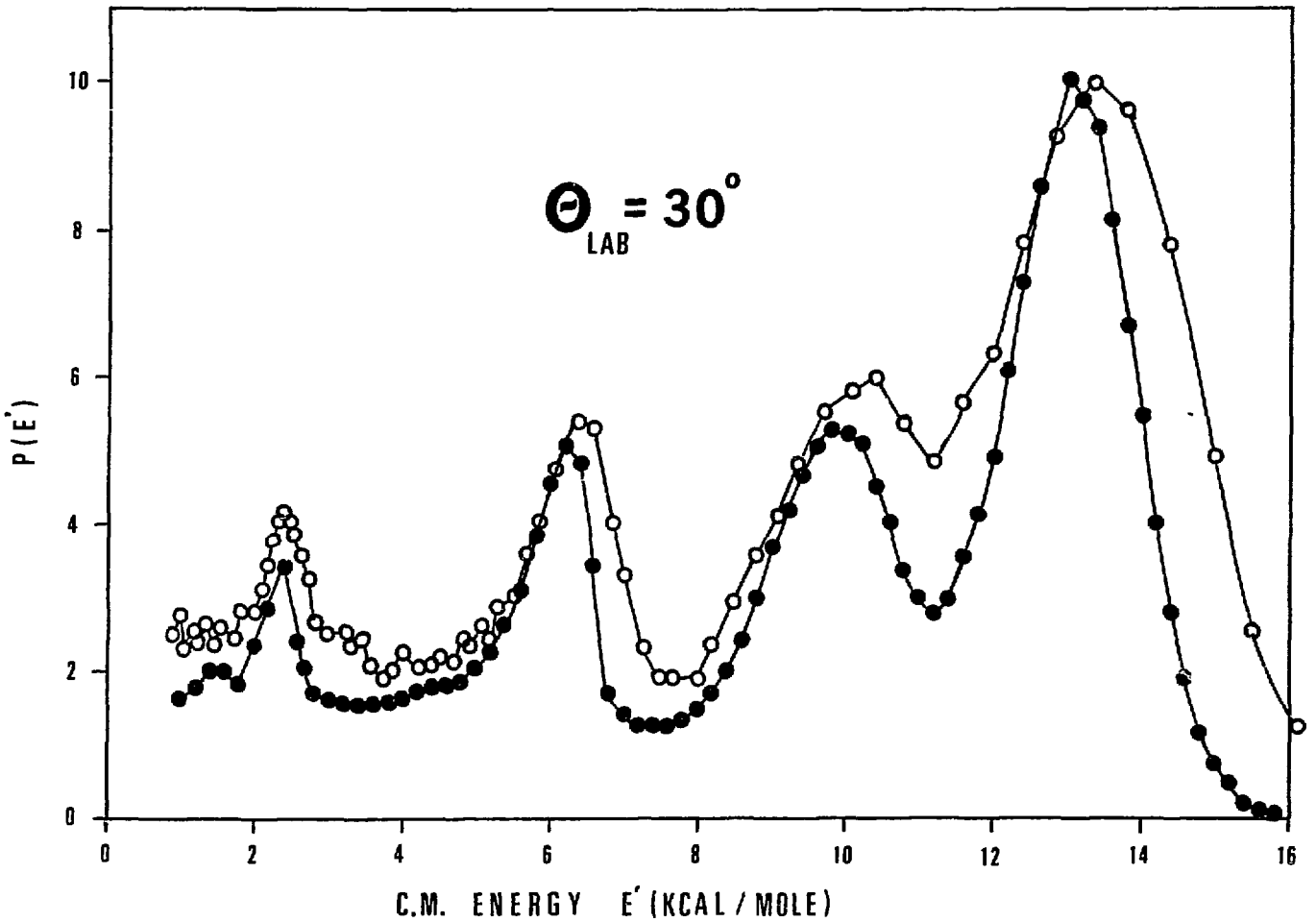

XBL 793-9042

Figure 14

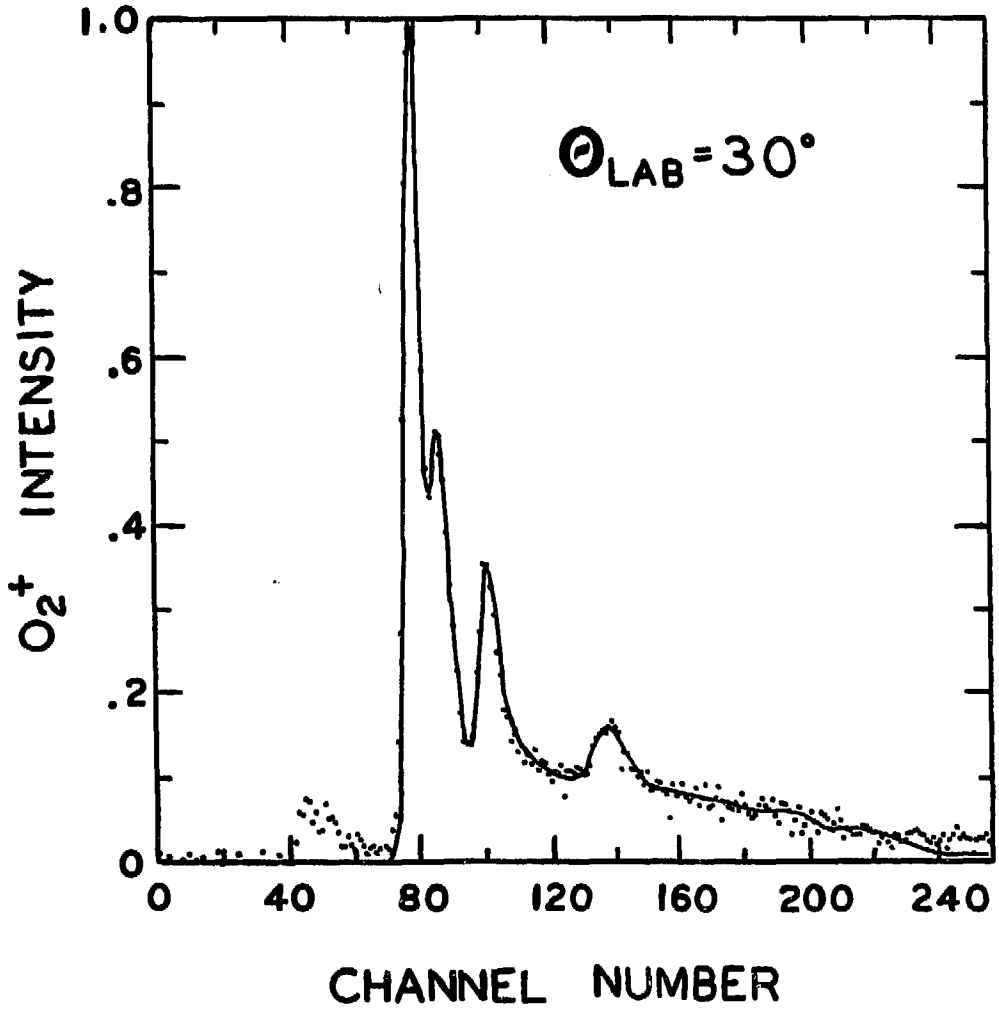

Figure 15

XBL 793-9043

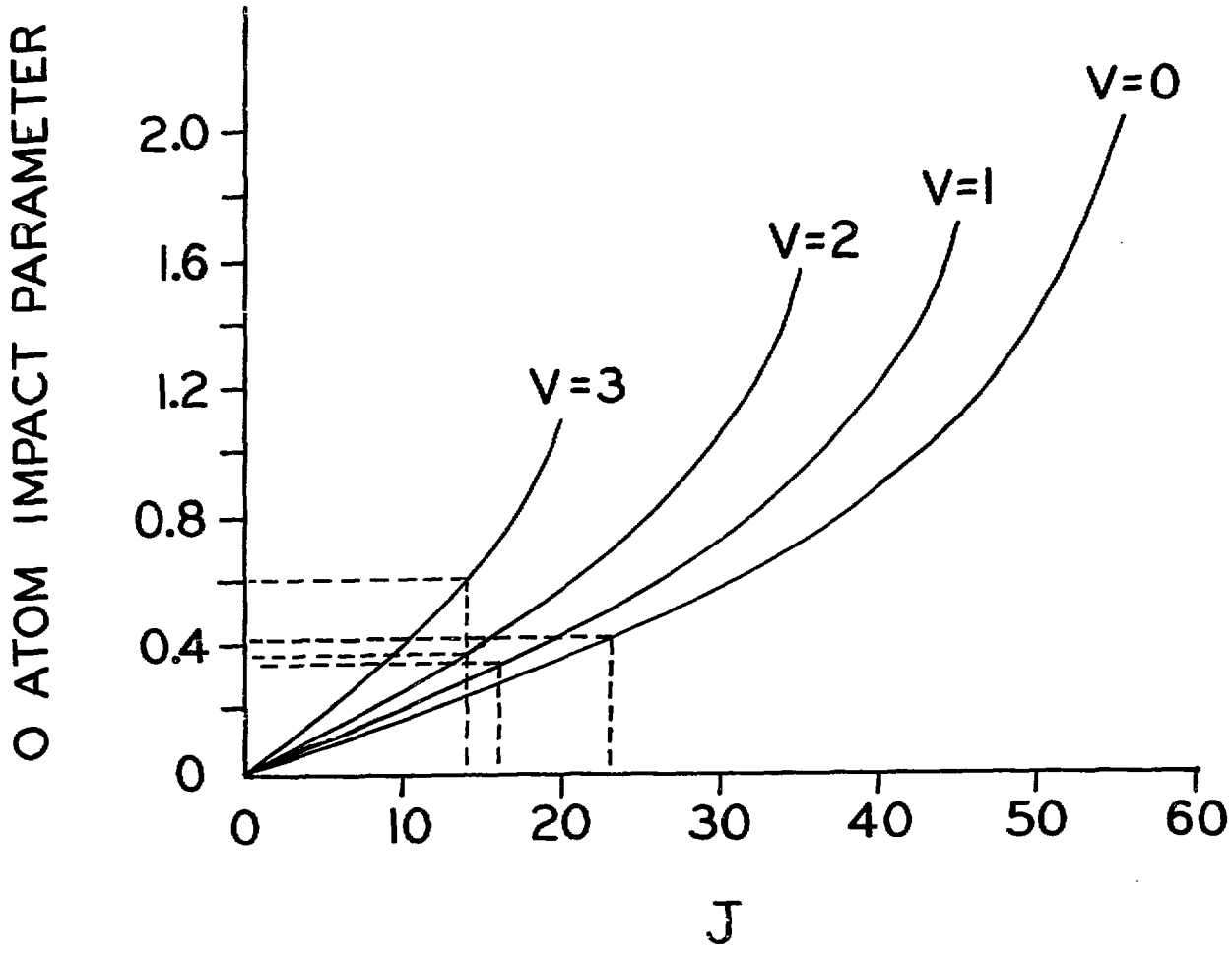

XBL 795-9751

Figure 16

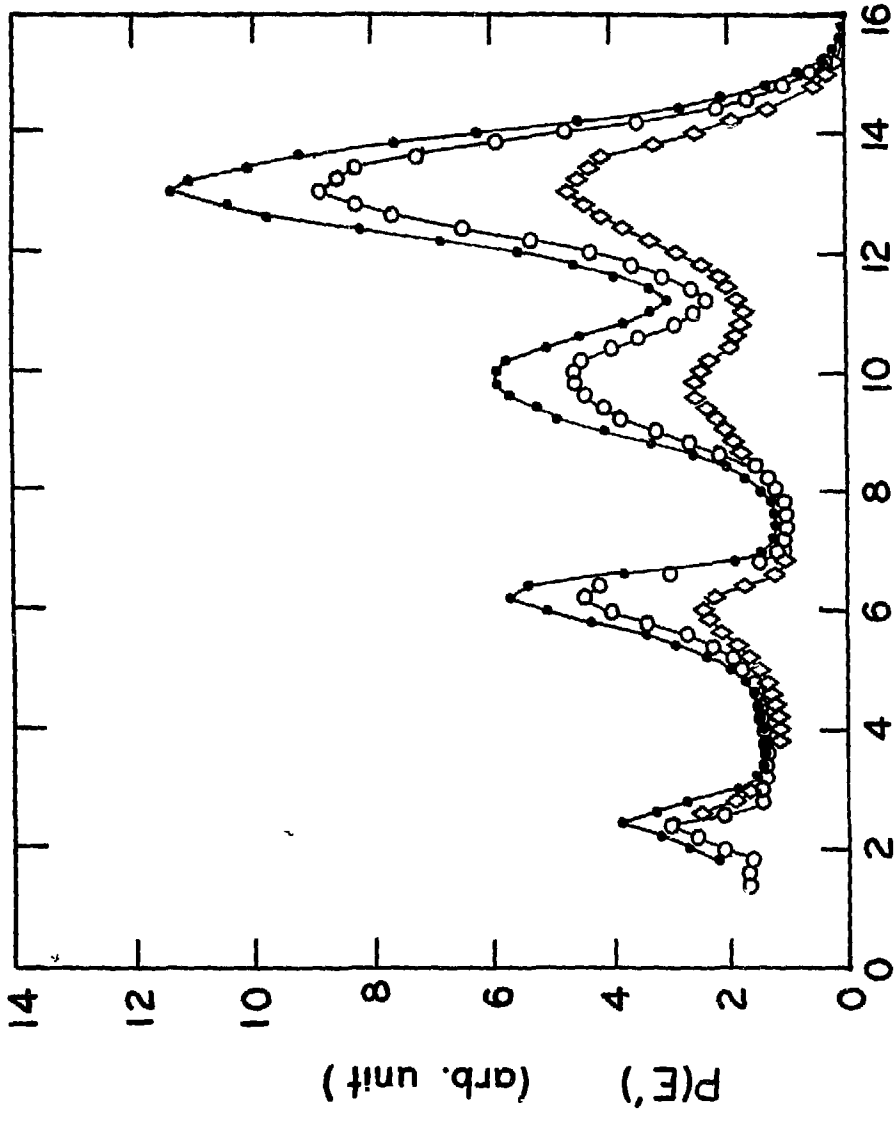

XBL 793-9045

Figure 17

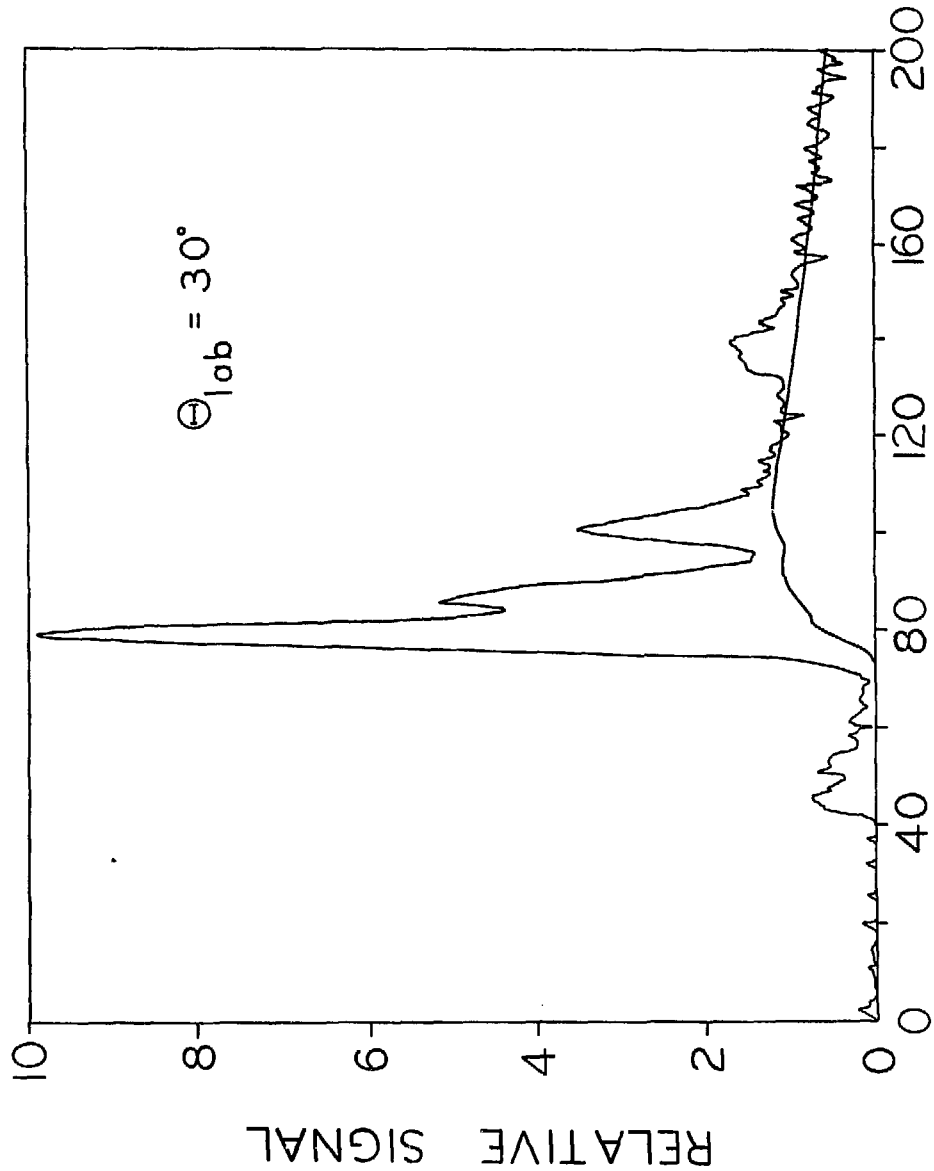

XBL 795-9761

Figure 18

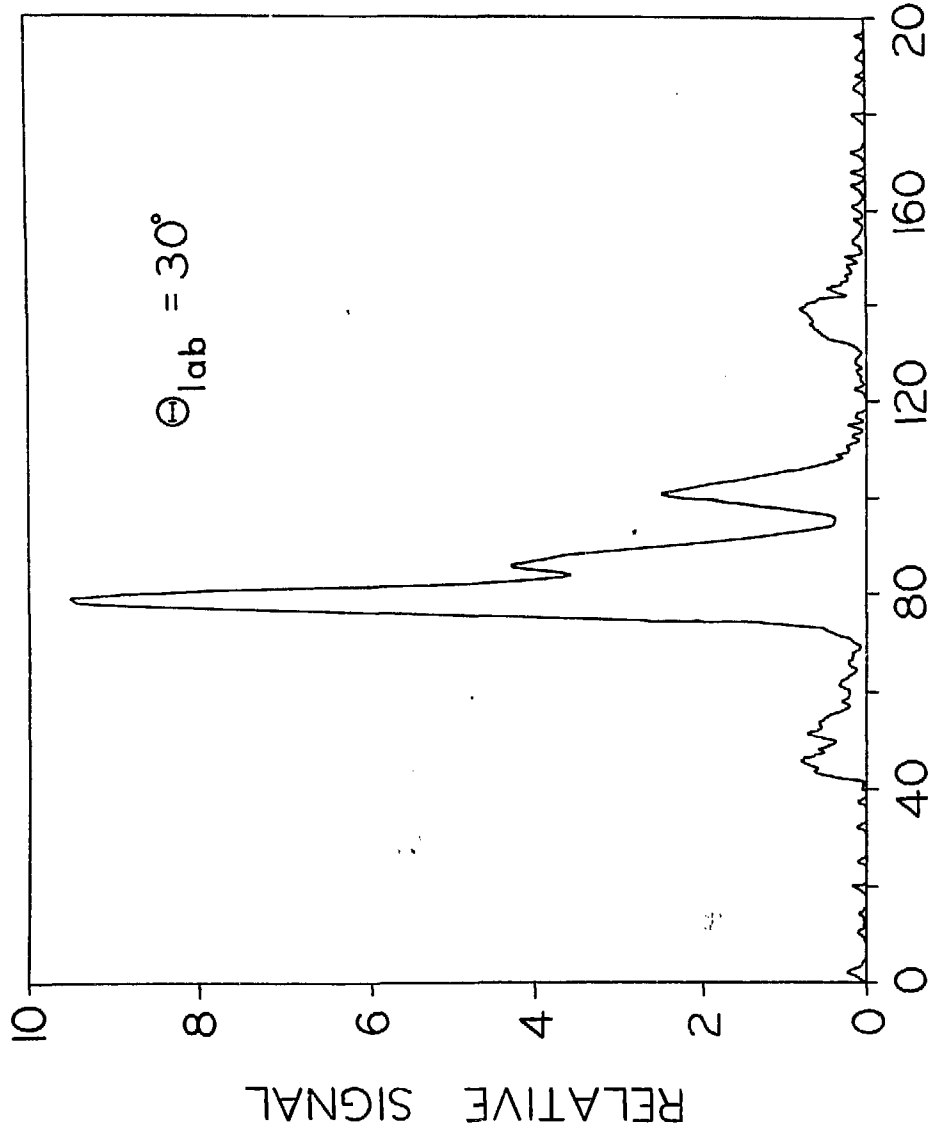

XBL 795-9760

Figure 19

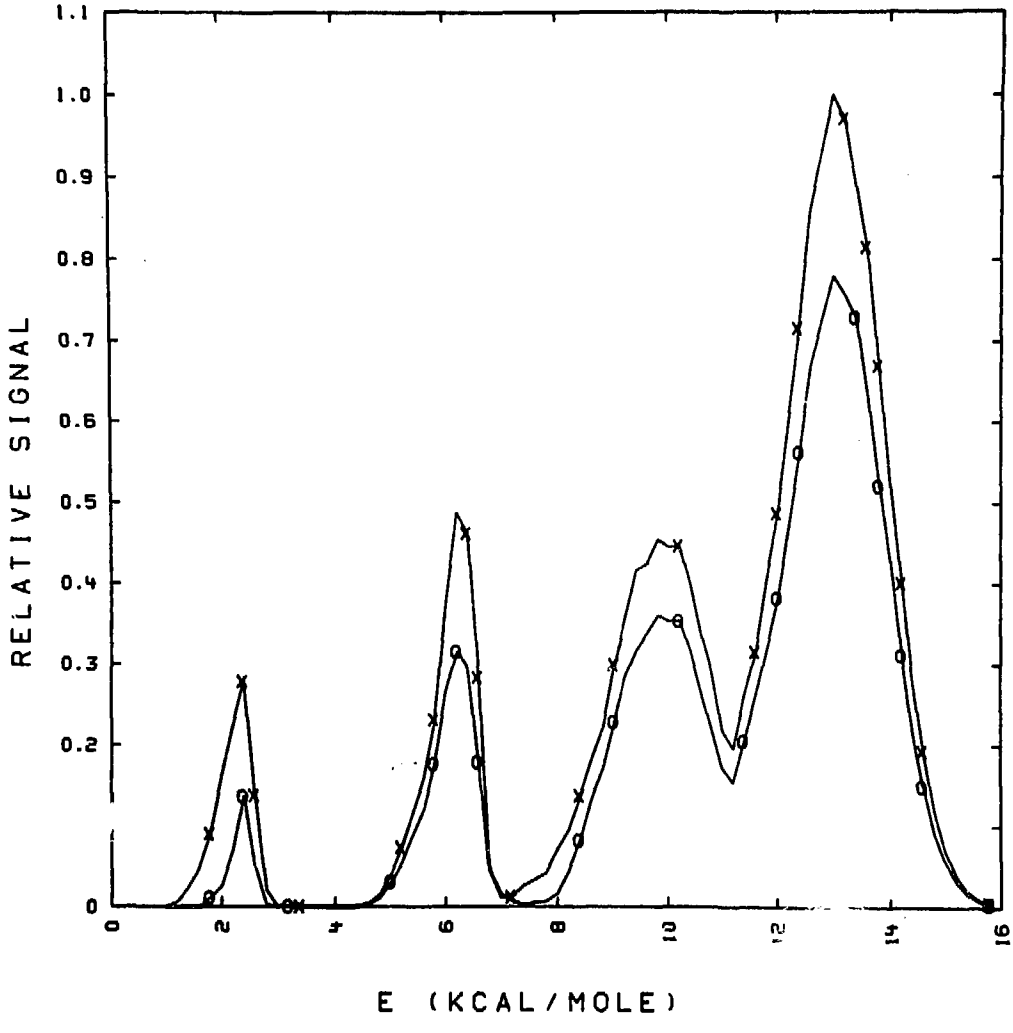

XBL 795-9879

Figure 20

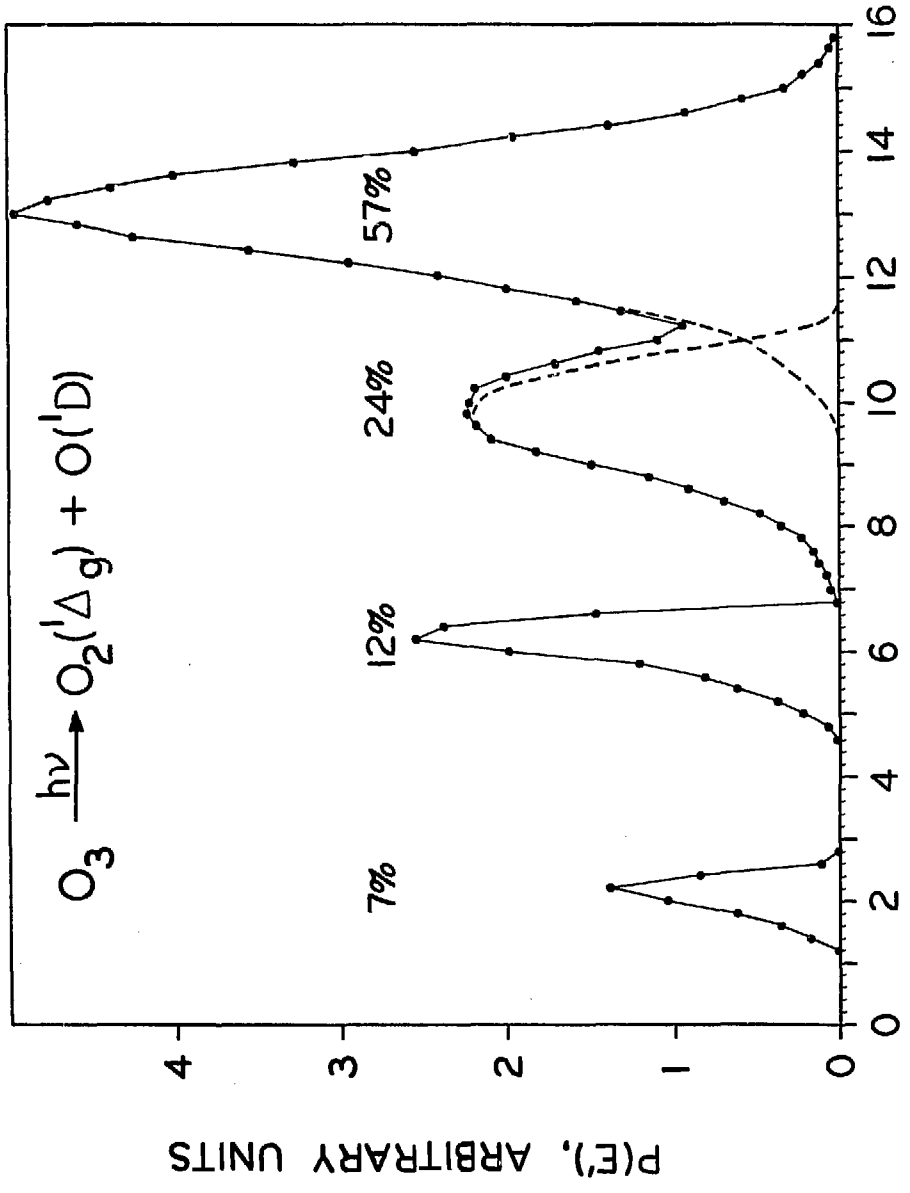

XBL 795-9745

Figure 21

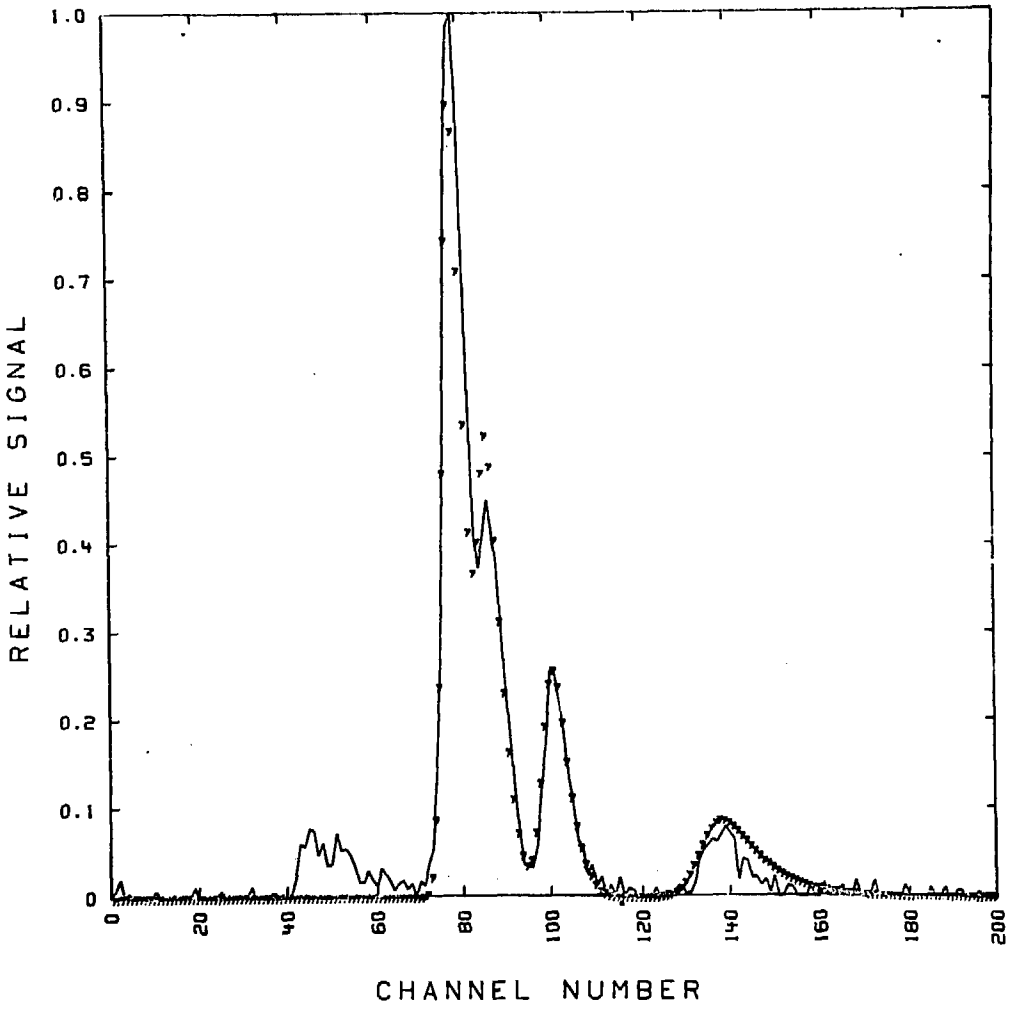

Figure 22 XBL 795-9883

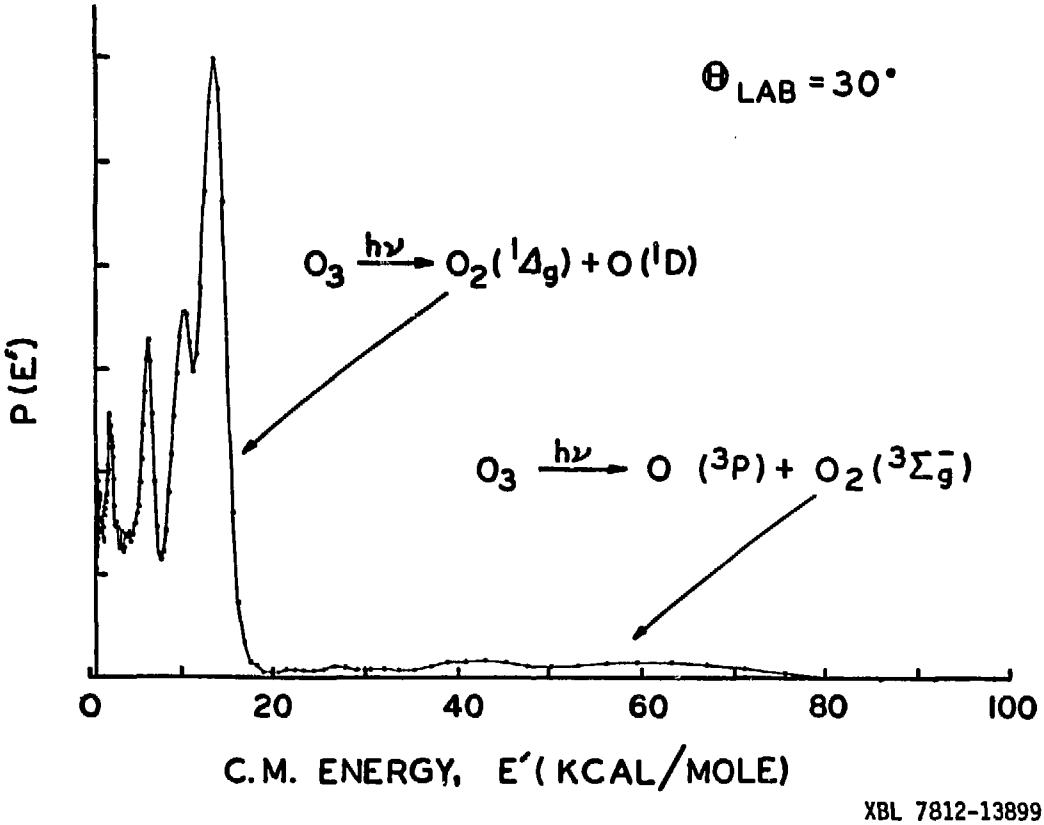

XBL 7812-13899

Figure 23

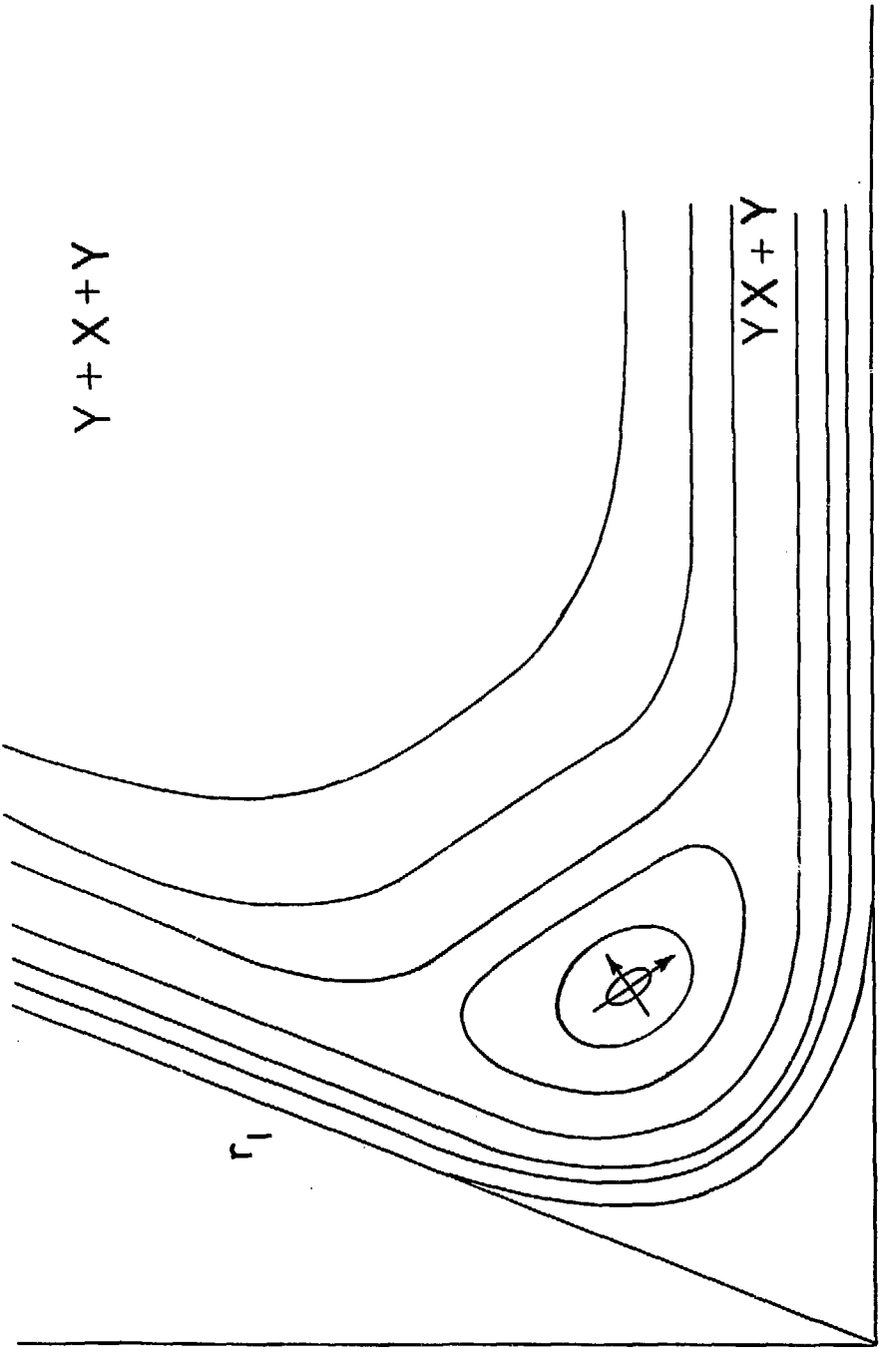

XBL 795-9755

Figure 24

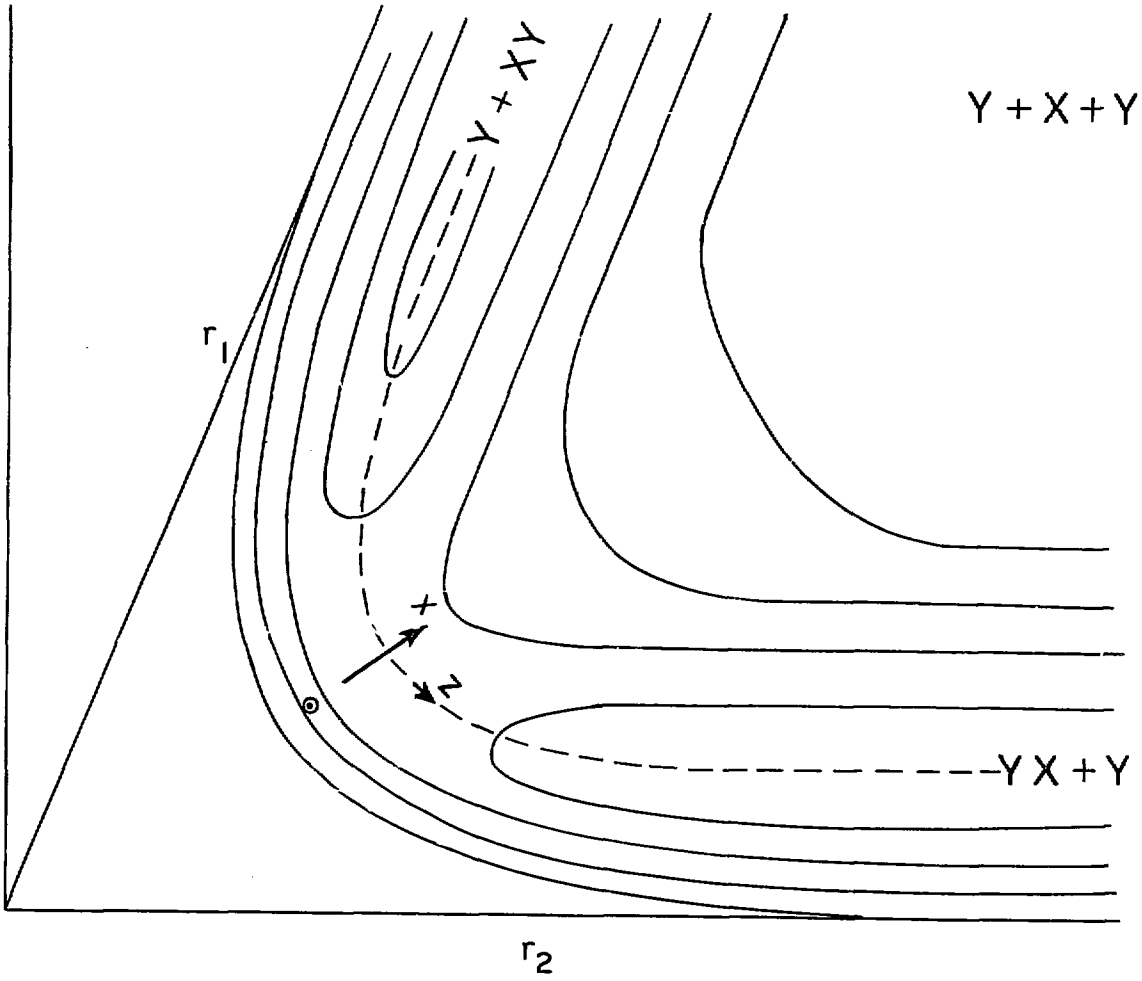

XBL 795-9756

Figure 25

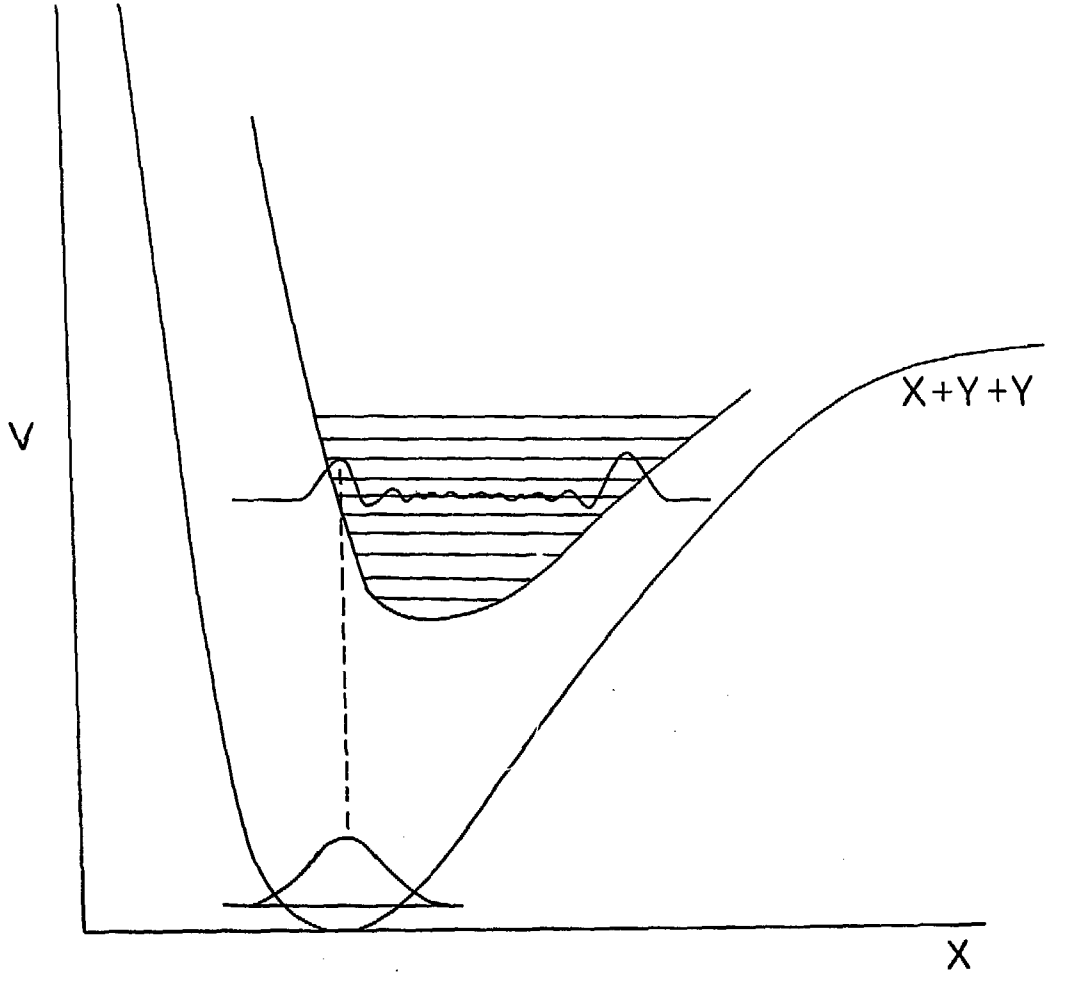

Figure 26

XBL 795-9754

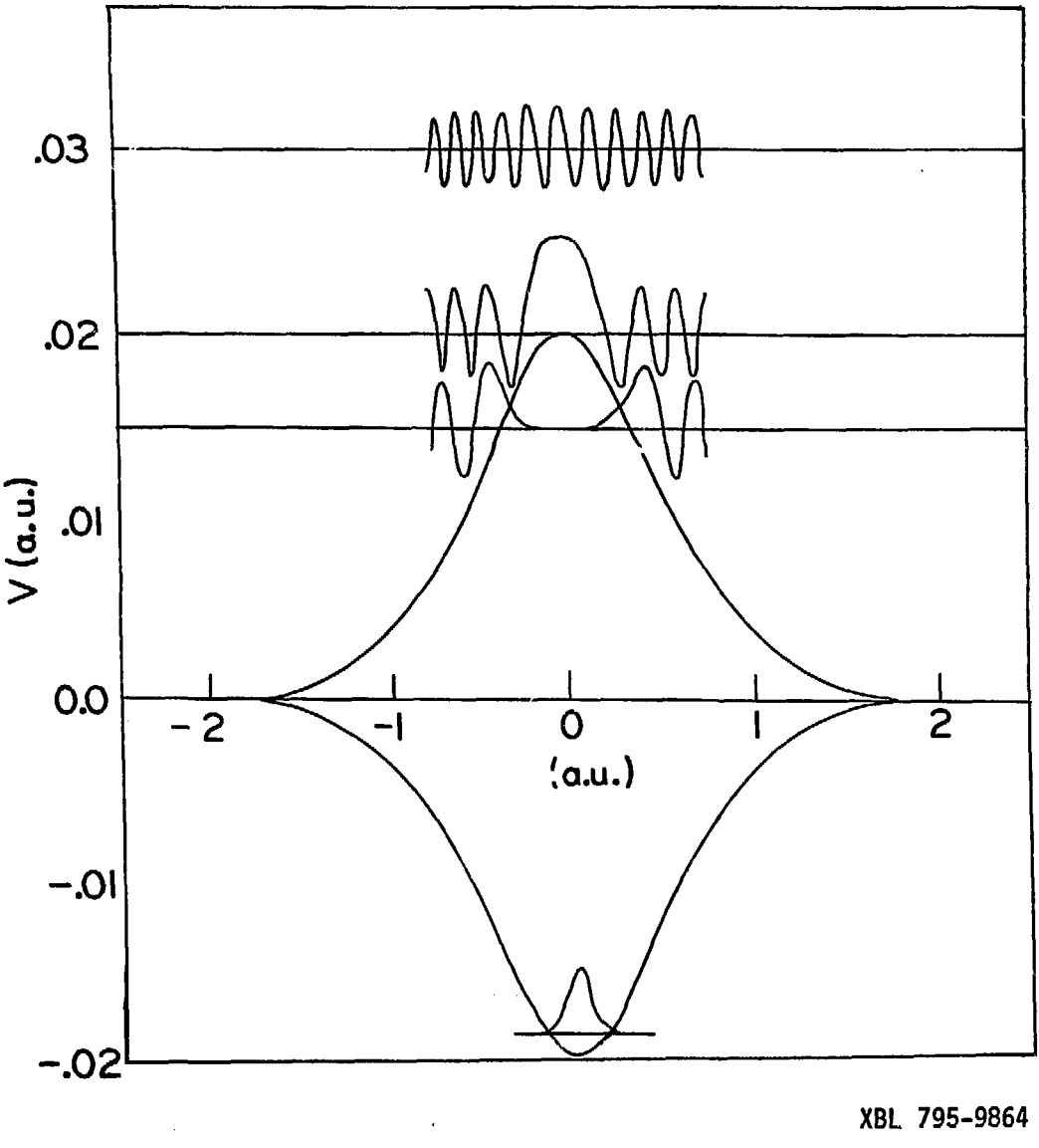

XBL 795-9864

Figure 27

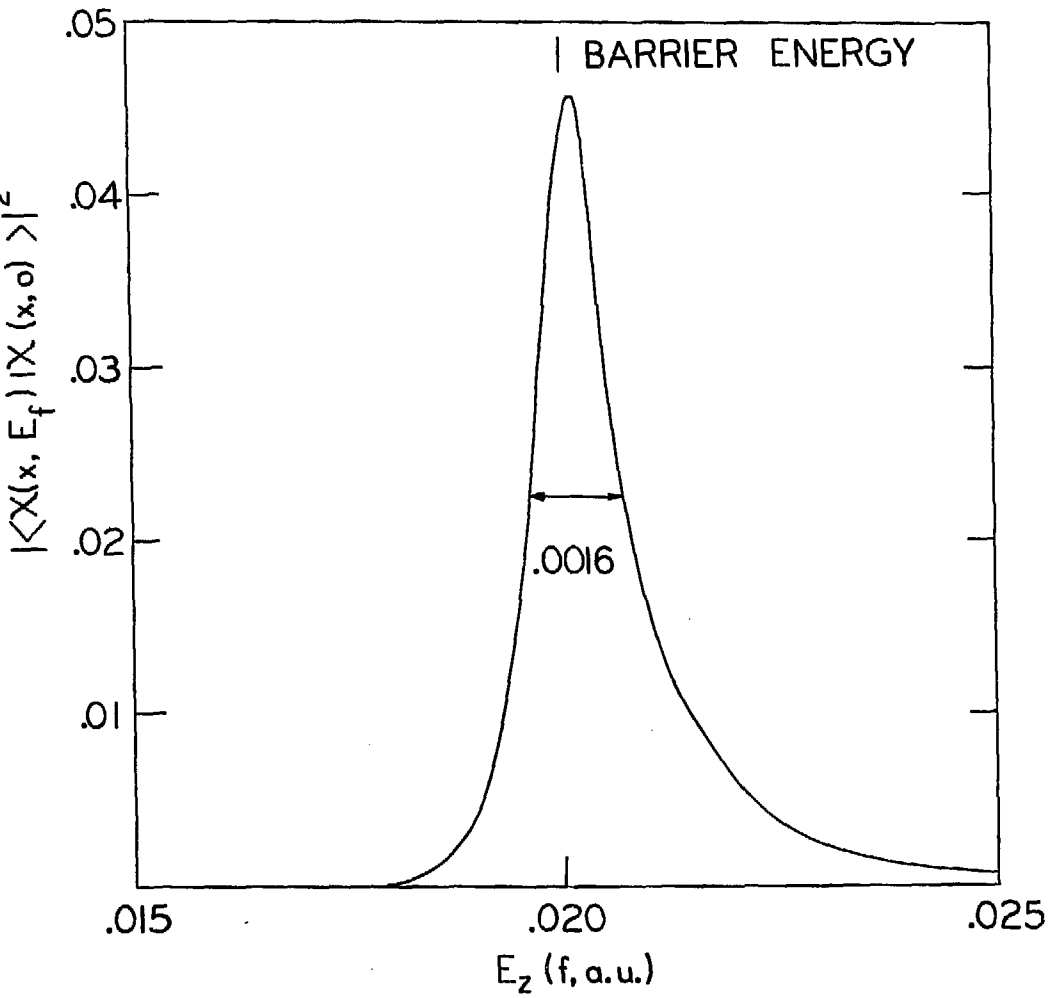

XBL 795-9753

Figure 28

III. INFRARED ABSORPTION SPECTROSCOPY OF MOLECULAR IONS - A PHOTODISSOCIATIVE TECHNIQUE

A. Introduction

Molecular ions are known to play a major role in a large variety of chemical and physical phenomena. Many of these processes, such as electrical conductivity and ion transport in biological systems, occur in condensed phases where the concentration of ions is usually quite substantial. The presence of 10^{20} ion molecules/cm^3 in solution is commonplace to all chemists (~1 molar), and techniques to study the effects and properties of ions in solution are well established. In particular, visible and IR absorption techniques have been used with great utility due to the high ion concentrations possible. Ions are also important in the gas phase. Upper atmospheric chemistry is greatly affected by complex ion molecule reactions, and one also finds ion molecular reactions in events such as combustion where ions are generated in flames.

Study of the chemistry of ions is presently hindered by the scarcity of physical data available. Data commonly available for gas phase neutral molecules such as structure, electron distribution, energy levels, etc. are commonly obtained from spectroscopic data. Chemical structure for neutral molecules is commonly obtained from infrared and microwave data. Similar data for gaseous ions is largely unavailable.

The difficulty in obtaining these data lies primarily in generating an adequate number density of the ions of interest in a given quantum state. At high source pressures, unwanted ion-molecule reactions often deplete the ions of interest and give products which are not intended to be studied. Only in a limited number of cases are the ions inert enough so that this does not occur. At low pressures where ion molecule reactions are not significant, the ion density decreases to the point where absorption or emission techniques become extremely difficult. Where neutral molecule absorption spectroscopy is performed with densities of typically 10^{12} to 10^{15} molecules/cc, ion sources may at most expect to generate 10^{6}-10^{8} ions/cc. They are generally much lower. The difficulty in obtaining absorption data on gaseous ions is therefore apparent. Emission techniques which have been successfully applied to electronic transitions are complicated in the infrared by low sensitivity of detectors and long lifetimes of excited states. Due to low sensitivity obtained with these methods, researchers have developed alternative techniques for obtaining spectra of ions. Photofragmentation spectroscopy has been successfully used for electronic transitions due to the high sensitivity obtained from ion detection.[1-8] Direct application of this technique fails for vibrational transitions because one quantum of vibration energy is insufficient to fragment a chemical bond.

Since photoabsorption techniques are not feasible, infrared spectroscopy is more appropriately obtained by measuring a physical quantity which is sensitive to the vibrational state of the ion molecule. The difference in charge exchange cross sections with respect to vibrational levels has been utilized for diatomic ion molecules with reasonable success although such a technique relies on a small change in a large measured signal (typically 1 part in 10^6).[32,33] Alternately, multiphoton absorption-dissociation has been utilized in an ion trap to measure low frequency vibrations in polatomic ions.[34] This technique (with one laser source) relies on the existence of a quasicontinuum of energy levels such that a single photon frequency can propogate an excitation sequence to the dissociation limit. This approach has thus been limited to ion molecules with more than 11 nuclei.

As mentioned, one quantum of vibrational energy (100-4000 cm^{-1}) will not dissociate most chemical bonds. However, such energies are far in excess of the bonding energy of a van der Waals bond of ions with a He atom which arises from ion induced dipole interactions. If a

molecule absorbs a quantum of vibrational energy, it is possible for this energy to migrate to the van der Waals bond and cause a dissociation of this weakly bonded complex. Thus by tuning the infrared frequency, absorption of this radiation can be observed via the fragmentation process. Helium is a logical choice for the van der Waals aduct due to its high ionization potential and small polarizability. The weak charge induced dipole interactions should largely unaffect the vibrational states of the ion of interest. Since these van der Waals interactions are so weak, it is necessary to produce them at extremely low temperatures. By using a supersonic nozzle, it is possible to obtain rotational temperatures of less than 2°K, thus allowing the formation of the desired complex. Although vibrational absorption features are expected to be affected only slightly by the van der Waals adduct, one would certainly expect the rotation-vibration transitions to be totally altered. The emphasis of this approach, however, is to obtain survey spectra since nothing is known about the structure of most ion molecules. The obscuration of the high resolution features due to the van der Waals

host is, therefore, of no concern here. After such low resolution survey spectra are obtained, it is then possible to obtain the ultimately sought-for high resolution data by techniques such as that described later.

B. Experimental - Vibrational Predissociation of Van der Waals Ions

A tandem mass spectrometer has been constructed in order to study the photodissociation of ion molecules. Figure 1 shows the apparatus. The nozzle, shown in detail in Figure 2, consists of a flow tube containing a Scandium tritide foil from the U. S. Radium Corporation which produces a 4 curie β^- source. The β^- particles produce ions via the following mechanism;

$$\beta^- + He \rightarrow He^+ + 2e^-$$

$$He^+ + M \rightarrow He + M^+$$

The ions produced along with the neutral gas are expanded through a .001-.004 inch orifice, producing the desired supersonic expansion.[9] The orifice is biased at $\pm$ 500 volts which fixes the reference voltage of the system. A skimmer is placed approximately 0.2 inches from the nozzle

in order to eliminate the expansion gas which emanates off axis. It too is held at ± 500 V. Utilizing a series of accelerating lenses (Fig. 3), the ions are given sufficient energy to minimize space charge effects, and allow for easy focusing. The accelerating region is differentially pumped by a 6 inch diffusion pump with Convalex 10 polyphenol ether pump oil. The pump is trapped with a liquid nitrogen cooled baffle. This region maintains a pressure of 10^{-6} torr during the expansion process.

The ions are separated from the neutral species using a parallel plate deflector which directs the ions 15 degrees off axis into an aperture to a 60° sector magnetic mass spectrometer. The flight tube of the mass spectrometer is held at ground potential giving 500 eV ions during the mass analysis. The mass spectrometer is also differentially pumped using a four inch diffusion pump with a liquid nitrogen cold trap. The pressure in this region is maintained at 2×10^{-8} torr during an experiment. It is now possible to mass select the desired van der Waals ion of interest and direct this species into a photoirradiation chamber.

The photoirradiation region is designed for ultra high vacuum operation so that collisional dissociation of the van der Waals complexes is kept to a minimum. This region contains a 220 liter per second ion pump as well as a liquid nitrogen cooled titanium sublimation unit. After

extended pumping, it is possible to obtain a vacuum of 5×10^{-10} torr in this region.

The ions are trapped in the photoirradiation region using a complex radio frequency trapping scheme[10]. A stacked plate design is used in conjunction with an octupole trap as shown in Figure 4. The effect of RF field is complex near the poles, however, the effective field attenuates rapidly by the sixth power of the distance from the central axis.

The amplitude of the RF applied to the poles is typically less than 20 volts. The RF frequency used is 15MHz. By utilizing an impedance matching coil inside the vacuum chamber, the total power dissipated is less than 10 watts. Thus a small RF power supply is adequate for trapping the ions. With this configuration, ions can be collected and stored for several seconds without significant ion loss. Consequently, the ion "bottle" can be filled slowly, and a high power laser pulse can be applied at any convenient time. With this technique the lifetime of the metastable $O_2 + (a^4\pi)$ state has been measured.[11] The ions were prepared in the trap, and allowed to radiate for a specified time interval. A pulsed laser at 532 nm was used to photo-

dissociate the remaining O_2^+ ($^4\pi$) molecules. Thus by measuring the quantity of fragmentation product as a function of storage time, the lifetime is obtained. This scheme is advantageous for van der Waals ion photodissociation experiments since the ion flux is small, and energy transfer times into the van der Waals bond may be long as described below.

In order to detect the absorption of incident radiation, the following mechanism is utilized:

$$M^+ \text{ He} \xrightarrow{h\nu} (M^+)^*\text{He} \rightarrow M^+ + \text{He}$$

For this process to be useful, it is necessary for the energy in the $(M^+)+$ moiety to transfer to the van der Waals bond. The rate at which this process takes place is presently in question. Experiments on the vibronic excitation of HeI_2 and $HeNO_2$ indicate rapid energy transfer with subnanosecond dissociation lifetimes.[12-14] Theoretical studies on the dissociation of ArHCl, however, show dissociation lifetimes as slow as several seconds.[15-18] Ions have a stronger interaction than neutral species which may enhance the energy transfer rate. Also, by using the ion trap, long lived excited state complexes can be stored for a convenient time after irradiation to allow for the energy transfer time.

The photofragments are contained from their recoil trajectory and directed into a quadrupole mass spectrometer for analysis and detection. Since all the ions are contained after fragmentation, the sensitivity of the method is far greater than the dissociation experiments for ozone. Whereas the ozone detection efficiency was one part in one million, here the collection efficiency approaches unity. A further advantage arises since an electron impact ionizer is eliminated. Thus background signals are virtually non-existent. Photofragment production signals as low as one count per minute are possible for these reasons.

The ions are detected using a Daly detector which permits high count rates with large noise discrimination. Even if the total number of counts is small, it is desirable to use a fast counting detector to accommodate burst mode operation when a pulsed laser is used.

The pump laser in these experiments is the same as that used in the ozone experiments. The Nd-Yag laser is directed into an Optical Parametric Oscillator[19] in order to obtain tunable infrared radiation. The 1.06μ output radiation from the Nd-Yag laser is sent through a Faraday Polarization Rotator which keeps retroreflected light from the parametric oscillator from damaging the pump laser. The pump beam is reduced to 3 mm using a

X0.5 telescope. Care must be taken so that secondary reflections from the curved optics do not focus onto the oscillator optics and cause damage. The beam is then sent through a dichroic mirror which has a transmittance of greater than 99% at 1.06μ, and is highly reflective at the output wavelengths. The 1.06μ radiation interacts with a birefringent $LiNbO_3$ crystal which yield parametric gain with output radiation at two frequencies, W_s and W_I, such that

$$W_P = W_I + W_s$$

and the proper phase matching conditions must be met. Using either the signal frequency (W_s) or the idler (W_I) output it is possible to obtain tunable radiation with wavelengths between 1.5 and 4.3 microns. Output power of 20 millijoules per pulse are obtained at 1.8 microns. Vibrational modes of C-H, N-H and similar groups are possible with this frequency range.

Each component of the molecular ion infrared spectrometer has been assembled separately, and performance tests made. Final assembly is now underway and preliminary spectroscopy experiments of supersonically cooled ions should be possible shortly. The vibrational spectrum of $He\text{-}HCl^+$ is proposed since HCl^+ is one of the few molecular ions for which vibrational information is avaiable,[20-26] and the vibrational energy spacings allow the use of the

optical parametric oscillator.

C. Infrared - Ultraviolet Double Resonance Photodissociation Spectroscopy of Molecular Ions

A description has been given for an infrared molecular ion spectrometer which relies on the intramolecular energy transfer in van der Waals compleses. It was noted that in such a scheme, the detailed features of the rovibrational levels will be obscured by the presence of the van der Waals host. It is, therefore, desirable to devise a method which will allow one to obtain the gas phase infrared spectrum of a molecular ion free of perturbations. The photodissociation technique exhibits many advantages in terms of high sensitivity and low noise, however, it is still necessary to provide enough energy for bond rupture.

Consider a molecular system where a molecule in its ground electronic and vibrational state undergoes a transition to an excited state with a photon which is slightly energy deficient to reach the dissociation limit of the excited electronic state. If the molecule is optically pumped to an excited vibrational level of the ground state surface, the system now has enough energy to dissociate using the UV photon which was previously energetically shy of the dissociation limit. No dissociation occurrs with the UV photon until a tunable

infrared source achieves a resonance transition to an excited rovibrational state. Such a scheme would yield optimum results if an upper state surface is available and the Franck-Condon factors from the lower electronic surface are favorable. This method thus relies on the fortuitous existence of electronic states with dissociation energies commensurate with current photon sources.

The application of this technique can also be extended to upper state potential surfaces which are totally repulsive. Utilizing this type of approach is less ideal than using the onset into a continuum from a bound surface, although it may be the only method available for some molecules. In this case, one relies on a significant change in Franck-Condon factors from the ground vibrational level to the excited state.

A favorable molecular ion for testing this technique is HCl^+. The large vibrational spacings allow one to use the optical parametric oscillator for the infrared transition, and the $A^2\Sigma^+$ state is energetically accessible using tunable ultraviolet radiation obtained from nonlinear doubling and mixing of dye laser radiation.[27,28]

The $A^2\Sigma^+ - X^2\pi$ emission spectrum of HCl^+ has been measured and analyzed for four isotopic combinations.[26] This analysis gives both vibrational and rotational

constants for the v = 0,1, and 2 levels of the ground state, and for the v = 0-9 levels of the excited state. The calculated vibrational transition of the ground state is 2568.4 cm^{-1} which corresponds to λ = 3.89 microns. The dissociation energies are also available. For the $X^2\pi$ state the dissociation products are $H(^2S) + Cl^+(^3P)$. Thus

$$D_o(^2\pi) = D_o(HCl) + IP(Cl) - IP(HCl).$$

For the $A^2\Sigma^+$ state the products are $H^+ + Cl(^2P)$. Here one obtains:

$$D_o(^2\Sigma^+) = D_o(HCl) + IP(H) - T_o(^2\Sigma^2\pi) - IP(HCl) \quad \text{with}$$

$D_o(HCl)$ = 4.431eV,[29] I.P.(HCl) = 12.748eV[30], I.P.(Cl) = 13.017eV[31], I.P.(H) = 13.597eV,[32] and $T_o(^2\Sigma-^2\pi)$ = 3.484eV.[26]

The energy to photodissociate is

$$E_{\text{Photon}}^{\text{min}} = T_o(^2\Sigma-^2\pi) + D_o(^2\Sigma) = 5.280\text{eV}.$$

This dissociation energy corresponds to 2348 Å radiation from the ground vibrational state. When a vibrational excitation is made to the v = 1, (E = 2569 cm^{-1}) then the photodissociation energy becomes 4.961eV which corresponds to 2499 Å radiation. (KrF laser yields 2480 Å) One finds

then that any intense source between 2350 Å and 2490 Å is suitable for the photodissociation source.

Extensive studies have been made on the production of tunable UV radiation using a Nd-Yag pump laser.[20-21] Sum-frequency generation from the second harmonics of rhodamine and coumarin dyes allows frequency upconversion to the 208-234 nm range by mixing with the 1064 nm fundamental of the Nd-Yag laser. The dye lasers can be pumped by the second and third harmonics of the Nd-Yag laser. Using the Nd-Yag laser described previously, it is reasonable to expect 1 mjoule of tunable radiation in the UV with no sacrifice in power to the optical parametric oscillator. By using 90° phase matching, greater conversion efficiencies are expected; however, a temperature controlled crystal holder is necessary to obtain the proper phase matching conditions. A thermostat of this type has been developed[33] and this design has been incorporated into the Nd-Yag tunable radiation system.

Using the ion trapping methods previously described, and the UV-IR laser system, generation of infrared spectra of dissociation ions should be readily achieved. If the ion trap can accommodate 10^8 ions/cm^3, with a cylindrical volume of 25 cm^3 accessible to the laser, then one can irradiate 2.5×10^{10} molecules. By allowing the ions to

stagnate in the trap for many millisiconds, it should be possible to obtain at least 1% of the molecules in the ground to vibrational state. If saturation, or near saturation is achieved for the bound-bound infrared transition, the signal production is dependent primarily on the UV photodissociation cross section.

Both the van der Waals ion and the two photon experiments are being actively pursued. After the successful demonstration of the HCl^+ ion it should then be worthwhile to study small polyatomic systems such as H_2O^+, NH_3^+, and CH_5^+.

FOOTNOTES

1. J.B. Ozenne, J. Durup, R. W. Odom, C. Pernot, A. Tabche'-Fouhaille', and M. Tadjeddine, Chem. Phys. 16, 17 (1976).

2. N.P.F.B. van Asselt, J. G. Maas, and J. Los, Chem. Phys. 11,253 (1975)

3. A. Tabche'-Fauhaille', J.Durup, J. T. Moseley, J.B. Ozenne, C. Pernot, and M. Tadjeddine, Chem. Phys. 17,81 (1976)

4. J. T. Moseley, R. P. Saxon, B. A. Huber, P. C. Cosby, R. Abouaf, and M. Tadjeddine, Chem. Phys. 67,1659 (1977)

5. R. Abouaf, B. A. Huber, P. C. Cosby, R. P. Saxon and Moseley, J. Chem. Phys. 68,2406 (1978).

6. M. Tadjeddine, R. Abouaf, P. C. Cosby, B. A. Huber and J. T. Moseley, J. Chem. Phys. 69,719 (1978).

7. D. L. Albritton, J. T. Moseley, P. C. Cosby, and M. Tadjeddine, J. Mol. Spec. 70,326 (1978)

8. A. Carrington, P. G. Roberts and P. J. Sarre, Mol. Phys. 34,291 (1977); Mol Phys 35,1523 (1978).

9. Michael McKeown and Melvin Siegel, American Laboratory, November, 1975.

10. E. Teloy and D. Gerlich, Chem. Phys. 4,417 (1974).

11. D. Gerlich and S. Bustamente, to be published.

12. R. E. Smalley, B. L. Ramakrishna, D. H. Levy, and L. Wharton, J. Chem. Phys, 61,4363 (1974)

13. R. E. Smalley, L. Wharton, and D. H. Levy, J. Chem. Phys., 63,4977 (1975)

14. R. E. Smalley, D. H. Levy and L. Wharton, J. Chem. Phys., 64,3266 (1976).

15. D. A. Dixon, D. R. Herschbach, and W. Klemperer, Faraday Disc. Chem. Soc. 62, 341 (1976)

16. J. A. Beswick and J. Jortner, Chem. Phys. Lett. 49, 13 (1977); J. Chem. Phys. 68, 2277 (1978); J. Chem Phys. 69,512 (1978).

17. G. Ewing, Chem. Phys. 29, 253 (1978)

18. M. S. Child, Faraday Disc. Chem. Soc. 62, 307 (1976).

19. R. L. Byer, and R. L. Harbst, Top. Appl. Phys. 16, 81 (1977).

20. A. Brice and F. A. Jenkins, Nature 123, 944 (1929)

21. M. Kulp, Z. Phsysik 67, 7 (1931).

22. F. Norling, Z. Physik 104, 638 (1937)

23. F. Norling, Z. Physik 106, 177 (1937)

24. L. Marsigny and J. Ferran, C. R. Acad. Sci. Ser. C 262, 531 (1966).

25. L. Marsigny and P. Deschamps, C. R. Acad. Sci. Ser. C 256, 352 (1963)

26. W. David Sheasley and C. Weldon Mathews, J. Nol. Spectros. 47, 420 (1973)

27. Gail A. Massey, and Joel C. Johnson, IEEE J Quant Elect. QE12, 721 (1976)

28. Gail A. Massey, Appli. Phys. Lett. 24, 371 (1974)

29. B. Rosen, Ed, "Spectroscopic Data Relative to Diatomic Molecules," (Reyamon Press, Oxford, 1970)

30. K. Watanabe, J. Chem. Phys. 26, 542 (1957)

31. B. G. West and M. Mizushima, Phys. Rev. 143,31 (1966).

32. William H. Wing, George A. Ruff, Willis E. Lamb Jr. and Joseph J. Spezeski, Phys. Rev. Lett. 36, 1488 (1976).

33. Alan Carrington and Peter Sarre, Mol. Phys 33, 1495 (1977).

34. Chemical and Biochemical Applications of Lasers Vol. IV Edt. C. Bradley Moore. (Academic Press, New York) 1979.

FIGURE CAPTIONS

Fig. 1 Schematic Diagram of tandem mass spectrometer with supersonic ion nozzle source.

Fig. 2 Supersonic nozzle source for the production of ion molecules.

Fig. 3 Ion dense system for first differential pumping region.

Fig. 4 R. f. ion trap and octupole trap

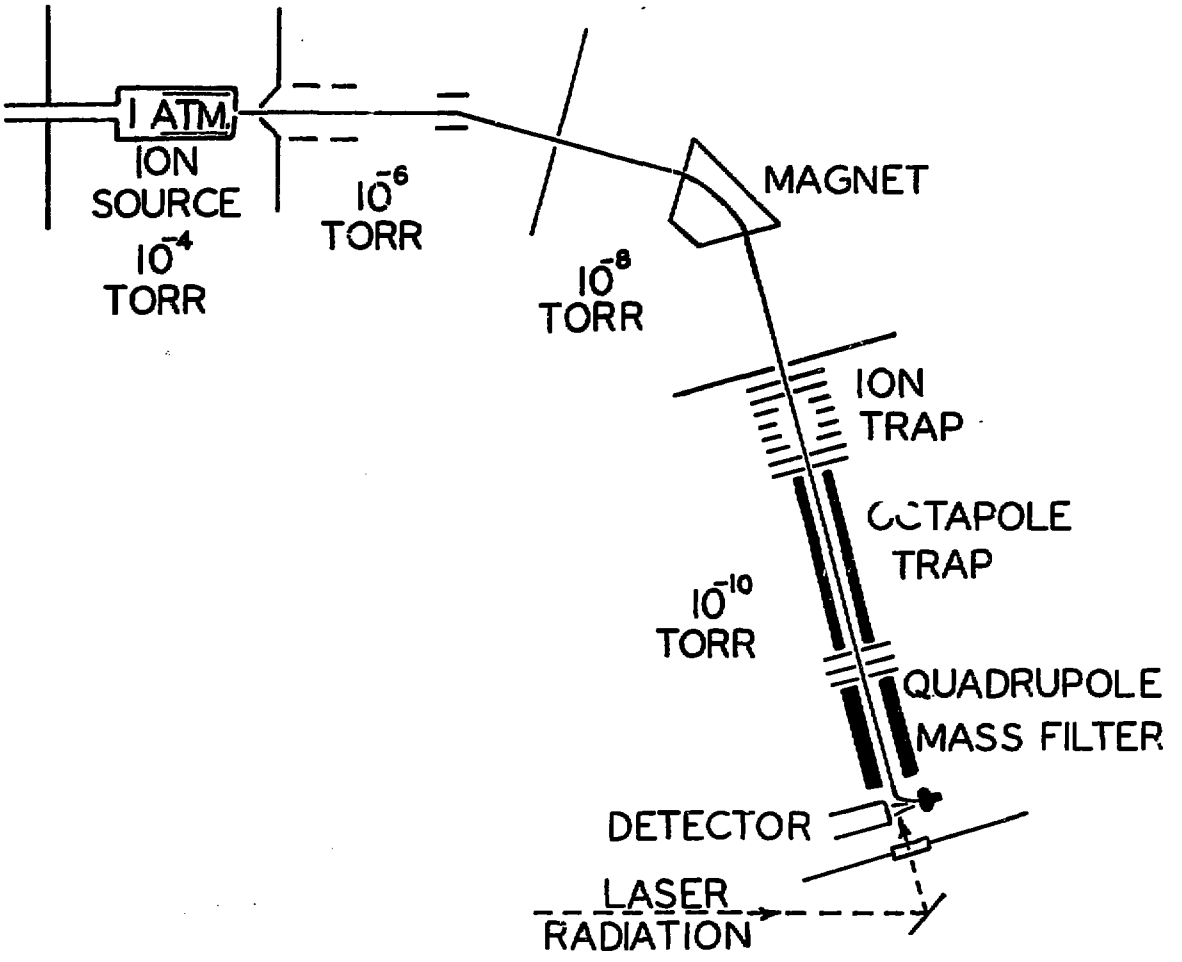

Figure 1

XBL 7812-13895

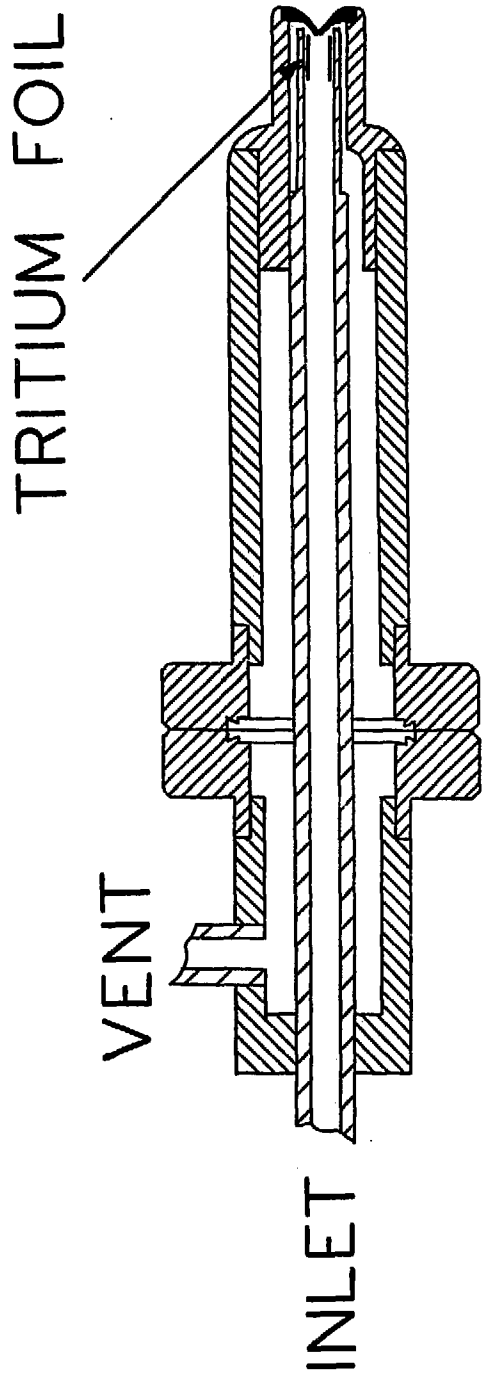

XBL 795-9758

Figure 2

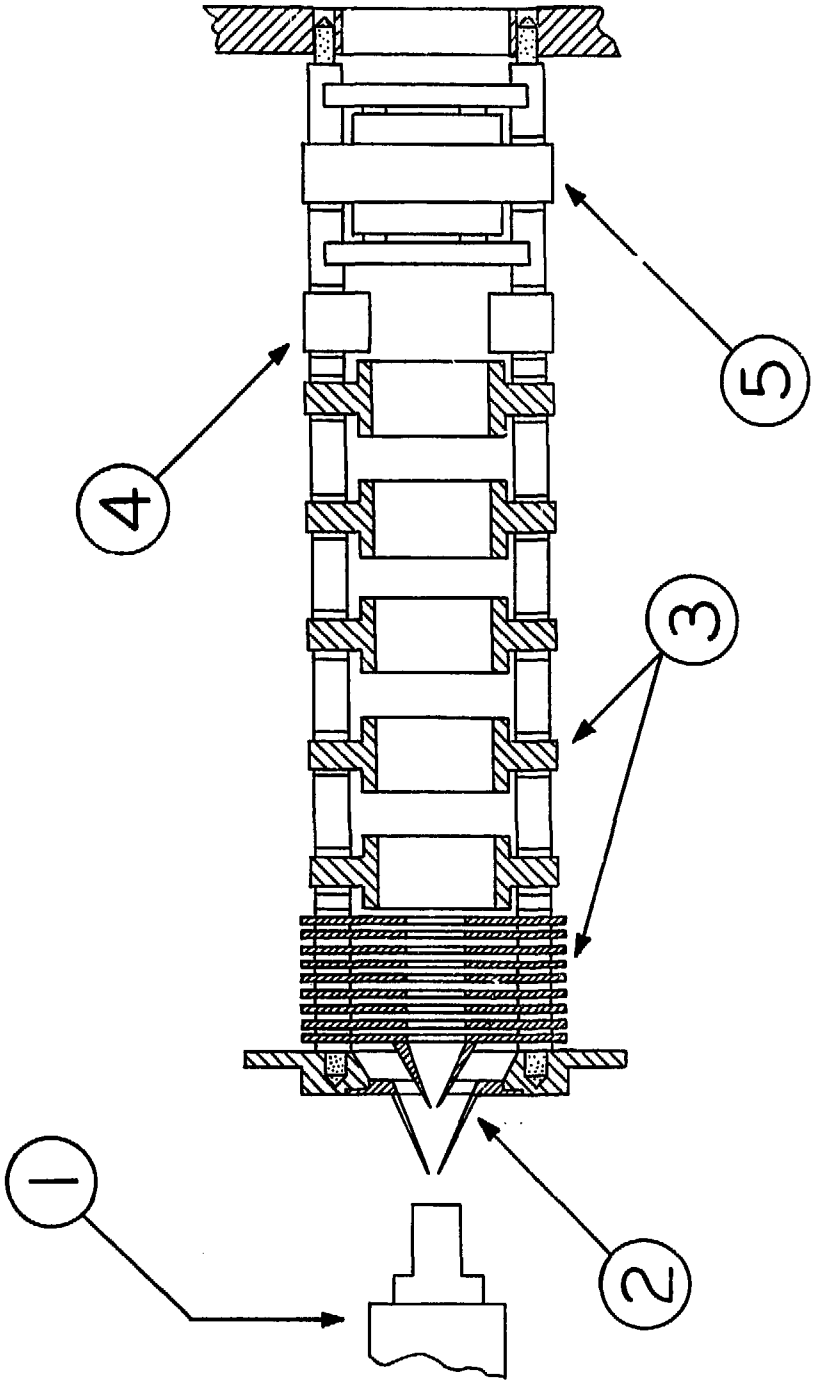

XBL 795-9759

Figure 3

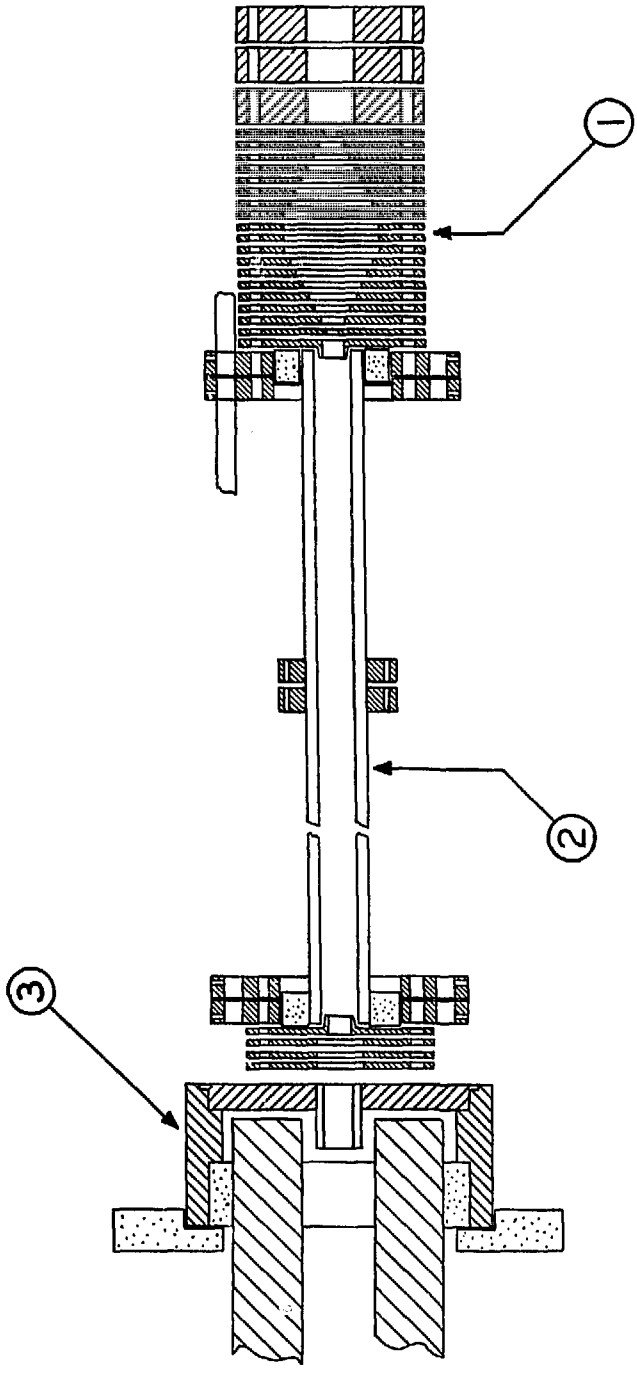

XBL 795-9752

Figure 4

APPENDIX A

Simulation Studies of Photodissociation

The following Fortran IV program is designed to simulate the dynamics of a photodissociation event in a crossed molecular beam facility. The use of such a program allows one to determine the resolution of a photofragment spectrometer, and can be used to determine which parameters of the apparatus degrade the experimental resolution. Thus by studying the effects of each beam parameter, one can design an optimal experiment.

Input

The program first accepts parameters relevant to the desired experiment.

Card Group I

I Card 1.	BMASS, FMASS	2F7.2 Format BMASS is the mass of the parent molecule in A.M.U. FMASS is the mass of the observed fragment in A.M.U.
I Card 2.	ENGION, IONLGT	2F7.2 Format ENGION is the energy of the ion in eV. which is analyzed by the mass spectrometer. It is assumed the have constant velocity over the entire region. IONLGT is the flight path of the ion formed in centimeters.

I Card 3.	ANGLE	F7.2 Format ANGLE is the angle of the detector with respect to the molecular beam, and is given in degrees.
I Card 4.	BLONG	F7.2 Format BLONG is the distance from the nozzle tip to the center of the interaction region in cm.
I Card 5.	FGPATH	F7.2 Format FGPATH is the distance from the center of interaction region to the center of the ionizer, in cm.
I Card 6.	FDWELL	I2 Format FDWELL is the time interval (in microseconds for integration of each channel of the multichannel scaler used for time of flight.
I Card 7.	PANGL	F7.2 Format PANGL is the angle (degrees) of laser E vector with respect to the molecular beam. It is assumed that the molecular beam, laser beam, and detector are all in the same plane, and that the two beams are orthogonal.
I Card 8.	POLA POLC	2F7.2 Format POLA and POLC are two factors in the equation:

$$PPROB = POLA \cos^2(v) + POLC$$

		where PPROB is the relative transition probability at a given polarization angle in the center of mass frame (v). This equation applies to parallel transitions. For isotropic fragmentation, this statement may be extracted from the program, or POLA = 0 and POLC = 1
I Card 9.	BVMIN, BVMAX	2F10.2 Format BVMIN and BVMAX are the minimum and maximum velocities desired for the beam velocity distribution. They are given in cm/sec.
I Card 10.	BVINC	F7.2 Format BVINC specifies the incremental velocity in which to convolute the beam velocity distribution.(cm/sec)
I Card 11.	TS	F7.2 Format TS is the translational temperature of the beam in degrees Kelvin.
I Card 12	AVMASS	57.2 Format AVMASS is the average mass of the molecular beam gas mixture in A.M.u.
I Card 13.	VS	F10.2 Format VS is the most probable velocity of the molecular beam. The velocity distribution of the beam is generated by

$$I(V) = C\, u^2 \exp\left(\frac{AVMASS}{2kTS}\right)(V-VS)^2$$

Card Group II. Beam Angular Distribution Function

BMANGL(I), BMAPRB(I), JDONE 2F6.2, I3 Format.

BMANGL(I) is the angular distribution (degrees) of the beam. Both positive and negative angles are permitted. 0 degrees is the beam axis.

BMAPRB(I) is the beam intensity corresponding to each beam angle.

JDONE is an indicator that the last beam angle has been given. If JDONE is non zero, the reading of beam angles and intensities is terminated.

Card Group III - Detector Angular Distribution

DTANGL(I), DTAPRB(I), JDONE 2F6.2, I3 Format.

DTANGL(I) is the angular deviation (degrees) from the angle given in ICard 3. Both positive and negative angles are permitted.

DTAPRB(I) is the detecting probability corresponding to each deviation angle.

JDONE indicates last detector deviation angle to be read. If JDONE is non zero, detector angles are terminated.

Card Group IV - Ionizer Spatial Distribution

IONIZR(I), IONPRB(I), JDONE 2F6.2, I3 Format

IONIZR(I) is the distance from the center of the ionizer (cm.). Negative distances yield a smaller fragment path length.

IONPRB(I) is the ionization probability as a function of ionizer spatial distribution.

JDONE indicates last ionizer card. If JDONE is not equal to zero, reading of ionizer cards is terminated.

Card Group V - Laser Spatial Distribution

LASER(I), LSRPRB(I), JDONE 2F6.2,I3 Format

LASER(I) is the deviation of the laser (in cm.) from the laser beam axis. Both positive and negative values are permitted where the axis is zero.

LSRPRB(I) is the laser intensity associated with a given spatial point

Sample Input

```
                PHOTOFRAGMENTATION SIMULATION

                        INPUT DATA

 48.ØØ    32.ØØ
 8Ø.ØØ    24.ØØ
 2Ø.ØØ
  5.45
 34.11
3
 ØØ.ØØ                              Experimental Parameters
 ØØ.ØØ     1.ØØ                        Card Group I
 48ØØØ.ØØ    62ØØØ.ØØ
2ØØ.ØØ
  2.ØØ
 4Ø.ØØ
 558ØØ.ØØ

 -1.ØØ     1.ØØ
 -Ø.75     1.ØØ
 -Ø.5Ø     1.ØØ
 -Ø.25     1.ØØ
  Ø.ØØ     1.ØØ                  Beam Angles (Deg.)
  Ø.25     1.ØØ                    Card Group II
  Ø.5Ø     1.ØØ
  Ø.75     1.ØØ
  1.ØØ     1.ØØ  1
```

```
-1.ØØ    1.ØØ
-Ø.75    1.ØØ
-Ø.5Ø    1.ØØ
-Ø.25    1.ØØ
 Ø.ØØ    1.ØØ          Detector Deviation Angle (Deg.)
 Ø.25    1.ØØ                Card Group III
 Ø.5Ø    1.ØØ
 Ø.75    1.ØØ
 1.ØØ    1.ØØ  1

-1.ØØ    Ø.1Ø
-Ø.8Ø    Ø.5Ø
-Ø.6Ø    Ø.8Ø
-Ø.4Ø    Ø.99
-Ø.2Ø    Ø.8Ø          Ionizer Position (cm)
 Ø.ØØ    Ø.6Ø              Card Group IV
 Ø.2Ø    Ø.4Ø
 Ø.4Ø    Ø.2Ø
 Ø.6Ø    Ø.1Ø
 Ø.8Ø    Ø.Ø5
 1.ØØ    Ø.Ø2  1

-Ø.6Ø    Ø.5Ø
-Ø.4Ø    1.ØØ
-Ø.2Ø    Ø.75          Laser Position (cm)
 Ø.ØØ    Ø.2Ø               Card Group V
 Ø.2Ø    Ø.75
 Ø.4Ø    1.ØØ
 Ø.6Ø    Ø.5Ø  1

 1.6Ø
 1.4Ø
 1.2Ø                  Energies to Simulate (Kcal)
 1.ØØ
 Ø.8Ø
 Ø.6Ø  1
```

Details of Simulation

The convolution of beam distributions is performed by selecting an energy (ENGDIS(JJ)), and calculating the components of a Newton diagram for in plane scattering (vertical scattering has been ignored in this program) by generating all presentations of the beam angle, detector angle, detector angle, beam velocity, laser, and ionizer specified from the above input. A laboratory velocity is calculated for both forward and backward scattered products, thus a flight time is obtained which is histogrammed from all the

presentations of a given energy. The final histogram is saved as a time of flight spectrum for a single fragment energy. This process is repeated for a new energy until all input energies have been processed. The matrix generated can then be used either to observe the spread in time at any given energy, or can be used in data fitting routines to obtain energy distributions in the center of mass coordinate frame, via least squares or trial and error fits.

Calculation of Laboratory Angle and Fragment Flight Path

The geometric details for calculating the laboratory angle and fragment flight path are shown in Figure 1. The angle and distance labels correspond to the variables in the program. Using the geometry shown, a matrix is formed for the interaction region, and ionizer region from the various combinations of beam angle, detector angle, ionization point, and excitation point. The angle calculated is used for the calculation of the Newton triangle shown in Figure 2.

Coordinate Transformation Calculations

As shown in Figure 2, the forward and backward scattered laboratory velocities of the photofragment are obtained from the input data. During this calculation, checks are made for maximum possible laboratory angle, and flight times which exceed 256 channels with the specified

integration time. No account has been made in this program for momentum transfer from the photon, to the molecular beam.

Since the ionizer is linearly responsive to number density, and the variable of interest is flux, a velocity factor must be incorporated into the intensity expression. The Jacobian for the transformation from center of mass to laboratory coordinates must also be incorporated, thus the response as a function of laboratory velocity is weighted by $(V_{LAB})^3/(Vcm)$. See page 33.

Polarization Dependence of the Angular Fragment Distribution

The polarization dependence for anisotropic scattering is described in the introductory chapter. The theory described, however, is applicable only for single energy fragemnts. Thus the polarization dependence should actually have energy dependent coefficients. This can be easily incorporated into the program, although presently omitted, by vectoring POLA and POLC in the polarization dependence coding for both forward and backward scattering. Thus

```
PPROB = POLA(JJ) * (COS(GAMMA) ** 2) + POLC(JJ)
```

It should also be mentioned that COS(GAMMA) in the above equation is applicable only for parallel transitions and should be changed to SIN(GAMMA) for the perpendicular case.

Output

The mode of output is dependent on the program card which specifies the actual output device for each logical device. The logical device outputs are as follows:

Logical Unit 6 outputs all the input data

Logical unit 20 outputs the simulated time of flight data

For each energy to be simulated, the program outputs the energy used (Kcal) in F10.4 format. 256 intensities follow for a simulated time of flight in 1P6E13.5 format. A sample of logical unit 20 output is:

OUTPUT FORMAT OF PHOTOFRAGMENT
TIME OF FLIGHT SIMULATION

1.2000

0.	0.	0.	0.	0.	0.
0.	0.	0.	0.	0.	0.
0.	0.	0.	0.	0.	0.
0.	0.	0.	0.	0.	0.
0.	0.	0.	0.	0.	0.
0.	0.	0.	0.	0.	0.
0.	0.	0.	0.	0.	0.
0.	0.	0.	0.	0.	0.
0.	0.	0.	0.	0.	0.
0.	0.	0.	0.	0.	0.
0.	0.	0.	0.	0.	0.
0.	0.	0.	0.	0.	0.
0.	0.	0.	0.	0.	0.
0.	0.	0.	0.	0.	0.
0.	0.	0.	0.	0.	0.
0.	0.	0.	0.	0.	0.
0.	0.	0.	0.	0.	0.
0.	0.	0.	0.	0.	0.
0.	0.	0.	0.	0.	0.
0.	0.	0.	0.	0.	0.
0.	0.	0.	0.	0.	0.
0.	0.	0.	0.	0.	0.
0.	0.	0.	0.	0.	0.
0.	0.	0.	0.	0.	0.
0.	0.	0.	0.	0.	0.
0.	0.	0.	0.	0.	0.
0.	0.	0.	0.	0.	0.
1.31528E+13	1.87998E+14	1.01699E+15	3.21517E+15	7.28665E+15	1.33119E+16

2.08746E+16	2.96792E+16	3.91219E+16	4.78295E+16	5.57954E+16	6.34358E+16
7.00582E+16	7.48941E+16	7.82517E+16	7.86293E+16	7.65663E+16	7.13219E+16
6.49317E+16	5.84799E+16	5.27965E+16	4.58198E+16	3.89773E+16	3.26740E+16
2.73669E+16	2.25074E+16	1.81865E+16	1.40097E+16	1.05904E+16	7.93230E+15
5.83780E+15	4.05615E+15	2.93043E+15	2.04841E+15	1.44817E+15	1.01822E+15
7.45833E+14	5.36469E+14	3.83708E+14	2.97576E+14	2.20564E+14	1.71301E+14
1.28713E+14	1.09206E+14	7.56838E+13	6.54116E+13	5.28204E+13	4.28887E+13
3.56433E+13	2.45048E+13	1.70478E+13	1.71444E+13	1.44203E+13	1.08700E+13
7.73900E+12	5.98313E+12	5.38496E+12	4.51511E+12	3.99447E+12	4.76000E+12
3.64305E+12	5.68572E+12	4.90136E+12	8.16731E+12	7.76951E+12	9.32472E+12
9.90685E+12	1.21299E+13	1.56762E+13	1.26215E+13	1.63679E+13	2.20520E+13
1.54704E+13	2.45467E+13	2.39082E+13	2.60103E+13	2.88882E+13	3.08104E+13
3.48783E+13	3.67848E+13	3.95113E+13	4.32157E+13	4.67046E+13	5.08105E+13
5.28472E+13	6.16233E+13	6.27105E+13	7.02403E+13	7.26526E+13	8.57310E+13
7.85477E+13	9.48299E+13	1.01436E+14	0.		
1.0000					
0.	0.	0.	0.	0.	0.
0.	0.	0.	0.	0.	0.
0.	0.	0.	0.	0.	0.
0.	0.	0.	0.	0.	0.

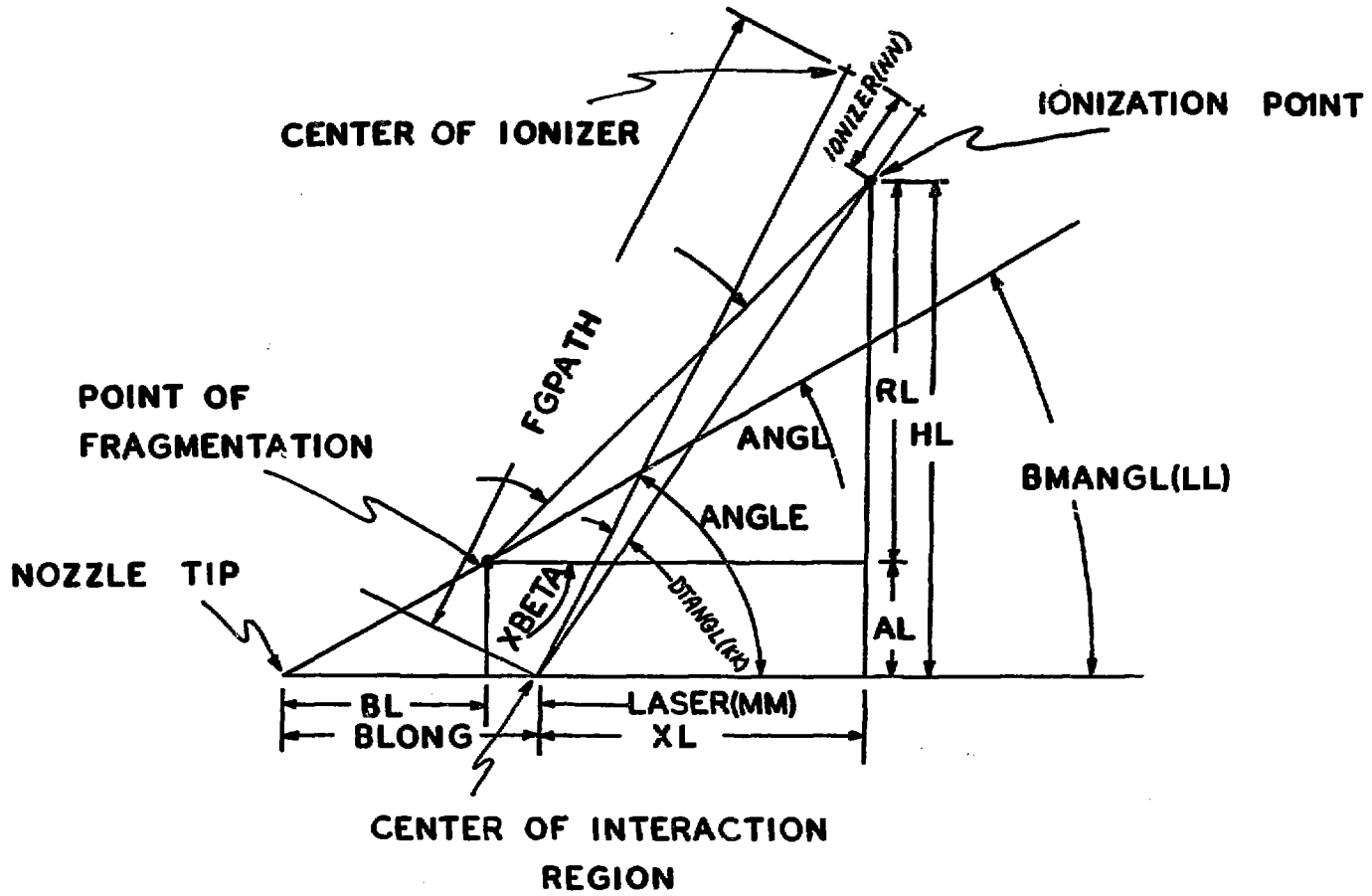
CENTER OF IONIZER
IONIZER(MM)
IONIZATION POINT
FGPATH
POINT OF
FRAGMENTATION
RL
HL
ANGL
BMANGL(LL)
ANGLE
NOZZLE TIP
XBETA
DTANGL(RX)
AL
BL
LASER(MM)
BLONG
XL
CENTER OF INTERACTION
REGION

XBL 795-9737

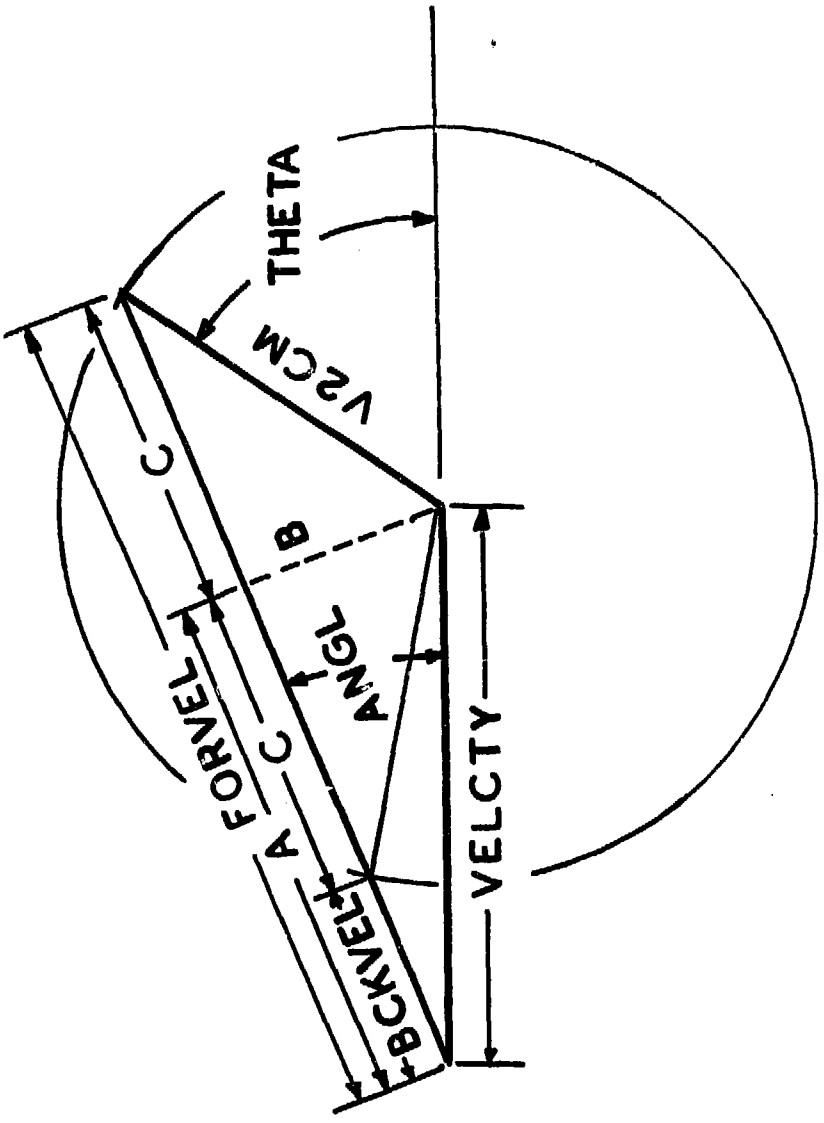

XBL 795-9736

```
      PROGRAM WJ(DIALOG,TAPE7=DIALOG,PARAMETERS,TAPE6=PARAMETERS,
     1  DATACMLAB,TAPE13=DATACMLAB,BMANGLE,TAPE14=BMANGLE,
     2  DTANGLE,TAPE15=DTANGLE,IONIZER,TAPE16=IONIZER,
     3  FLASER,TAPE17=FLASER,ENGPROB,TAPE18=ENGPROB,
     4  CONVDATA,TAPE20=CONVDATA)
C * * * * * * * * * * * * * * * * * * * * * * * * * * * * * * * *
C * * * * * * * * * * * * * * * * * * * * * * * * * * * * * * * *
C
C                PHOTOFRAGMENTATION SIMULATION PROGRAM
C
C * * * * * * * * * * * * * * * * * * * * * * * * * * * * * * * * *
C * * * * * * * * * * * * * * * * * * * * * * * * * * * * * * * *
      REAL IONLGT
      REAL VELDIS(256),VPROB(256),TFHIST(1000)
      REAL BMAPRB(50),BMANGL(50),IONIZR(50),LASER(50),IONPRB(50)
      REAL DTANGL(50),DTAPRB(50),ENGDIS(256),LSRPRB(50)
      INTEGER FCHAN,AV,FDWELL
C
C  THIS PROGRAM PERFORMS A CENTER OF MASS TO LAB TRANSFORMATION
C  FOR A SINGLE BEAM PHOTOFRAGMENTATION PROCESS.
C
C  INPUT
C  THE INPUT PARAMETERS TO THE PROGRAM ARE:
C    1.  CENTER OF MASS FRAGMENT TRANSLATIONAL ENERGY DISTRIBUTION
C    2.  VELOCITY DISTRIBUTION PARAMETERS
C    3.  ANGULAR DISTRIBUTION OF BEAM
C    4.  ANGULAR DISTRIBUTION OF DETECTOR
C    5.  POLARIZATION FUNCTION OF MOLECULE--EG. B PARAMETER
C    6.  IONIZER PROBABILITY DISTRIBUTION
C    7.  LASER DISTRIBUTION
C
C     FILE NAMES--LLL VERSION ONLY
C     THE FOLLOWING FILES MUST EXIST BEGORE PROGRAM EXECUTION:
C      1.  ENERGY DISTRIBUTION=ENGPROB
C      2.  ANGULAR INTENSITY OF BEAM=BMANGLE
C      3.  ANGULAR FUNCTION OF DETECTOR=DTANGLE
C      4.  IONIZATION PROBABILITY=IONIZER
C      5.  LASER SPATIAL DISTRIBUTION=FLASER
C      6.  INITIAL CONDITIONS=DATACMLAB
C
C
C   READ THE EXPERIMENTAL PARAMETERS FROM DISK
C  SET UP CONDITIONS FOR PROGRAM RUN
C
C
C  DATA OBTAINED FROM DATACMLAB FILE ARE:
C
C    1.  MOLECULAR WEIGHT OF MOLECULE (AMU)
C    2.  MOLECULAR WEIGHT OF FRAGMENT (AMU)
C    3.  ION ENERGY (EV)
C    4.  ION FLIGHT LENGTH (CM)
C    6.  DETECTOR ANGLE  (DEGREES FROM PRIMARY BEAM)
C    5.  DISTANCE FROM NOZZLE TO INTERACTION REGION
C    7.  FLIGHT PATH LENGHT OF FRAGMENT (CM)
C   10.  DWELL TIME FOR CALCULATED TIME OF FLIGHT  (X E-6)
C   11.  A COEFFICIENT IN PPROB=A*COS(POLANGLE)+B
C   12.  B COEFFICIENT IN ABOVE EQUATION
C   13.  POLARIZATION ANGLE WITH RESPECT TO BEAM.
C   14.  INITIAL VELOCITY (CM/SEC)
C   15.  FINAL VELOCITY (CM/SEC)
C   16.  VELOCITY INCREMENT (CM/SEC)
C   17.  TRANSLATIONAL TEMPERATURE OF BEAM
C   18.  AVERAGE MASS OF BEAM
C   19.  MOST PROBABLE VELOCITY
```

```
C
C
C  * * * * * * * * * * * * * * * * * * * * * * * * * * * * * * * * *
C
C  SET UP TO READ FILE  DATACMLAB
C  THIS FILE READS EXPERIMENTAL CONDITIONS
C
C
C  READ DATA IN ORDER LISTED ABOVE
C
      READ(13,4000)BMASS,FMASS
      READ(13,4000)ENGION,IONLGT
      READ(13,4005)ANGLE
      READ(13,4005)BLONG
      READ(13,4005)FGPATH
      READ(13,4010)FDWELL
      READ(13,4005)PANGL
      READ(13,4000)POLA,POLC
C
      READ(13,4025)BVMIN,BVMAX
      READ(13,4005)BVINC
      READ(13,4005)TS
      READ(13,4005)AVMASS
      READ(13,4030)VS
C  ALL DATA FROM  DATACMLAB  IS READ
C
C
C  * * * * * * * * * * * * * * * * * * * * * * * * * * * * * * * * *
C  COMPUTE VELOCITY DISTRIBUTION ARRAY VELDIS(I) FOR
C  A THEORETICAL BEAM.
C
C
C  CALCULATE THE NUMBER OF VELOCITIES--LIMITED TO 256 FROM DIMENSION STATEMENT
C
      RVEL=(BVMAX-BVMIN)/BVINC
      NVEL=INT(RVEL)+1
      IF(NVEL.LT.256)GO TO 55
      NVEL=256
55    VELCTY=BVMIN-BVINC
      DO 60 I=1,NVEL
      VELDIS(I)=VELCTY+BVINC
      VELCTY=VELDIS(I)
60    CONTINUE
C
C
C  * * * * * * * * * * * * * * * * * * * * * * * * * * * * * * * * *
C
C  CALCULATE VELOCTITY PROBABILTY DISTRIBUTION VPROB(I) OF THEORETICALLY
C  GENERATED BEAM.
C
C  I(V) IS CALCULATED HERE IN NUMBER DENSITY
      DO 65 I=1,NVEL
      C1=AVMASS/(2*(1.3806E-16)*TS*(6.023E23))
      VPROB(I)=VELDIS(I)**2*EXP(-C1*((VELDIS(I)-VS)**2))
      VPROB(I)=VPROB(I)/1E6
65    CONTINUE
C  * * * * * * * * * * * * * * * * * * * * * * * * * * * * * * * * *
C  GENERATE BEAM ANGULAR DISTRIBUTION FUNCTION
C  THE DATA IS READ FROM FILE  BMANGLE
C
      I=1
160   READ(14,170)BMANGL(I),BMAPRB(I),JDONE
      NANGLE=I
      I=I+1
```

```
      IF(JDONE.EQ.0)GO TO 160
170   FORMAT(2F6.2,I3)
C
C * * * * * * * * * * * * * * * * * * * * * * * * * * * * * * * *
C  GENERATE DETECTOR PROBABILITY FUNCTION
C  THE DATA IS READ FROM FILE  DTANGLE
C
      I=1
285   READ(15,300)DTANGL(I),DTAPRB(I),JDONE
300   FORMAT(2F6.2,I3)
      NDTANG=I
      I=I+1
      IF(JDONE.EQ.0)GO TO 285
C * * * * * * * * * * * * * * * * * * * * * * * * * * * * * * * *
C
C  GENERATE IONIZER FUNCTION
C  THE DATA IS READ FORM FILE  IONIZER
C
      I=1
310   READ(16,350)IONIZR(I),IONPRB(I),JDONE
      NIONZR=I
      I=I+1
      IF(JDONE.EQ.0)GO TO 310
350   FORMAT(2F6.3,I3)
C
C * * * * * * * * * * * * * * * * * * * * * * * * * * * * * * * *
C
C  READ LASER FUNCTION
C  THE DATA IS READ FROM FILE  FLASER
C
      I=1
360   READ(17,370)LASER(I),LSRPRB(I),JDONE
      NLASER=I
      I=I+1
      IF(JDONE.EQ.0)GO TO 360
370   FORMAT(2F6.3,I3)
C
C * * * * * * * * * * * * * * * * * * * * * * * * * * * * * * * *
C
C  READ ENERGY DISTRIBUTION
C  DATA IS ENTERED AS CENTER OF MASS TRANSLATIONAL FRAGMENTATION ENERGY
C
      I=1
390   READ(18,400)ENGDIS(I),JDONE
      NENG=I
      I=I+1
      IF(JDONE.EQ.0)GO TO 390
400   FORMAT(F7.2,I3)
C
C
C * * * * * * * * * * * * * * * * * * * * * * * * * * * * * * * *
C
C  ALL DATA IS ENTERED AT THIS POINT
C
C * * * * * * * * * * * * * * * * * * * * * * * * * * * * * * * *
C
C  PRINT PARAMETERS
C  DATA IS OUTPUT TO FILE  PARAMETERS
C
C * * * * * * * * * *
      WRITE(6,5000)
      WRITE(6,5005)
      WRITE(6,5010)
      WRITE(6,5015)BMASS,FMASS
```

```
      WRITE(6,5020)ENGION,FGPATH
      RDWELL=FDWELL
      WRITE(6,5025)IONLGT,RDWELL
      WRITE(6,5035)VELDIS(1)
      WRITE(6,5040)VELDIS(NVEL)
      WRITE(6,5041)AVMASS
      WRITE(6,5042)TS
      WRITE(6,5045)ANGLE
      WRITE(6,5046)PANGL
      WRITE(6,5047)POLA,POLC
      WRITE(6,5050)
      WRITE(6,5055)
      WRITE(6,5060)
      DO 450 I=1,NENG
      WRITE(6,449)ENGDIS(I)
449   FORMAT(F7.2)
450   CONTINUE
      WRITE(6,5070)
      DO 455 I=1,NDTANG
      WRITE(6,5075)DTANGL(I),DTAPRB(I)
455   CONTINUE
      WRITE(6,5071)
      DO 456 I=1,NANGLE
      WRITE(6,5075)BMANGL(I),BMAPRB(I)
456   CONTINUE
      WRITE(6,5080)
      DO 457 I=1,NIONZR
      WRITE(6,5075)IONIZR(I),IONPRB(I)
457   CONTINUE
      WRITE(6,5090)
      DO 458 I=1,NLASER
      WRITE(6,5075)LASER(I),LSRPRB(I)
458   CONTINUE
      WRITE(6,5100)
      DO 460 I=1,NVEL,4
      J=I+1
      K=I+2
      L=I+3
      WRITE(6,5105)VELDIS(I),VPROB(I),VELDIS(J),VPROB(J)
     1    ,VELDIS(K),VPROB(K),VELDIS(L),VPROB(L)
460   CONTINUE
C
C  CONVERT UNITS ECT. BEFORE ENTERING CONVOLUTION DO LOOPS.
C
C  CONVERT ANGLES TO RADIANS
      DO 465 I=1,NANGLE
      BMANGL(I)=BMANGL(I)/57.2958
465   CONTINUE
      DO 470 I=1,NDTANG
      DTANGL(I)=DTANGL(I)/57.2958
470   CONTINUE
      PANGL=PANGL/57.2958
      ANGLE=ANGLE/57.2958
C  CALCULATE THE ION FLIGHT TIME
C  CONSTANT ION ENERGY OVER ENTIRE LENGTH IS ASSUMED
C  V=SQRT(2E/M)
C
      V=SQRT(2.*(1.60209E-12)*ENGION*(6.02E23)/FMASS)
      TMION=IONLGT/V
      MI=BMASS-FMASS
C  CALCULATE REDUCED MASS
      RMASS=(MI*FMASS)/BMASS
C * * * * * * * * * * * * * * * * * * * * * * * * * * * * * * * *
C
```

```
C  THE FOLLOWING IS THE MAIN CONVOLUTION ROUTINE
C  IT CONSISTS OF NESTED LOOPS FOR ALL PARAMETERS WHICH
C  AFFECT THE NEWTON TRIANGLE.  THE PROCEEDURE IS AS FOLLOWS:
C
C  1.  CONSTRUCT NEWTON TRIANGLE USING
C      VELDIS(II),ENGDIS(JJ),DTANGL(KK),BMANGL(LL)
C       ALSO USED ARE BMASS, FMASS, AND ANGLE.
C
C  2.  THE PARAMETER CALCULATED IS LABORATORY VELOCITY.
C      FROM THIS A FLIGHT TIME IS CALCULATED
C
C  3.  THE EVENT PROBABILITY IS THE PRODUCT OF
C      VPROB(II)*DTAPRB(KK)*BMAPRB(LL)*IONPRB(I)*
C      PPROB*LSRPRB(BB)
C
C  4.  THE EVENT INTENSITY IS THEN HISTOGRAMMED USING
C      SPECIFIEID TIME INTERVALS TO GENERATE A SYNTHETIC
C      TIME OF FLIGHT SPECTRUM.
C
C * * * * * * * * * * * * * * * * * * * * * * * * * * * * * * * * * *
C  ZERO THE HISTOGRAM BUFFER
C
      DO 510 I=1,256
      TFHIST(I)=0.0
510   CONTINUE
C
C
C
      DO 900 JJ=1,NENG
C  CONVERT KCAL,S TO ERGS.
      ENERGY=ENGDIS(JJ)*41840000000.
      V=SQRT(2.*ENERGY/RMASS)
C  V2CM IS CENTER OF MASS VELOCITY OF OBSERVED FRAGMENT
      V2CM=M1*V/BMASS
      DO 800 II=1,NVEL
      VELCTY=VELDIS(II)
      DO 700 KK=1,NDTANG
      GM=ANGLE+DTANGL(KK)
      DO 600 LL=1,NANGLE
      DO 597 MM=1,NLASER
      BL=BLONG+LASER(MM)
      AL=BL*TAN(BMANGL(LL))
      DO 595 NN=1,NIONZR
C
C  CALCULATE LAB ANGLE
C
      HL=(FGPATH+IONIZR(NN))*SIN(GM)
      XL=(FGPATH+IONIZR(NN))*COS(GM)
      DL=XL-LASER(MM)
      RL=HL-AL
      XBETA=ATAN(RL/DL)
      ANGL=ABS(XBETA-BMANGL(LL))
      RPATH=SQRT(DL**2+RL**2)
C  TEST IF THERE IS NO BACKSCATTERED PRODUCT.  THIS IMPLIES
C  THAT ALL LAB ANGLES ARE ALLOWED, AND TEST FOR SUCH IS
C  UNNECESSARY.
      IF(V2CM-VELCTY)550,525,525
525   NOBACK=1
      GO TO 555
550   NOBACK=0
C  TEST FOR LARGEST LAB ANGLE POSSIBLE WITH THE GIVEN
C  BEAM VELOCITY AND FRAGMENT VELOCITY.  IF THE LAB
C  ANGLE IS GREATER THAN MAXIMUM ANGLE,  IGNORE THIS
C  SCAN AND CONTINUE.
```

```
C
      STHETA=V2CM/VELCTY
C  SINCE SOME COMPUTERS DO NOT HAVE ARC SIN FUNCTIONS,
C  IT IS GENERATED HERE BY X/SQRT(1-(X**2)
      THETA=ATAN(STHETA/(SQRT(1.-(STHETA**2))))
      IF(ANGL-THETA)555,595,595
555   A=VELCTY*COS(ANGL)
      B=VELCTY*SIN(ANGL)
      C=SQRT((V2CM*V2CM)-(B*B))
      FORVEL=A+C
      BCKVEL=A-C
C
C  CALCULATE THE POLARIZATION DEPENDENCE
C  REF. BUSCH AND K. WILSON J. CHEM. PHYS, 56, 3638 (1972)
C  CALCULATE CENTER OF MASS ANGLE.
      VH=FORVEL*SIN(ANGL)
      STHETA=VH/V2CM
      THETA=ATAN(STHETA/(SQRT(1.-(STHETA**2))))
C  CALCULATE ANGLE BETWEEN POLARIZER AND CENTER OF MASS ANGLE.
      GAMMA=2.*ASIN((SQRT(2.-2.*COS(THETA)*COS(PANGL)))/2.)
C  FOR ISOTROPIC DISTRIBUTION LET POLA=0. AND POLC=1.
C  NOTE:  COS(GAMMA) SHOULD BE SIN(GAMMA) IF PARELLEL
C       TRANSITION IS MADE.
      PPROB=POLA*(COS(GAMMA)**2)+POLC
C
C  CALCULATE FLIGHT LENGTH TO IONIZATION POINT
C
C  RPATH IS THE ACTUAL DISTANCE TO IONIZATION POINT
C
C
      TLAB=(RPATH/FORVEL)+TMION
      CHANL=TLAB/(FDWELL*1E-6)+1.0
C  GET RID OF ABSURD FLIGHT TIMES
      IF(CHANL.GT.256.)GO TO 576
      ICHAN=INT(CHANL)
C  CALCULATE EVENT PROBABILITIES
      EVENT=VPROB(II)*DTAPRB(KK)*BMAPRB(LL)*IONPRB(NN)*
     1    PPROB*LSRPRB(MM)
C
C  TRANSFORM EVENT PROBABILITY INTO AN INTENSITY
      RINTEN=EVENT*(FORVEL**3)/V2CM
C
C  HISTOGRAM THE FORWARD SCATTERED RESULT.
C
      TFHIST(ICHAN)=TFHIST(ICHAN)+RINTEN
576   CONTINUE
C
C  NOW TREAT THE BACKWARD SCATTERED RESULT
C
C
      IF(NOBACK)595,579,595
C  CALCULATE POLARIZATION PROBABILITY FOR BACK SCATTERED PRODUCT.
579   VH=BCKVEL*SIN(ANGL)
      STHETA=VH/V2CM
      THETA=ATAN(STHETA/(SQRT(1.-(STHETA**2.))))
      GAMMA=2.*ASIN((SQRT(2.-2.*COS(THETA)*COS(PANGL)))/2.)
      PPROB=POLA*(COS(GAMMA)**2)+POLC
C
      TLAB=(RPATH/BCKVEL)+TMION
      CHANL=TLAB/(FDWELL*1E-6)+1.0
      IF(CHANL.GT.256.)GO TO 595
      JCHAN=INT(CHANL)
C  CALCULATE AN EVENT PROBABILITY
      EVENT=VPROB(II)*DTAPRB(KK)*BMAPRB(LL)*IONPRB(NN)*
```

```
     1    PPROB*LSRPRB(MM)
C
C  TRANSFORM EVENT PROBABILITY TO AN INTENSITY.
       RINTEN=EVENT*(BCKVEL**3)/V2CM
       TFHIST(JCHAN)=TFHIST(JCHAN)+RINTEN
C
C  GET NEXT LASER POSITION.
595    CONTINUE
C  GET NEXT IONIZER POSITION.
597    CONTINUE
C
C  GET NEXT BEAM ANGLE.
600    CONTINUE
C  GET NEXT DETECTOR ANGLE.
700    CONTINUE
C  GET NEXT BEAM VELOCITY
800    CONTINUE
C
C
C  CONVOLUTION COMPLETE FOR ENGDIS(JJ)
C  WRITE THE DISTRIBUTION ON DISK
       WRITE(20,810)ENGDIS(JJ)
810    FORMAT(F10.4)
       WRITE(20,820)(TFHIST(I),I=1,256)
820    FORMAT(1P6E13.5)
C  CLEAR THE BUFFER AND CONTINUE
       DO 830 I=1,256
       TFHIST(I)=0.0
830    CONTINUE
C
900    CONTINUE
C
C
C  FORMAT STATEMENTS
C
4000   FORMAT(2F7.2)
4005   FORMAT(F7.2)
4010   FORMAT(I2)
4025   FORMAT(2F10.2)
4030   FORMAT(F10.2)
C
C
5000   FORMAT(1H1,///)
5005   FORMAT(51X,19H INITIAL CONDITIONS)
5010   FORMAT(1HO,///)
5015   FORMAT(18H MASS OF MOLECULE:,F6.2,5H AMU.,
      1     11X,18H MASS OF FRAGMENT:,F6.2,5H AMU.)
5020   FORMAT(12H ION ENERGY:,F6.2,5H E.V.,
      1     17X,24H FRAGMENT FLIGHT LENGHT:,F6.2,4H CM.)
5025   FORMAT(19H ION FLIGHT LENGHT:,F6.2,4H CM.,
      1     11X,32H OWELL TIME OF GENERATED T.O.F.:,F7.4,
      2     13H MICROSECONDS)
5035   FORMAT(23H BEAM INITIAL VELOCITY:,F8.2,9H CM./SEC.)
5040   FORMAT(21H BEAM FINAL VELOCITY:,F8.2,9H CM./SEC.)
5041   FORMAT(14H AVERAGE MASS:,F6.2,4H AMU)
5042   FORMAT(18H BEAM TEMPERATURE:,F6.2,11H DEGREES K.)
5045   FORMAT(30X,16H DETECTOR ANGLE:,F6.2,8H DEGREES)
5046   FORMAT(30X,20H ANGLE OF POLARIZER:,F6.2,8H DEGREES)
5047   FORMAT(30X,36H POLARIZATION FUNCTION COEFFICIENTS:,2F6.2)
5050   FORMAT(1HO,//)
5055   FORMAT(55X,8H D A T A)
5060   FORMAT(1HO,16H FILE ENPROB----)
5070   FORMAT(1HO,///,16H FILE DTANGL----)
5071   FORMAT(1HO,16H FILE BMANGL----)
```

```
5075  FORMAT(2F8.2)
5080  FORMAT(1H0,16H FILE IONIZR----)
5090  FORMAT(1H0,15H FILE LASER----)
5100  FORMAT(1H0,25H VELOCITY DISTRIBUTION---)
5105  FORMAT(3X,4(F10.2,1PE14.4,7X))
      CALL EXIT
      END
```